2015

Interlayer Utilization (Including Metal Borides) For Subsequent Deposition Of Nsd Films Via Microwave Plasma Cvd On 316 And 440C Stainless Steels

Jared Ballinger
University of Alabama at Birmingham

INTERLAYER UTILIZATION (INCLUDING METAL BORIDES) FOR SUBSEQUENT DEPOSITION OF NSD FILMS VIA MICROWAVE PLASMA CVD ON 316 AND 440C STAINLESS STEELS

by

JARED BALLINGER

SHANE A. CATLEDGE, CHAIR
ALAN W. EBERHARDT
GREGG M. JANOWSKI
ANDREI STANISHEVSKY
YOGESH K. VOHRA

A DISSERTATION

Submitted to the graduate faculty of The University of Alabama at Birmingham,
in partial fulfillment of the requirements for the degree of
Doctor of Philosophy

BIRMINGHAM, ALABAMA

2015

INTERLAYER UTILIZATION (INCLUDING METAL BORIDES) FOR SUBSEQUENT DEPOSITION OF NSD FILMS VIA MICROWAVE PLASMA CVD ON 316 AND 440C STAINLESS STEELS

JARED BALLINGER

DEPARTMENT OF PHYSICS

ABSTRACT

Diamond thin films have promising applications in numerous fields due to the extreme properties of diamonds in conjunction with the surface enhancement of thin films. Biomedical applications are numerous including temporary implants and various dental and surgical instruments. The unique combination of properties offered by nanostructured diamond films that make it such an attractive surface coating include extreme hardness, low obtainable surface roughness, excellent thermal conductivity, and chemical inertness. Regrettably, numerous problems exist when attempting to coat stainless steel with diamond generating a readily delaminated film: outward diffusion of iron to the surface, inward diffusion of carbon limiting necessary surface carbon precursor, and the mismatch between the coefficients of thermal expansion yielding substantial residual stress. While some exotic methods have been attempted to overcome these hindrances, the most common approach is the use of an intermediate layer between the stainless steel substrate and the diamond thin film.

In this research, both 316 stainless steel disks and 440C stainless steel ball bearings were tested with interlayers including discrete coatings and graded, diffusion-based surface enhancements. Titanium nitride and thermochemical diffusion boride interlayers were both examined for their effectiveness at allowing for the growth of continuous and adherent diamond films. Titanium nitride interlayers were deposited by cathodic arc vacuum

deposition on 440C bearings. Lower temperature diamond processing resulted in improved surface coverage after cooling, but ultimately, both continuity and adhesion of the nanostructured diamond films were unacceptable. The ability to grow quality diamond films on TiN interlayers is in agreement with previous work on iron and low alloy steel substrates, and the similarly seen inadequate adhesion strength is partially a consequence of the lacking establishment of an interfacial carbide phase.

Surface boriding was implemented using the novel method of microwave plasma CVD with a mixture of hydrogen and diborane gases. On 440C bearings, dual phase boride layers of Fe_2B and FeB were formed which supported adhered nanostructured diamond films. Continuity of the films was not seamless with limited regions remaining uncoated potentially corresponding to delamination of the film as evidenced by the presence of tubular structures presumably composed of sp^2 bonded carbon. Surface boriding of 316 stainless steel discs was conducted at various powers and pressures to achieve temperatures ranging from 550-800 °C. The substrate boriding temperature was found to substantially influence the resultant interlayer by altering the metal boride(s) present. The lowest temperatures produced an interlayer where CrB was the single detected phase, higher temperatures yielded the presence of only Fe_2B, and a combination of the two phases resulted from an intermediate boriding temperature. Compared with the more common, commercialized boriding methods, this a profound result given the problems posed by the FeB phase in addition to other advantages offered by CVD processes and microwave generated plasmas in general. Indentation testing of the boride layers revealed excellent adhesion strength for all borided interlayers, and above all, no evidence of cracking was observed for a sole Fe_2B phase. As with boriding of 440C bearings, subsequent diamond

deposition was achieved on these interlayers with substantially improved adhesion strength relative to diamond coated TiN interlayers. Both XRD and Raman spectroscopy confirmed a nanostructured diamond film with interfacial chromium carbides responsible for enhanced adhesion strength. Interlayers consisting solely of Fe_2B have displayed an ability to support fully continuous nanostructured diamond films, yet additional study is required for consistent reproduction. This is in good agreement with initial work on pack borided high alloy steels to promote diamond film surface modification. The future direction for continued research of nanostructured diamond coatings on microwave plasma CVD borided stainless steel should further investigate the adhesion of both borided interlayers and subsequent NSD films in addition to short, interrupted diamond depositions to study the interlayer/diamond film interface.

Keywords: CVD, NSD film, boriding, stainless steel, interlayer

DEDICATION

I dedicate this thesis to the memory of my father, John Ballinger Jr., the hardest working and smartest man I have ever known.

ACKNOWLEDGEMENTS

I would like to express my sincerest thanks to my advisor and committee chair, Dr. Aaron Catledge. His guidance and input have been essential toward the completion of this work. I would like to thank my committee members, Dr. Yogesh K. Vohra, Dr. Gregg M. Janowski, Dr. Alan W. Eberhardt, and Dr. Andrei Stanishevsky for offering their valuable time and providing direction and vital recommendations to the direction of this project.

Many graduate students provided immeasurable support during my time at UAB. I would like to thank Sunil Karna, Gopi Samudrala, Leigh Booth, Jamin Johnston, Mike Walock, and Jeff Montgomery for their shared experiences with CVD and/or insight with various characterization techniques. I would like to thank Mr. Jerry Sewell of the physics machine shop for his continual availability for numerous stage modifications. I would also like to share my appreciation for Mark Case and the staff of the physics office for their assistance with financial related matters.

I would like to extend my deepest gratitude to my family for the continual support, love, strength, and encouragement they have contributed on my path toward educational excellence.

I gratefully acknowledge support for the project provided by Grant number T32EB004312 from the National Institute of Biomedical Imaging and Engineering. Additional support was afforded by the U.S. Department of Education – GAANN

program under Award Number P200A120026 to University of Alabama at Birmingham (UAB). Support also comes from the National Science Foundation Partnerships for Innovation: Building Innovation Capacity (PFI: BIC) subprogram under Grant No. IIP-1317210. Any opinions, findings, and conclusions or recommendations expressed in this material are those of the author and do not necessarily reflect the views of the National Science Foundation.

TABLE OF CONTENTS

Page

LIST OF TABLES

LIST OF FIGURES

1. INTRODUCTION

1.1 Purpose

Various surface coatings have been applied to steels and other metals for many decades. These surface modifications can be divided into three major categories including thermochemical, thermal, and discrete coatings. The overall goal of the different methods is the surface enhancement of a material to improve certain properties while maintaining the softer, tougher base metal interior. Improved surface properties usually include hardness, corrosion resistance, and wear resistance. While many well-established coatings have been developed and are used commercially, none offer the same appeal of a thin diamond film coating given its unique combination of properties that make it the ultimate surface coating augmentation.

Although the applications are numerous, many challenges exist for obtaining a continuous and adherent diamond film on a steel substrate. Direct attempts at diamond coating via chemical vapor deposition lead to the formation of an intermediate soot layer directly on the surface upon which diamond will then form. Because of this poorly adhered layer of soot, the diamond film will freely delaminate. Thus, an interlayer is used to overcome the associated problems with direct diamond deposition on stainless steels. Specifically, the well-established diffusion barrier, titanium nitride, is being implemented in addition to a diffusion-based borided surface. Both of these interlayers

are expected to avoid the problems of direct diamond deposition allowing for diamond films to grow.

Discrete coatings of TiN are being utilized as an interlayer on 440C stainless steel bearings while the thermochemical process of surface boriding as an interlayer is tested on both 440C bearings and 316 discs. Control of the boriding process using the novel method of microwave plasma chemical vapor deposition will allow for the manipulation of the resultant layer microstructure. Ultimately, the commonly seen dual phase boride layer consisting of continuous, discrete layers of both Fe_2B and FeB will be avoided through control of the deposition parameters. The different interlayers are expected to block the diffusion of iron out of the stainless steel and limit carbon's inward diffusion to permit the formation of quality nanostructured diamond coatings. Adherence is likely to be improved with both interlayers aided by the formation of interfacial carbides during the preliminary nucleation stage associated with diamond growth. Finally, the large mismatch between the coefficients of thermal expansion for both the diamond film and stainless steel substrates which leads to residual thermal stress following cooldown due to the elevated temperature of CVD processing will be offset by the incorporation of an interlayer resulting in crack-free, continuous diamond coatings.

1.2 Intellectual Merit

The overall goal of this work is the successful deposition of adherent diamond films on stainless steel substrates. This is of great importance due to the many attractive properties of diamond that can be exploited by surface modification with only a thin film of polycrystalline diamond deposited on a bulk material. Stainless steel sees wide use in

many areas throughout the world, so the ability to enhance the properties of such a readily available material would have great impact. While much research has been geared toward this same goal, little commercial success has been realized.

Metal nitrides are known to be excellent diffusion barriers, so they have potential for allowing a diamond film to grow without the mutual diffusion of carbon and iron that would otherwise hinder its synthesis via direct deposition. Titanium nitride, a commonly used surface coating, has enjoyed usage in microelectronics as a diffusion barrier to copper and aluminum migration. While it has also been attempted on iron and low alloy steels as an interlayer for subsequent diamond deposition, it has not been incorporated on 440C martensitic stainless steel which is an important grade used in biomedicine such as in surgical tools and dental instruments given its combination of corrosion resistance, hardenability by heat treatment, and relatively low cost. Additionally, the application of a nanostructured diamond film via the patented gas chemistry developed at UAB through work mainly on Ti-6Al-4V has not been explored.

A novel method of boriding is being utilized to modify the surface of the stainless steels prior to diamond deposition. Boriding is already a commercially used surface modification technique for low alloy steels, stainless steels, and other metals. However, plasma methods, such as microwave plasma chemical vapor deposition, need to be further developed as they offer some advantages over the industrialized techniques. Being able to achieve this two-step deposition utilizing the same system would prove beneficial both logistically and financially. CVD processes have advantages in particular including the deposition of highly dense, pure materials with excellent uniformity. This has the potential to limit porosity of the boride layer that is often present following

commercial boriding. Control of the CVD processing parameters allows for modification of the surface morphology and microstructure of a coating. This is of particular importance given the FeB phase is undesirable as its brittleness and high thermal expansion coefficient can result in catastrophic failure of the boride layer even without a diamond film. The more common pack and paste boriding methods normally require temperatures greater than 900 °C while CVD allows for lower substrate temperatures during deposition while still maintaining respectable growth rates. While some plasma methods have received research interest, these have not utilized microwave radiation as an activation source. Relying on microwave radiation presents several benefits including stability and reproducibility of the plasma, energy efficiency, potential for scaleup, and use of a relatively inexpensive microwave source.

Achieving a diffusion barrier on the stainless steel is of paramount importance to the successful deposition and adhesion of a subsequent diamond film. Literature has shown that boride interlayers formed by the industrialized pack boriding method have produced some favorable results for adhesion of larger microcrystalline films. Boriding via microwave plasma CVD could reduce costs by limiting the amount of time required for boriding and utilizing a single system for both boriding and diamond deposition. CVD relies on many variables that can all affect the deposition process including microwave power, pressure, and gas flowrate. Prior experimentation has shown temperature to have a profound effect on the boride interlayer formed. Different boride stoichiometry combinations are produced at different surface deposition temperatures. A controlled study of the boriding process where substrate temperature is changed through control of pressure and microwave power with other parameters held constant would give

important information into the boride layer itself. Characterization of these various temperature borided stainless steel samples will provide insight into their potential for supporting a well-adhered, continuous diamond film. As with TiN interlayers, the testing of the patented NSD gas chemistry developed at UAB will be implemented on graded boride interlayers for achieving ultrasmooth films ideal for wear applications.

1.3 Diamond

Interest in diamond has greatly increased due to the promising applications as well as the developments in the processes. The chemical vapor deposition technique has led to the ability to coat a variety of materials with thin films composed of diamond. Diamond has always been a greatly desired material due to its wonderful combination of properties, many of which are the ultimate among all materials. Impressively, synthetic diamond films are able to achieve many of the same properties of natural single crystal diamond. Some of the most notable properties are diamond's immense hardness, great thermal conductivity, and large transparency to the electromagnetic spectrum. The hardness and thermal conductivity give rise to applications in the cutting and grinding industry. Additionally, diamond has great potential as a coating for preventing surface wear such as in bearings or orthopedic implants. This relies on the hardness of diamond as well as a low coefficient of friction (a film must be polished or rely on a reduced grain size). The large transparency range of diamond makes it useful as a window due to its high transmittance of electromagnetic radiation. Diamond is also a desired material for use in electrical heat sinks due to its great thermal conductivity as well as its high electrical resistivity [1-4].

Diamond is only one of many unique forms that carbon has been found to assume. Over the last three centuries, unique allotropes of carbon discovered include fullerenes [5-8] with their cage-like soccer ball structure for targeted drug delivery, carbon nanotubes [7-10] with excellent tensile strength, thermal conductivity, and tailorable electronic properties, and graphene [11, 12], single atomic layer sheets of graphite likewise possessing a collection of impressive properties with applications in microelectronics, energy storage, and more. These are in addition to the other common carbon form of graphite, a planar structure with carbon atoms covalently bonded to three nearest neighbors forming a honeycomb lattice; the individual sheets (graphene) are held together loosely by van der Waals forces which allow the singular sheets to slide giving rise to graphite's lubricating applications. In terms of crystal structure, diamond has a face-centered cubic (FCC) unit cell containing eight carbon atoms with an edge length, *a* = 0.357 nm. The diamond unit cell is shown in Figure 1. Each carbon atom is covalently bonded to its four nearest neighbors in a tetrahedral structure, and the C-C bond length is given by $d = \frac{a\sqrt{3}}{4} = 0.154$ nm. Owing to the strength of the C-C covalent bonds and the rigidity of the tetrahedral structure, diamond possesses a thermal conductivity of over five times that of copper at room temperature (2000 $W \cdot m^{-1} \cdot K^{-1}$), chemical inertness (will not react with most acids or alkalis), supreme hardness, and elevated melting point. Diamond is considered to be a wide band-gap semiconductor (5.47 eV at 300 K) giving it a negative electron affinity. Additional optical properties include broadband transparency from UV to the far infrared of the electromagnetic spectrum and a refractive index of 2.4, the highest of any material that is transparent to visible light and providing the sparkle of a brilliant cut diamond crystal (in conjunction with total internal reflection). Natural

diamond can be divided into an assortment of types depending on the presence of defects such as nitrogen inclusion and giving diamond the range of properties observed, various colors including yellow to blue, and limiting their application specific usage.

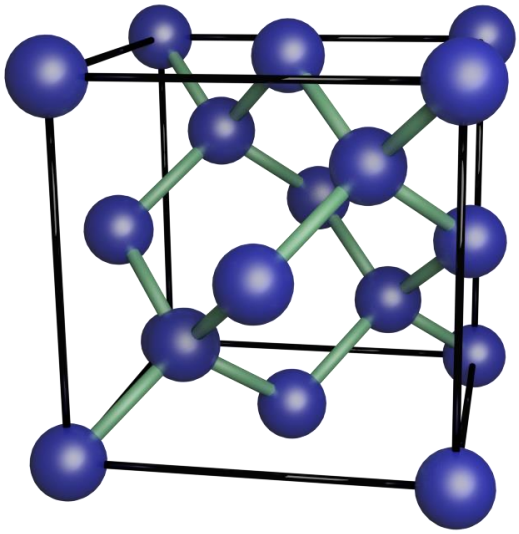

Figure 1: Unit cell of the diamond lattice which has a face-centered cubic crystal structure. Tetrahedral arrangement is seen by the covalent bonding to the four nearest neighbors.

The advent of diamond growth from the vapor phase using chemical vapor deposition (CVD) has ignited the research field given the broad engineering potential of synthetic diamond with adjustable and consistent properties particular to a preferred utilization. A phase diagram for carbon shows the thermodynamically stable regime of diamond to be at extreme temperatures and pressures with natural genesis ensuing at depths of 200 km where temperatures of 1500 °C and pressures greater than 7 GPa exist. The first method developed to produce diamond, High Pressure, High Temperature (HPHT), utilizes this stable region to synthesize diamond from a carbon-rich melt accompanied by a metal solvent like iron. HPHT provides control of the shape and quality of produced diamonds with most being small grains used as abrasives. CVD of

diamond was first reported in the 1950s but met with skepticism and poor growth rates. The growth of diamond by CVD operates in a metastable regime given the low pressures and temperatures normally below 1000 °C. It relies on dissociation of hydrogen and hydrocarbon gases by heating in excess of 2000 K using various energy sources [1, 2, 4]. A range of microstructures including amorphous carbon [13], polycrystalline diamond [1], and single crystal diamond [1] can be deposited depending on the substrate material. CVD diamond also provides the ability to coat large areas in excess of 300 mm and to uniformly deposit onto curved geometric substrates. While very pure diamond films can be grown when compared with natural diamond, defects can still be present such as hydrogen inclusion, especially in the grain boundaries, given the overwhelming presence in the feedgas. Grain boundaries are also the source of amorphous carbon, especially as the grain size of diamond is reduced to the nanoscale. Within single crystals of diamond, both extended defects (dislocations) and point defects (substitutional impurities such as nitrogen) can occur. Given the metastable regime of CVD, incorporation of sp^2 bonded carbon is one of the most common defects observed which can be readily probed by Raman spectroscopy [14, 15].

Numerous applications exist for CVD diamond given the combination of desirable properties that can be exploited. Many of the CVD synthetic diamond properties fall within the range of natural diamond including hardness and strength. These provide exceptional wear properties for diamond combined with the thermal conductivity (also comparable to single crystal diamond) and low surface friction making it an excellent coating for cutting tools. A resistance to thermal oxidation is advantageous for machining in both high speed and dry conditions. The stiffness of diamond provides

for numerous acoustic applications including surface acoustic wave devices and tweeter domes found in loudspeakers. A key principle for tweeters when reproducing sounds is the breakup frequency which is proportional to the sound propagation velocity, $v \propto \sqrt{E/\rho}$, in a material, and compared to customarily used aluminum, diamond should have three times the performance. The thermal conductivity of diamond at room temperature is greater than any other material. While heat conduction is usually the responsibility of free electrons in a metal, lattice phonons provide the mechanism of heat conduction in diamond. Beyond its applications in cutting tools, the excellent thermal conductivity allows service in thermal management such as heat sinks for many electronic devices. Wide spectral transparency makes diamond a prime choice as a window material, one example being high-power CO_2 lasers. The fact that diamond is a wide-bandgap semiconductor results in its ability to support large electric fields prior to breakdown. Active power grids could be reduced substantially in overall size with switches utilizing diamond coatings [1, 2, 4]. The revolutionary applications are plentiful and research continues to push the conventional boundaries.

CVD diamond is also seen as having many applications in biomedicine such as surface coating of orthopedic implants to improve longevity, therefore reducing the frequency of revision surgeries [16-18]. Current artificial implants include a metal ball articulating against an ultrahigh molecular weight polyethylene cup. Wear of the plastic leads to osteolysis and tissue inflammation and eventually requires replacement as the implant inevitably loosens. Corrosion of the two surfaces is also a potential issue given they are in contact with human bodily fluids. Thus, factors influencing a potential coating include wear resistance, low surface friction, corrosion resistance, and

biocompatibility. A nanostructured diamond coating of Ti-6Al-4V, one such metal used in artificial implants, was developed at UAB and meets all of these needs [17]. Diamond having ultimate hardness will not wear, it is chemically inert which is great for corrosion resistance, the nanostructured diamond film microstructure has an extremely smooth surface for low coefficient of friction, and diamond studies have shown improved biocompatibility [16, 19] compared to uncoated orthopedic implants. Given the need for enhanced wear performance and lubricity of a multitude of medical devices, nanostructured diamond coatings are a promising endeavor with applications for heart valves, stents, dental instruments, and coronary arterial cleaning devices [20] being only the beginning of potential applications.

1.4 Stainless Steel

Stainless steels are high alloy steels defined as having a minimum of 11% chromium. Stainless steel's chief property to distinguish it from other steels is its ability to develop a passive layer of chromium oxide on the surface which protects it from the formation of iron oxides as seen with low alloy steels. This protective film is only a few atomic layers thick and has limited self-healing to damage of the steel’s surface. The provided corrosion resistance allows for protection in both air and aqueous environments. Stainless steel is a poor conductor compared to copper, and some stainless steels are magnetic, such as martensitic and ferritic grades, while austenitic stainless steels are not. Many different grades of stainless steels exist with numerous applications. The ability for stainless steel to be sterilized enhances its antibacterial properties for applications in the former two areas of use. It is formed into sheets, tubes, and bars for use in surgical

instruments, food related equipment, appliances, and for structural purposes. Stainless steel production starts with the melting of recycled scrap in addition to the respective alloying elements using an electric-arc furnace. Next, argon oxygen decarburization is used to refine the melt by injecting a mixture of argon and oxygen in order to achieve the desired carbon level. A secondary refinement step is required for many stainless steel grades such as a vacuum treatment where the chemical composition is finalized. Casting is then conducted, usually by the continuous casting process, to transform the melt into slabs. Hot and cold rolling can then be performed to transform the slabs to more usable forms such as sheets and rods. Finally, the categorizing of stainless steels is broadly based on their crystalline structure [21-23].

Austenitic stainless steel such as 316 have a face-centered cubic (FCC) crystal structure indicative of the austenitic iron phase. They are the most common type of stainless steel possessing a great balance of properties. Compared to other stainless grades, austenitic stainless steels have enhanced corrosion resistance with a minimum of 16% chromium to upward of 25%. 3xx stainless steels are both weldable and formable which is highly desirable when working with a metal, and its operating temperatures span a vast range from use in cryogenics to the extreme heat of a jet engine. They have minimal carbon and sufficient nickel and/or manganese added to retain the austenitic crystal structure. Austenitic stainless steels maintain their strength levels at higher temperatures better than ferritic stainless steels. Drawbacks of this group include limited resistance to cyclic oxidation compared to ferritic stainless steels, more vulnerable to thermal fatigue than ferritic grades, and susceptible to stress corrosion cracking if not adequately chosen for the corrosiveness of the operating environment [21-23].

Ferritic stainless steels have the ferritic iron crystal structure which is body-centered cubic (BCC). This is the most common crystal structure of all steels, but this grade encompasses only one fourth of all stainless steel production. They usually contain less alloying elements leading to lower costs and enhanced engineering properties but worse corrosion resistance. They are more of a budget stainless steel compared to austenitic given the lower level of chromium and lack of nickel, an advantage given the volatility of nickel pricing. Improvements in processing methods have led to newer grades such as 439 and 441 which meet a variety of operating needs including good formability and the accommodation of common joining methods, and they are potential alternatives to the common 304 austenitic stainless steel. Duplex stainless steels are an interesting median of the previous two as their microstructure consists of roughly a balance of both austenite and ferrite grains. This leads to new stainless grades that can provide a combination of desired properties from the former two. In terms of alloys, higher chromium content (20-25%) is present compared to austenitic grades but only minimal nickel (1-7% versus 10-20%). Finally, molybdenum and nitrogen are used to achieve the stable balance of microstructure. Physical properties include improved resistance to stress corrosion cracking than austenitic stainless steels and improved toughness when compared with ferritic grades [21].

Martensitic stainless steels like 440C are the least corrosion resistant class, but they have the highest achievable hardness due to the martensitic crystal structure (body-centered cubic). A comparison of BCC martensitic and FCC austenitic crystal structures is presented in Figure 2. The limited corrosion resistance relative to austentic stainless steels is due to the low levels of chromium ranging from 10-18%. Carbon (0.2-1.2%) is

added which allows for a variety of mechanical properties to be obtained through heat treating, just as with low alloy steels. High hardness comes from austenitizing (heating to above the critical temperature for austenite to be the stable phase) where the sample is held for an extended time to ensure uniform phase transformation followed by quenching. Quenching is done to ensure sufficient cooling (air cooling or oil quenching depending on section size and grade) for austenite transformation into martensite. Tempering is needed after cooling due to the brittle, as-quenched martensite, in order to improve ductility and strength in favor of some hardness [21, 24].

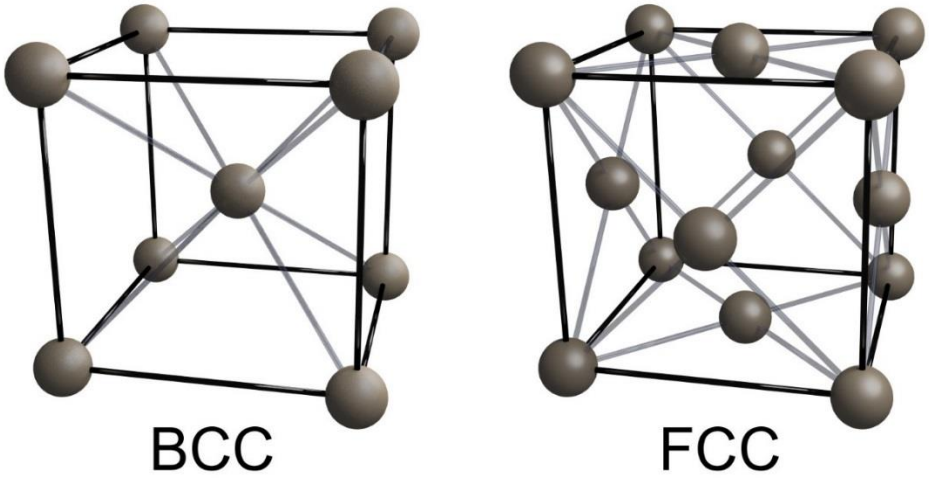

Figure 2: Body-centered cubic (BCC) and face-centered cubic (FCC) unit cells of martensitic and austenitic stainless steels respectively.

1.5 Challenges of Diamond Deposition on Stainless Steel

Diamond deposition is challenging on many materials including ferrous substrates such as stainless steel. Iron is known as a carbon dissolving material, particularly at the conditions used in the CVD process (Fe: 1.3 wt. % C at 900 °C). Thus, carbon dissolves into the substrate leaving very little carbon precursor remaining at the surface for diamond nucleation [25]. A second problem is associated with the high vapor pressure of

Fe. This results in the diffusion of iron out of the substrate to the surface. Any transition metal with a partially filled *d* –electron shell will result in the catalytic formation of graphite when attempting direct diamond deposition [26-28] as well as other soot such as iron carbides. These two processes hinder the formation of sp^3 carbon bonds needed for diamond growth. Only after a sufficiently thick layer of soot has formed directly on the surface will a diamond film be deposited [29]. However, the loosely adhered layer of soot underneath the diamond results in an unpractical film that readily delaminates. An additional problem is the large difference between the thermal expansion coefficients of diamond and stainless steel which negatively influences the adhesion of the diamond film leading to large residual stresses after cooling the sample from deposition temperature. Figure 3 illustrates the mutual diffusion of carbon into the steel and iron to the surface resulting in a layer of soot forming directly on the substrate. Any diamond layer that eventually deposits will merely delaminate upon cooling.

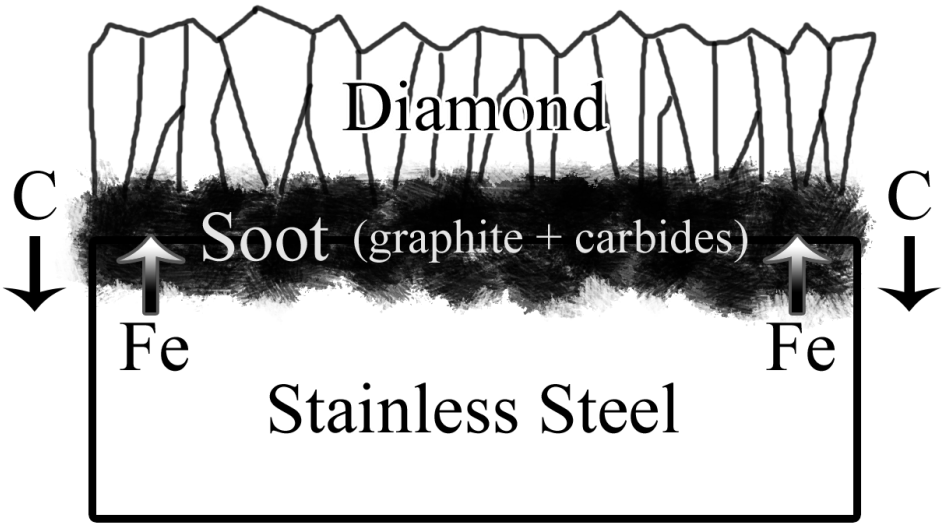

Figure 3: A diagram of a direct diamond deposition on stainless steel illustrating the mutual diffusion of Fe and C atoms resulting in a soot layer forming directly on the steel upon which a diamond film will eventually grow and then readily delaminate.

While some exotic methods have been attempted in order to achieve diamond growth on ferrous substrates, the most common approach is to use an intermediate layer, or interlayer. One property of extreme prominence when choosing the interlayer includes the ability to block the diffusion of iron to the surface as well as carbon into the substrate. Without this mutual diffusion, adherent diamond films are a possibility. In addition, an intermediate coefficient of thermal expansion relative to diamond and stainless steel is desirable to offset the residual thermal stresses due to thermal expansion coefficient mismatch. The linear coefficients of thermal expansion for stainless steel and diamond are given in Table 1 in addition to those for various interlayer materials. The interlayer should be well adhered to the substrate or else the subsequently deposited diamond film provides little practical value. Furthermore, it should promote the formation of carbides during the initial stages of diamond deposition which is an indicator of favorable adhesion between the substrate surface and diamond coating. Since diamond deposition is conducted at high temperatures, the interlayer must be able to withstand the CVD process itself. Finally, as with any potential commercial application, the economics of the process must be considered [29].

Table 1: Linear thermal expansion coefficients and crystal systems of relevant materials

Material	**α ($x10^{-6}$ K^{-1})**	**Crystal System**
TiN	9.35	Face-Centered Cubic
Fe_2B	7.85	Body-Centered Tetragonal
FeB	23.0	Primitive Orthorhombic
CrB	12.3	End-Centered Orthorhombic
316 Stainless Steel	16.0	Face-Centered Cubic
440C Stainless Steel	10.2	Body-Centered Cubic
Diamond	1.18	Face-Centered Cubic

A diffusion barrier is a key requisite when selecting an interlayer material. TiN is one such material that has been extensively used as a diffusion barrier. Properties responsible for this role include the relatively high thermal stability, chemical inertness, and low electrical resistivity. These characteristics are common among most of the transitional metal nitrides which has earned it a place as a widely selected barrier in circuit applications such as in blocking aluminum and copper migration [30, 31]. TiN has also been shown to be an effective diffusion barrier to the inward diffusion of carbon [32]. Given these properties, it is likely be an adequate barrier to the upward diffusion of Fe which would be expected to have a more comparable diffusion rate to aluminum versus the smaller and more mobile atoms of carbon. Transition metal borides, such as Fe_2B, are composed of dense microstructures which are favorable as diffusion barriers. Fe_2B is known to have very little carbon solubility with it observed to pool underneath the boride layer [33]. These borides form tightly packed lattices with iron atoms at the lattice sites and the smaller boron atoms at interstitial, octahedral hole positions, as demonstrated in Figure 4 by the Fe_2B body-centered tetragonal unit cell. Boron atoms are covalently bonded to the iron atoms. Combined with the chemical stability of these structures, transition metal borides should effectively impede both carbon and iron diffusion [34].

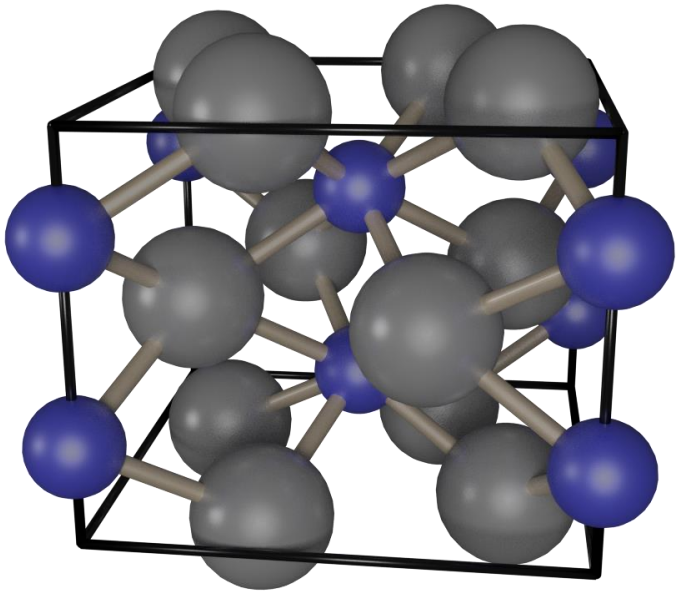

Figure 4: The Fe_2B unit cell with its body-centered tetragonal crystal structure. The small blue spheres represent boron atoms with iron atoms corresponding to the larger grey ones.

1.6 Diffusion coatings on stainless steel

Many coatings are applied to steels in order to enhance the surface properties of the base metal. These usually consist of improved hardness and corrosion resistance in addition to other application specific properties. Surface modification of steels explicitly is of principal importance given it is the engineering material of choice for a vast array of applications. Coatings usually are of two varieties: overlay coatings and diffusion coatings. The former relies on depositing a completely foreign material on the surface of the steel. These are usually applied by means of physical vapor deposition, electroplating, or plasma spraying. Little diffusion of the coating material is observed in the substrate constituents leading to a sharp interface between the coating and metal. On the other hand, diffusion coatings rely on a thermochemical process where atoms are

diffused into the steel and react to form new compounds with the substrate elements. The interface of this type of coating is not a discrete surface, but a graded structure with increasing amounts of the diffused elements occurring near and on the surface. A heat source to enhance the diffusion is a commonality shared by the different methods used to form diffusion coatings. The diffusion depth can be described the following parabolic law:

$$x = D\sqrt{t}$$

where *x* is the case depth, *D* is the diffusion coefficient, and *t* is the time. The diffusivity coefficient depends on a number of factors including the temperature of deposition and the steel to be modified [7-9].

The primary equation which describes steady-state diffusion is known as Fick's law:

$$J = -D\frac{dC}{dx}$$

where *J* is the atomic flux (number of atoms through a plane of unit area per unit time), *D* is the diffusion coefficient, *C* is the atomic concentration, and *x* is the position. This says that a negative gradient in the concentration at some position yields a positive flux in the direction of +*x*. Thus, the minus sign translates to diffusion down the concentration gradient, also known as the driving force of diffusion. For non-steady-state diffusion, i.e. concentration of atoms varies with time, Fick's second law is applied:

$$\frac{dC_x}{dt} = D\frac{\partial^2 C}{\partial x^2}$$

(in one dimension). A solution is obtained in the form of the error function:

$$C[x(t), t] = A + B\ erf\left(\frac{x}{\sqrt{4Dt}}\right)$$

where A and B are determined by the initial settings and boundary conditions. The diffusion coefficient is a measure of the mobility of the diffusing atoms. It can be related to activation energy and temperature by an Arrhenius equation:

$$D = D_0 e^{\left(-\frac{E_A}{RT}\right)},$$

with D_0 (cm^2/s) being a proportionality constant (diffusivity when temperature is infinite), E_A (J/mol) the activation energy of the diffusing atoms, R (J/mol/K) the ideal gas constant, and T (K) corresponding to temperature [35].

Diffusion in solids takes the form of two principal mechanisms. Vacancy diffusion corresponds to the movement of atoms through vacant sites of the crystal lattice. Examples include self-diffusion of a bulk material and diffusion of substitutional impurities. The second common process is interstitial diffusion involving the migration of atoms via interstitial sites within the crystal lattice. In order for diffusion to occur, energy is required to break bonds and distort the lattice as the atom moves from site to site. The number of atoms with the required energy, which is highly dependent on the temperature, can be described with Boltzmann statistics. Vacancy sites are present for any crystal structure and the number of vacancies is directly proportional to the temperature which likewise is directly related to the rate of diffusion. Interstitial diffusion is generally the faster form of diffusion given the large number of interstitial sites compared to the relatively low quantity of vacancies. However, it requires smaller atoms such as H, C, O, N, or B. The high mobility of these atoms also leads to enhanced diffusion rates relative to vacancy diffusion. Other factors also influence the diffusion rate of various atoms through different materials. Crystal structure plays an important role with open lattices lending themselves to faster diffusion. As an example, comparing

the diffusion rates of carbon in FCC iron and BCC iron at the same temperature, the values are greater for the latter due to the lower atomic packing factor and thus, more open crystal structure. This is not the same as the solubility of carbon in these two iron crystal structures which is greater for FCC iron due to the larger interstitial sites it provides. Bonding in a material also plays a role with stronger bonds such as metallic and covalent bonds giving rise to slower diffusivity. Diffusion is also affected by defects in crystal structure, such as edge dislocations, in addition to grain boundaries. The effects are harder to calculate directly but lead to increased diffusion rates since it provides a more open structure resulting in a lower required activation energy [35].

Three of the most common diffusion-based coating methods of steels that have been thoroughly investigated and enjoyed commercial success include diffusing either carbon, nitrogen, or boron into the metal. These are referred to as carburizing, nitriding, and boriding respectively. Nitriding is performed by diffusing atomic nitrogen into the metal which improves both corrosion and oxidation resistance of steels. It is performed at a relatively low temperature of approximately 500 °C when compared to the other methods. The reduced temperature allows for comparatively better dimensional control of the workpiece with little deformation. The resultant surface structure of the steel is dependent on the steel and nitriding method. The case structure consists of a diffusion zone of the original steel microstructure in solid solution with nitrogen atoms and precipitates. A surface compound of either Fe_4N (γ') or Fe_3N (ε) can form and cases are stratified. If the outer surface layer is all γ', it is modified or removed because even though it possesses great hardness, it is extremely brittle leading to possible spallation during use. The case structure formed as a combination of these phases demands precise

control for the particular application. Three main nitriding methods are offered commercially including gas, liquid, or plasma nitriding. Gas nitriding is the most common given the excellent control it provides while requiring long processing times and producing shallow case depths. Plasma nitriding prevents oxidation of grain-boundaries and improves surface saturation which reduces required nitriding times [36, 37].

Boriding is a similar diffusion process in that heat is used to produce a thermochemical reaction which results in boron atom diffusion into the steel surface. Comparatively higher temperatures are implemented ranging from 800-1050 °C in most instances. Like nitriding, boriding results in improved hardness, wear resistance, and corrosion resistance. The process can be performed in solid, liquid, or gaseous boron containing environments. Iron borides that form as a result of the process have the huge advantage of achievable hardness values from 1600 to 2000 HV which is substantially higher than both nitriding and carburizing which can achieve maximum hardness levels of approximately 900 and 700 HV respectively. Combined with the low surface friction, borided steels have outstanding resistance to wear. Two main iron boride phases form during the diffusion process: Fe_2B and FeB. A single phase boride layer usually is comprised solely of Fe_2B while a double-phase layer adds FeB on top. This is undesirable given the harder and more brittle nature just as with the γ' phase for nitriding. If FeB is only present in small amounts without forming a continuous layer, then its presence is acceptable. Post annealing steps have been developed to limit the existence of continuous layers of FeB in boride layers [36-38]. A cross-sectional representation of a dual-phase borided steel surface is displayed in Figure 5 (a). Figure 5 (b) shows the gradual change in composition as the surface is approached from the bulk steel.

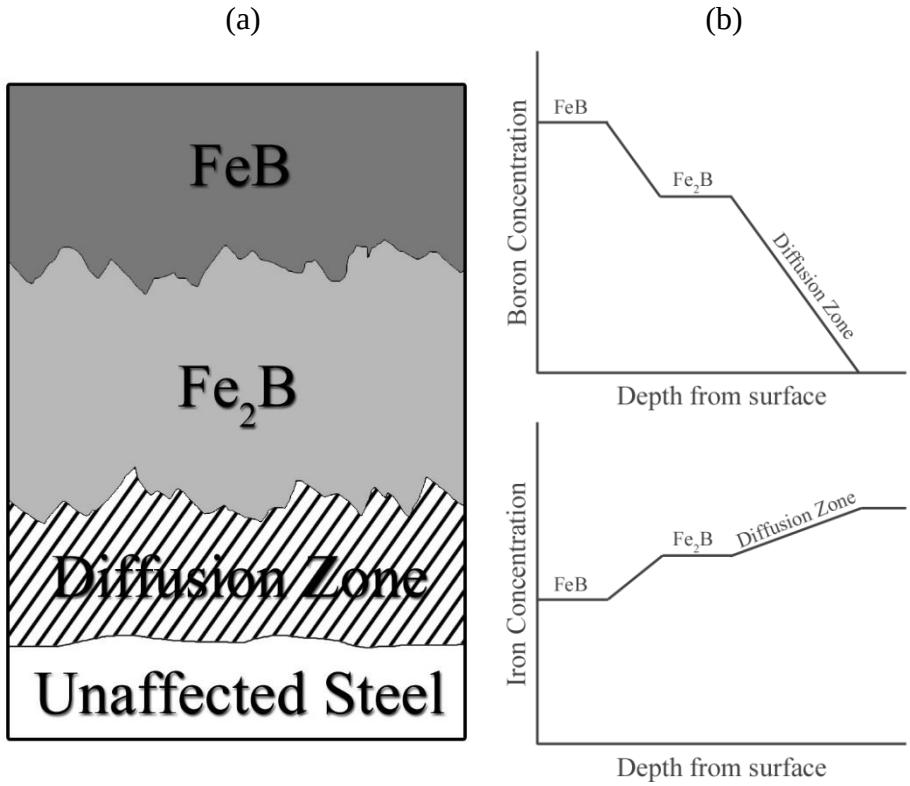

Figure 5: Graded, diffusion-based nature of borided steel surface. (a) Cross-sectional view of the microstructural evolution of a boride layer with the undesirable dual phase. (b) Corresponding boron and iron concentrations as a function of depth.

Numerous methods exist for applying the diffusion based boride coating including pack boriding, paste boriding, liquid boriding, gas boriding, and plasma boriding. The first two methods are the only techniques seeing wide use with liquid and gas being problematic given the environmental concerns associated with the toxic and explosive atmospheres required. Pack (cementation) boriding is the most common process and is accomplished by packing the steel component to be coated in heat-resistant retort with a powder mixture consisting of a boron source, activator, and inert filler. Commonly used boron sources include boron carbide, ferroboron, and amorphous boron while activators consist of KBF_4, NH_4Cl, NA_2CO_3, and more. Paste boriding is the commercial alternative to pack boriding which uses a paste applied to the surfaces to be borided

instead of packing the workpiece in a powder. Again, a boron source and activator is required in addition to a binding agent to form the paste. Once more, the sample is placed in a furnace and heated (though paste boriding additionally requires a protective atmosphere) to the selected temperature and held for an extended period of time to form the desired thickness and microstructure [37, 38].

Plasma boriding processes have received some attention as an alternative to the more accepted pack and paste boriding treatments. These processes rely on the assistance of plasma formation near the surface to increase the efficiency of the boron diffusion. Several advantages are apparent including the reduced temperatures and duration of the process. This is economically favorable given the directly associated decline in cost that would be accompanied by this reduced energy usage. An increase in the boron potential at the surface relative to the pack boriding method is responsible for this improved diffusion proficiency. Composition of the resultant layer and thickness are both controllable through command of the process parameters such as temperature and gas chemistry. The main drawback is the toxicity and explosive nature of the boron gas sources used which include B_2H_6 and BCl_3. However, waste byproducts of the powders and pastes also present environmental hazards that must be disposed of properly. Additionally, some porosity can result which can be problematic for a part in service, but this again is not limited to the plasma gas methods [38, 39].

1.7 Literature Review

A multitude of interlayers have been explored as suitable diffusion barriers for the acceptance of diamond films including CrN [40-42], TiN [43-45], Ni [46, 47], and Ti

[48]. Additionally, more exotic systems of materials, such as a dual metal interlayer of W-Al [49], have also been investigated. Most of these interlayers have been met with limited success. One such problem is the sharp change in material properties at the interface, with locally high stress providing a driving force for delamination. With the addition of an interlayer, multiple interfaces are present which can increase potential for interfacial fracture/delamination. One such solution is to create a gradual transition in surface composition/structure via thermal diffusion such as seen via nitriding [50] or boriding [51-53].

A promising interlayer approach attempted on high alloy steels is a borided surface implemented by Buijnsters *et al.* [51]. In this work, two substrates were used: 316 stainless steel and H11 tool steel. Boriding was carried out via the pack cementation process with an interrupted treatment of boriding for 1 hour followed by annealing for 15 minutes, for a total of four cycles. It was found that varying the boron carbide concentration during boriding led to either a dual phase FeB and Fe_2B interlayer or a single phase Fe_2B layer. Following boriding, the samples were polished and ultrasonically abraded with diamond powder. Hot filament CVD was used to deposit diamond films with a CH_4/H_2 ratio of 0.5%. A total pressure of 50 mbar, a temperature range of 520 to 650 °C (though likely 50-100 °C higher due to thermocouple placement), and a total gas flow of 200 sccm was maintained. Diamond deposition onto borided 316 stainless steel and H11 tool steel which contained the FeB phase resulted in heavy delamination of the deposited films due to thermal expansion coefficient mismatch. Raman spectra of the remaining diamond film yields an upshifted doublet diamond peak indicative of large thermal stresses following cooldown. Similar CVD experiments on

both steels which only had the Fe_2B phase present after boriding resulted in continuous and adherent diamond films. Films grown on the borided 316 stainless steel had facetted diamond crystallites ranging from 300-1500 nm in size that tended to clump together. Raman spectra displayed only a slightly upshifted diamond peak, and XRD of the diamond coated borided 316 stainless steel contains peaks for Fe_2B, γ-iron, and diamond. In addition, Cr_3C_2 peaks are detected indicating an interfacial phase present between the diamond and boride layer which is expected for well-adhered diamond films[51].

Silva *et al.* [46] tested a unique multilayer system consisting of Ni/Cu/Ti on high-speed M2 steel. A thin 3-4 um film of Ni was first applied followed by a larger 32-36 um layer of Cu with both deposited via electroplating. Finally, a thin layer (0.5-2.5 um) of Ti was deposited using arc sputtering. The Ni layer was used for improved adhesion of the multilayer, the Cu was responsible for shear stresses of the deposited films, and Ti was present for adhesion of the diamond film to the interlayer. Samples were ultrasonically abraded in a diamond powder suspension prior to diamond deposition. MPCVD was used for the diamond thin film growth with powers ranging from 1.0-1.3 kW, total pressures of 60-70 Torr, and H_2 flow of 300 sccm. CH_4 flowrate was either 9 or 15 sccm with an introductory step of 30 sccm to enhance the initial diamond nucleation stage. Deposition time was usually 5 hours though longer runs of 24 and 54 hours were also attempted. Finally, a 1 hour ramp-down was used in order to reduce the thermal shock of the sample cooling from diamond deposition temperatures. Depositions using the higher microwave powers developed cracks after cooling of the sample. Higher temperature diamond depositions were found to lead to increased thermal-induced stresses following cooling of the sample. The residual stresses for the crack-free diamond films ranged

from approximately 4.5 GPa to 1.7 GPa as calculated using Raman peak shifting. Residual stresses were also measured using XRD data and found to agree reasonably well. Utilizing Rockwell indentation, adhesion was tested for both a thick and thin film. While the cracking pattern differed between the two, both appeared to remain adhered after testing as no white marks surrounding the crater appeared.

Weiser and Prawer [45] utilized a 3 μm electron-beam evaporated TiN interlayer deposited on only half of magnet iron substrates. After seeding with diamond paste abrasion, diamond deposition took place in a microwave plasma CVD system using a pressure of 20 Torr, H_2 flow of 99 sccm, CH_4 flow of 1 sccm, substrate temperature of 1050 °C, and a deposition time of 12 hours. Diamond films formed on both the TiN interlayer as well as the uncoated iron substrate. However, the diamond film on the bare iron only formed on top of a layer of graphitic soot. The coating delaminates within the soot layer as revealed by secondary electron emission spectroscopy of partially delaminated diamond film. On the TiN interlayer, no soot layer formation associated with the mutual diffusion of carbon and iron was observed. However, diamond adhesion was still relatively poor with cracking and delamination of the film occurring. Similar characterization of delaminated diamond coating revealed an interfacial amorphous carbon present which forms during the initial stages of nucleation, and the coating failure occured at the TiN and amorphous carbon interface.

Yet another interlayer approach was researched by Vieira and Nono [48] relying solely on a 0.5 um thick, pure Ti film deposited by electron beam process onto polished 304 stainless steel disks. Hot filament CVD was used for diamond deposition with a CH_4 mixture of 2.5 weight percent in a balance of H_2 and growth time of 4 hours. Pressure

was maintained at 50 Torr, and the substrate temperature was approximately 550 °C. SEM of the diamond film surface showed well-faceted polycrystalline grains. A sharp diamond peak was observed with a 3.2 cm^{-1} shift up as well as a broad graphitic band. Energy dispersive spectrometry revealed that Fe diffused into the Ti interlayer leading to good adhesion of the interlayer to the substrate. After diamond deposition, XRD revealed that most of the Ti was converted to TiC. This led to poor adhesion of the diamond film to the interlayer resulting from high residual stresses.

Borges *et al.* [50] used surface modification techniques of nitriding and carbonitriding to test their effectiveness to support continuous and adherent diamond films. 304 stainless steel was nitrided or carbonitrided by ion nitriding with input gases of N_2+H_2 for nitriding and N_2+C_2H_2 for carbonitriding. However, first a sputtering step of 30 minutes with only H_2 was used to remove the chromium oxide passive layer. The effect of H_2 flow relative to total flow on the nitriding process was studied and found to influence the amount of CrN present at the surface. Additionally, numerous Fe_xN_y were formed as well which can deactive the 3d-orbital of Fe and prevent the catalyst for graphite formation when depositing diamond. Diamond deposition took place by means of radio frequency thermal plasma torch using Ar, H_2, and CH_4. Uniform diamond films were grown on samples that had the largest amount of Cr present at the surface (those nitrided with the lowest levels of H_2). Diamond films grown on the substrates nitrided at 2.5% and 5% H_2 flow resulted in considerable delamination of the film upon cooling. The large Cr concentration was important as carburization of the surface took place at the start of the deposition leading to the formation of chromium carbides. The rough surface after nitriding was found to have a beneficial role in enhancing adhesion of the diamond

film as confirmed by mechanical scratch testing. Ultimately, continuous films as thick as 30 μm were grown on nitrided 304 stainless steel without the presence of cracking [50].

2. MATERIALS AND METHODS

2.1 Materials

Two grades of stainless steels are being utilized in this work. 440C martensitic stainless steel bearings of 9 mm diameter were explored first. Nominal composition for this grade of stainless steel is 1.1% C and 17% Cr in a balance of Fe. Maximum levels of additional elements include 1% Mn, 1% Si, 0.04% P, 0.03% S, and 0.75% Mo. Some bearings were pre-coated with a layer of TiN as evidenced by the gold coloring of the normally silver stainless steel. TiN coatings with a thickness of approximately 3 μm were applied by the PVD method of cathodic arc vacuum deposition (BryCoat, Oldsmar, FL). All bearings were ultrasonically cleaned in acetone and methanol for 15 min each followed by a 5 min ultrasonic rinse in deionized water. Seeding, a step prior to diamond deposition in order to provide nucleation sites for diamond grains to grow and ultimately coalesce into a uniform and continuous film [54], was achieved using ultrasonic agitation for 30 min in a 3:1 solution of methanol:nano-diamond slurry with average particle size of 4-5 nm and an average agglomeration size of 30 nm (International Technology Center, Research Triangle Park, NC).

316 austenitic stainless steel disks (ESPI Metals, Ashland, OR) of 7 mm diameter with a 0.06” thick sheet are utilized as the second material. The nominal composition of 316 stainless steel is 12% Ni, 17% Cr, 2.5% Mo, in a balance of Fe. Maximum levels of additional elements include 1% Si, 2% Mn, 0.08% C, 0.045% P, and 0.03% S. Multiple

disks were mounted in a hardened polyester resin mold with a 1" diameter steel disk placed on top to ensure planeness. Discs were then grinded using various SiC sandpaper and polished via diamond slurry applied to polishing cloths in conjunction with diamond extender solution. Following removal of the disks from the resin, they were ultrasonically cleaned analogous to the 440C bearings and ultrasonically seeded prior to diamond deposition.

316 discs were prepared from 12 x 6 x 0.06 inch sheet via a mechanical punch. Manual grinding was performed using SiC sandpapers starting at a low 120 grit and then successively increased in fineness till a final sanding at 1200 grit. Substantial material removal was necessary to obtain a flat top and bottom given the geometric deformation from the punching process producing a convex top and concave bottom to the disc. This was followed by polishing with consecutive diamond slurries of 9, 6, 3, and 1 μm. In order to remove the α'-martensite formed during cold rolling and potentially the punching process as well, an annealing step was incorporated to fully transform the microstructure to the γ-Fe phase. This was accomplished using an air furnace at 1070 °C. After the furnace reached temperature, discs were placed in the furnace which was then allowed to come back up to the original temperature set point. Discs were held at this temperature for 15 minutes in order to allow sufficient time for through heating. Discs were removed from the furnace and cooled in still air on a refractory brick. Significant scale formation was detected via XRD even following substantial delamination upon cooldown. While the remaining scale layer can be readily removed from the top and bottom of the discs while sanding flat, the sides of the disc are not as easily grinded given the small size and rounded profile of the discs. Thus, a second annealing method was

attempted to limit scale formation by annealing in a nitrogen atmosphere furnace to prevent the stainless steel from reacting with oxygen at high temperature. This was conducted using the same annealing conditions with the only change being the samples were in the furnace from the start to prevent opening it and exposing the atmosphere to oxygen. The samples were removed from the furnace and once more cooled in still air. This allows them minimal time to react with oxygen as they rapidly drop from the elevated annealing temperature.

An alternative method to punching to obtain the disc geometry from sheet metal was ultimately used and provided in the form of waterjet cutting. It is a unique method where ultra-high pressure water in conjunction with an abrasive powder (for dense materials such as metals) is used to cut various materials. A stream of water is accelerated through a nozzle at a pressure of 50,000 to 60,000 psi resulting in a diameter as small as 0.020 inch. Advantages of this method include no distortion or warping of the material, no heat affected zone as it is a cold process, low contact force, good edge finish, and high accuracy of ±0.001 in. Given the desired size of the discs being quite small, other methods such as plasma or laser cutting were not suited to the task. Discs were cut by Minnesota Waterjet, Inc. in Ramsey, MN and sanded using 400 grit, 600 grit, 800 grit, and 1200 grit sandpapers.

2.2 Methods

2.2.1 *Microwave Plasma Chemical Vapor Deposition*

Microwave plasma chemical vapor deposition is one of many forms of CVD where some input energy is used to dissociate reactant gases that ultimately deposit on a

heated substrate through chemical reactions near and on the surface. An exhaust system is used to remove unwanted by-products from chemical reactions as well as unreacted input gases. Given the wide ranging applications and uses for CVD to form various thin films and phase-pure, bulk materials, a range of systems with varying conditions can be implemented from sub-Torr pressures to above ambient and temperatures ranging from a few hundred degrees to over 1500 °C. CVD is an attractive choice for many reasons including its conformal film production, relatively high deposition rates, and the ability to deposit extremely pure materials. In the case of microwave plasma CVD, microwave radiation is the supplied energy source for ionizing the input gases to form a ball of plasma above the sample as seen in Figure 6. A common alternative to microwave plasma CVD is hot-filament CVD which uses a filament that is heated to initiate the chemical reactions.

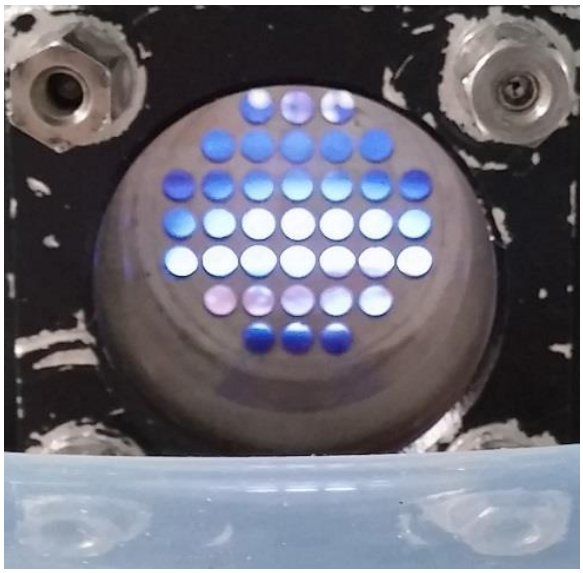

Figure 6: Plasma ball as viewed through an optical port and formed above the sample during a diamond deposition.

Immense research interest has been exhausted on the chemical vapor deposition of carbon films since the initial reports of diamond growth from the vapor phase as it was originally believed to only be possible under extreme conditions of high pressures and temperatures where diamond is the stable phase. Amazingly, diamond can be formed instead using very low pressures and moderately high temperatures using a mixture of hydrocarbon and hydrogen gases that are heated to initiate chemical reactions. Molecular hydrogen is broken down into atomic hydrogen through the application of input energy such as microwaves and plays a crucial role in allowing diamond to grow. It terminates dangling carbon bonds which could otherwise lead to graphitic formation and it preferentially etches graphite that forms. While atomic hydrogen will also etch diamond, the etch rate of graphite is substantially higher for CVD conditions used to deposit diamond films [55]. Two types of diamond growth can occur depending on the substrate: homoepitaxy growth on a single crystal diamond, which simply builds on the lattice already present, and heteroepitaxy deposition which results in a polycrystalline film such as on a non-diamond substrate. Heteroepitaxy diamond growth is the focus of most research, including this dissertation, and must be assisted through an additional processing step before CVD treatment. This is referred to as seeding and can be accomplished in a variety of ways; the overall goal is to form nucleation sites from which the diamond film can grow and coalesce by scratching the surface with diamond seed crystals that are embedded into the surface. A range of carbon based thin films can be deposited via CVD depending on the growth conditions and feedgas inputs including microcrystalline diamond, diamond like carbon, nanocrystalline diamond, and tetrahedral amorphous carbon with various grain sizes and ratios of sp^3 to sp^2 carbon composition.

The MPCVD system is comprised of several major components including the gas supply system, the microwave generator and power supply, the deposition chamber, and the vacuum and cooling systems. A picture of the UAB system with labeled components is shown in Figure 7.

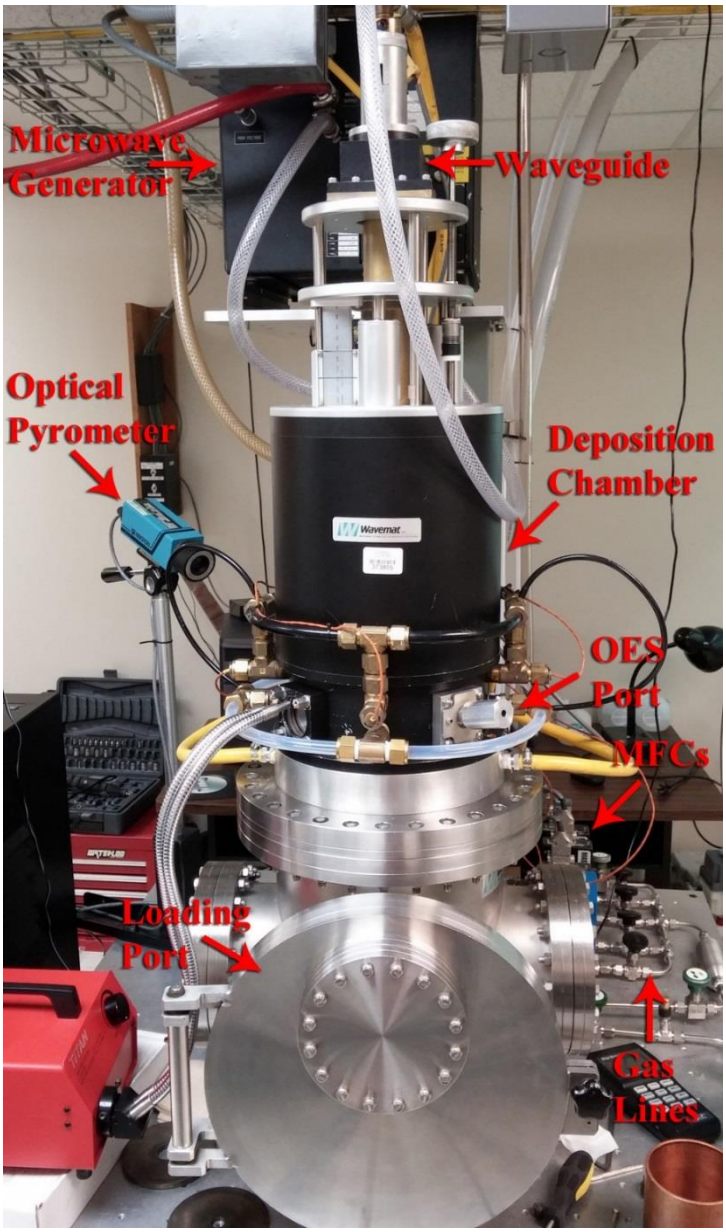

Figure 7: Microwave plasma chemical vapor deposition system illustrating key components including microwave generator, waveguide, deposition chamber, and gas lines.

2.2.1.1 *Gas supply system*. The gas supply system is comprised of high purity cylinders of H_2, N_2, CH_4, B_2H_6, He, and O_2 gases used for various areas of the experimentation. H_2 is present in both CVD diamond and boriding used to form the plasma and preferentially etch graphite, N_2 is used during NSD deposition, CH_4 is the carbon precursor used for CVD diamond, B_2H_6 is responsible for the diffused boron in surface boriding, He is used to backfill the CVD chamber to prevent contamination, and O_2 is used during plasma cleaning of the bell jar to remove deposits that could contaminate a coating deposition. Two-stage regulators connect the tanks to 0.25 inch gas lines which direct the various gases to the CVD chamber. Each gas line is connected to a mass flow controller (MFC) which allows for optimal control of the flowrate. The MFC for hydrogen gas has the highest maximum flowrate of 1000 standard cubic centimeters per minute (sccm). After the MFC, each gas line has a shut-off valve to prevent flow into the CVD chamber. Next, all gases enter a mixer for even distribution of the precursor gases. Diborane additionally has a second shut-off valve for safety precautions and a tuning valve to additionally control the flowrate manually as well as to prevent overshoot upon initial opening of the shut-off valve.

2.2.1.2 *Microwave generator and power supply*. The magnetron, rated for up to 6 kW with a frequency of 2.45 GHz, supplies the microwave radiation to the CVD chamber. The power supply can set the microwave power from 0.60 to 6.00 kW. A rectangular, metal waveguide is connected to the microwave generator to transmit the electromagnetic waves to the microwave cavity. Tuning of the microwave radiation is performed with adjustment of an excitation probe and vertical adjustment of a sliding

short for optimal resonant cavity height. Microwaves are operated in the TM_{013} mode for 2.45GHz. The microwave cavity has a diameter of 17.8 cm and its height is determined by the sliding short (about 21 cm for the TM_{013} mode) [2, 3]. Adjustment of both the probe and sliding short affects size and position of the plasma ball in addition to the reflected microwave power which must be minimized in order to ignite the plasma and prevent damage to the magnetron.

2.2.1.3 *Deposition chamber.* The stainless steel deposition chamber has a diameter of 18 inches and a height of 17 inches. The gases and reactions are contained by a fused silica bell jar that is transparent to the microwave radiation. The chamber features four optical ports, two of which are used for visibly observing the plasma, one for measuring substrate temperature with a Mikron M77LS Infraducer two-color infrared (IR) pyrometer, and the last for connecting an optical fiber to perform optical emission spectroscopy. A gas inlet is located on the side where the precursor gases enter the chamber. Multiple ports are present at the bottom of the unit such as connecting to the throttling butterfly valve, responsible for maintaining the desired operating pressure for deposition, which leads to the vacuum pump; another port is connected to the two pressure gauges for measuring pressures below (ultimate base pressure) and above (operating pressure) 10 Torr. A third port allows for the water cooling lines to connect to the stage. The largest port is where the sample is loaded onto the height adjustable stainless steel stage which is raised to the optimal position relative to the plasma and secured in place. Disassembly of the system is tedious but required for various repairs such as replacement of a damaged bell jar.

2.2.1.4 *Vacuum pump and cooling lines*. A scroll pump is used to achieve vacuum, maintain deposition pressure, and exhaust chemical byproducts and unreacted gases. A base pressure from 10-40 mTorr was achieved for most runs which is acceptable since homoepitaxy deposition is not the goal of this work. Water cooling is supplied by a chiller and reinforced tubing which is used to cool multiple system components including the power supply, microwave generator, chamber walls, sliding short, excitation probe, and stage. Water cooling allows for higher pressures and powers to be used while maintaining desired deposition temperatures to achieve higher growth rates. Additionally, air cooling is supplied to maintain acceptable operating temperatures of the silica bell jar. Bell jar temperatures are measured using thermocouples attached to the hot air exhausts after cool air has been warmed by the plasma heated bell jar.

2.2.2 *Raman Spectroscopy*

Raman spectroscopy is one of the main techniques used in the characterization of diamond films. It is able to differentiate between sp^2 and sp^3 carbon bonding. The various forms of carbon materials also exhibit characteristic spectral patterns when probed with this technique. Advantages associated with Raman spectroscopy when compared with other spectroscopy methods include the ability to examine samples in various physical states (solids, liquids, and gases), in a wide range of sizes (bulk, powders, and thin films), and without the need for lengthy sample preparation. Production of a Raman spectrum requires illumination with a monochromatic source of light. Lasers of various wavelengths depending on the application are utilized with

common selections including 632 nm red HeNe laser, 514.5 nm green argon ion laser, 325 nm ultraviolet He:Cd laser, or 785 nm near infrared diode laser.

Photons from the laser source can interact with the molecules of the sample by being absorbed or scattered, but they can also simply be transmitted without any interaction. Absorption occurs when the difference in energy between the ground and excited states of a molecule are equal to that of an incident photon causing the molecule to enter an excited state. Scattering does not require a photon to have the same energy as the difference between various energy levels of the molecule. Two types of important scattering of light in a molecule are Rayleigh and Raman scattering. If the incident photon polarizes the electron cloud of a molecule raising it to a virtual energy state, when it quickly drops back down to the ground state, it will release a photon. The energy of the scattered photon will be the same as that of the incident since the difference between the virtual and ground state is the same when being raised or lowered. This form of elastic scattering is known as Rayleigh scattering and the released photons can travel in any direction. Raman scattering on the other hand is an inelastic process which induces nuclear motion in the molecule. Energy can be transferred to the photon from the molecule or vice versa which results in a scattered photon of different energy than that of the incident one. Raman scattering is inherently a much weaker process where approximately one in every 10^7 photons will scatter in this manner. While this made observation of Raman scattering problematic in the past, modern day optics and lasers allow for extremely high power densities per unit area as well as the ever-improving state of modern detectors.

Two types of Raman scattering can occur: Stokes and anti-Stokes. As an example, Stokes scattering takes place when the molecule is initially in the ground state but is promoted to a higher energy vibrational excited state by the absorption of energy from an incident photon. If energy is transferred to the incident photon via the scattering process by the transition of a molecule initially in an excited state down to the ground state, this is known as anti-Stokes scattering. The relative intensity of these two forms of Raman scattering are dependent on the temperature of the sample as thermal energy results in a distribution of molecules initially being in an excited state for anti-Stokes scattering to occur. At room temperature, Stokes scattering is the dominant form of Raman scattering detected. Put simply, Rayleigh scattering results in elastically scattered light with the same energy while Raman scattering yields inelastically scattered light with a shifted energy in relation to the incident photon. The various forms of scattering during a Raman shift spectral measurement are illustrated in Figure 8.

The remaining components of the Raman system consists of optics which direct the laser to a microscope with objectives of various magnifications where it is focused onto the sample. The scattered light is then sent back through the microscope (one common system arrangement) where it passes through additional optics including a notch filter to remove the majority of wavelengths near the laser source produced by Rayleigh scattering and reflection. Light is separated by a monochomator into separate frequencies and focused onto a linear CCD where each point along the line corresponds to a certain frequency. The CCD is similar to the chips found in digital cameras and are silicon based multichannel arrays. Advanced cooling is often used as the detector must be extremely sensitive given the weak nature of Raman scattering which likewise enhances the

detection of background noise [56, 57]. Calibration of the detector is crucial prior to collecting any spectra to ensure accurate, reproducible measurements.

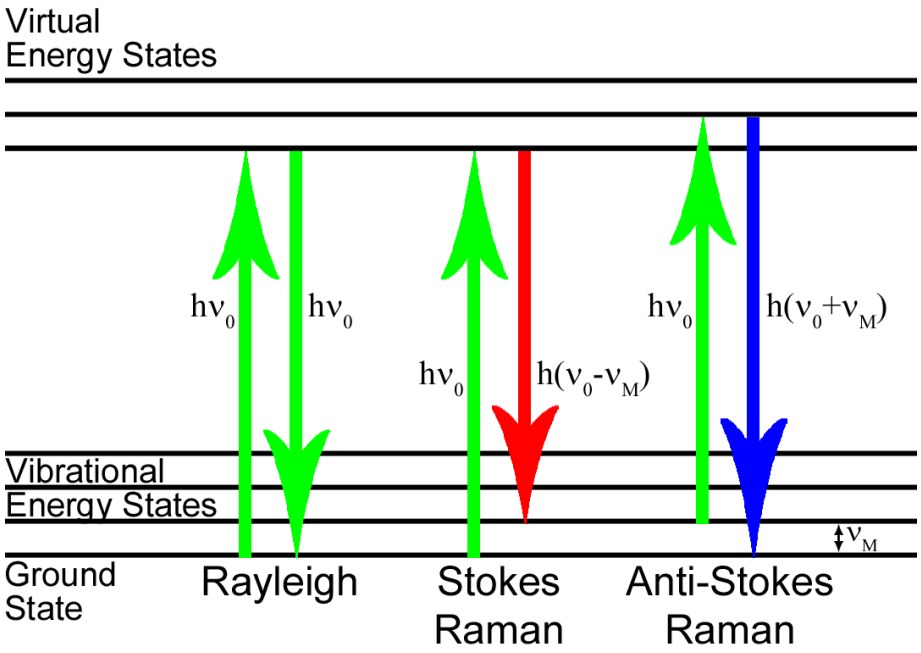

Figure 8: Scattering modes occurring during Raman spectroscopy including the dominant Rayleigh scattering and the two form of Raman scattering: Stokes and anti-Stokes. Energy of incident and scattered photons are included.

The UAB system uses a green solid-state (532 nm) frequency-doubled Nd:YAG from Dragon lasers. Neutral density filters with optical densities from 1 to 5 are part of the initial optics which can be selected to reduce the laser intensity or completely block its transmission without continually shutting the laser off between measurements while changing position on sample and refocusing. The microscope with varying objectives from 10x to 100x is used to focus on the sample location as well as the laser. At 100x, the laser spot size is approximately 5 μm. A SuperNotch plus filter (Kaiser Optical Systems) is incorporated that is centered at 532 nm with a 50 cm^{-1} width. The CCD detector (Princeton Instruments) is a 1340x100 pixel array format. Cryogenic liquid

nitrogen is used to cool the detector to an operating temperature of -110 °C. Argon and neon lamps (Oriel) are used as calibration sources prior to Raman signal detection. The measured signal from the lamps is then calibrated as the location of each peak as detected by the CCD (recorded as a pixel number) is then able to be corresponded to a certain wavelength given the known spectral positions.

Single crystal diamond, given its simple arrangement of carbon atoms in a cubic lattice structure with each atom tetrahedrally bonded to four neighbors, presents a trivial Raman spectra with a single sharp peak at 1332 cm^{-1}. Crystalline graphite also has a unique spectrum with the presence of two peaks located at 1355 cm^{-1} and 1575 cm^{-1} corresponding to the D and G bands respectively. The G band results from the crystalline nature of the graphitic structure whereas the D band arises due to the presence of disordered graphite. Amorphous carbon is an unstructured arrangement of both sp^3 and sp^2 bonded carbon. These films can have a wide range of characteristics and makeup such as the relative amounts of sp^3 to sp^2 content or the inclusion of large amounts of hydrogen which then determines the hardness of the material, resistivity, transparency, etc. Comparison of the relative content of the different bonding of carbon relies on the level of polarizability of the components. The σ-bonds of sp^3 hybridized carbon are vastly less polarizable than the π-bonds of sp^2 hybridized carbon which results in a greatly reduced scattering cross-section of the former in comparison. This does depend on the wavelength of the excitation source, and for a visible 514.5 nm laser source, the cross-section of the sp^2 phase is approximately 50-250 times greater than the sp^3 phase. Progressing to CVD films comprised of crystalline diamond, microcrystalline diamond films incorporate all three of the previously mentioned peaks: diamond, D band of

graphite, and G band of graphite. While the majority of these films is sp^3 bonded carbon in the form of microcrystalline diamond grains, there still exists the presence of sp^2 bonded carbon in the form of amorphous carbon. This occurs in the grain boundaries as well as at the surface of the film. Finally, reducing the grain size of the diamond crystallites to the nano-regime, we arrive at nanostructured diamond (NSD) films. These once again include the diamond peak, D band, and G band. However, structurally, the amount of sp^3 crystalline diamond has been reduced in favor of additional amorphous carbon. The general makeup of this type of film is the nanocrystalline diamond grains embedded in an amorphous carbon matrix. Beyond the three familiar peaks, two additional peaks arise at 1190 and 1350 cm^{-1} belonging to trans-polyacetylene (TPA). These molecules are composed of alternating chains of carbon and hydrogen and are found in the grain boundaries. When initially discovered with the early NSD films grown, they were believed to be attributed to nanocrystalline diamond grains. However, later, this was disproven and it was shown they are in fact associated with the presence of TPA [14, 15, 58, 59].

2.2.3 *X-ray Diffraction*

X-ray diffraction is a powerful technique for studying the arrangement of atoms within a material. Crystal structure refers to the unique arrangement of atoms within a solid. The unit cell is the smallest segment of the crystal lattice which is repeated throughout the crystal structure in three dimensions to form the bulk of the material. The unit cell can be thought of as a cube with atoms placed in an exact grouping within the unit cell. The simplest example is atoms only located at the corners of a cube which

corresponds to the crystal structure designated simple cubic. The cube is the unit cell with the highest level of symmetry given the edges of the cube are all of equal length as well as the edges being perpendicular. Unit cells also exist beyond cubic not requiring this level of symmetry. Whatever shape the unit cell takes, this is the simplest structure of the crystal lattice that is repeated throughout space. Given the arrangement of atoms in the unit cell, crystallographic planes arise that are important in determining the properties of the material. The easiest example referring back to the simple cubic unit cell would be one side of the cube. The plane is not confined to the single unit cell, but it is easiest to once again view in relation to this reduced, repeating unit. Another plane would be one that connects opposite edges of the unit cell which bisects the cube into equal halves. Because of the repeating nature of the unit cell to form the crystal lattice, these planes also repeat with a consistent separation distance, *d*, from one plane to the next. X-ray diffraction relies on these crystallographic planes. Diffraction experiments consist of an incident wave, such as x-rays, that are directed toward a material where they interact and are scattered at certain angles which a moveable detector can then identify. The wavelength of the waves must be on the order of the interatomic spacing for a diffraction pattern to result. X-ray diffraction relies on both coherent scattering and constructive interference. Coherent scattering does not involve energy transfer between the incident wave and the atom so it simply leads to a change in direction while maintaining the frequency and phase of the incident wave. Constructive interference results in certain scattering directions producing peaks in the intensity detected if multiple scattered waves arrive at a point in phase. These directions of constructive interference are highly dependent on the crystal structure, and specifically, the crystallographic planes of atoms

in the lattice. Bragg's Law is the key to understanding and defining the location of these observed peaks from x-ray diffraction. Looking at Figure 9, two crystallographic planes of atoms are shown horizontally and separated by a distance, d. Two incident x-rays approach the sample and are scattered off the two respective planes. Shown in red is the additional distance that the bottom ray travels. Knowing that the incident angle, θ, is the angle between the incident ray and the crystallographic planes, then it is trivial to show the triangles that involve the additional distance traveled also has an angle of θ as labeled. Using this angle and the interplanar spacing, each segment of the additional distance travelled by the bottom ray is equal to $d\sin\theta$. Finally, for the condition of constructive interference to be attained, this total additional distance must be equal to an integer number of wavelengths. This can be written finally as Bragg's Law:

$$2d\sin\theta = n\lambda.$$

In order for this equation to be satisfied in a diffraction experiment, one can vary either the detection angle or the wavelength of incident radiation. The Laue method uses a range of x-ray wavelengths which are directed toward a stationary, single crystal sample and the diffracted pattern produced can be used to determine crystal orientation. The more common approach is the Debye-Scherrer method which uses monochromatic radiation with a polycrystalline sample where the detector angle is varied while measuring the intensity [60, 61].

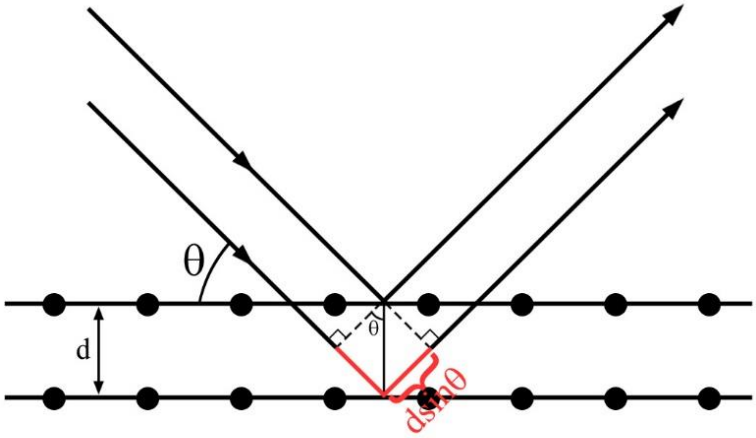

Figure 9: Geometry for Bragg's Law to be satisfied with the difference in path length shown in red for the bottom ray which must be equal to an integer number of wavelengths for constructive interference to occur.

The first requirement for an x-ray diffractometer is an x-ray source. This relies on the interaction of energetic electrons with an atom causing a loss of energy. An incident electron can be inelastically scattered by the atom where the lost energy is transferred leading to an inner core electron being ejected. An outer electron can then fall into this vacancy and an x-ray can be emitted from the atom as a means of disposing of the excess energy. This x-ray is known as a characteristic x-ray since its energy is equal to the difference between the two electron states involved in its creation. A ceramic sealed X-ray tube with a filament bias voltage of 40 kV and a tube current of 45 mA is the source used in the UAB diffractometer (X'pert MPD, Philips, Eindhoven, The Netherlands). The sealed tube features a stationary anode and cathode inside a metal/ceramic container under high vacuum. The cathode, usually a filament made of tungsten, is electrically heated which results in thermionic emission of electrons; these electrons are accelerated toward the anode as a result of the large potential established between it and the cathode causing the electrons to interact with the atoms of the anode to produce X-rays. X-ray

tubes have an extremely low efficiency of approximately 1% with most of the energy being converted to heat. This requires advanced cooling such as a chiller to prevent the anode target from melting. The UAB system uses a copper anode (Cu Kα, $\lambda = 0.154154$ nm), one of the most commonly implemented, which has the benefit of great thermal conductivity allowing for higher powers yielding a larger intensity of x-rays as well as improving the efficiency of characteristic radiation production. Even less of the total produced x-rays are used in the diffraction experiment as only a fraction exit through the beryllium windows of the x-ray tube. Additionally, the beam undergoes monochromization to eliminate the majority of x-rays other than the selected characteristic radiation desired and slits to limit divergence of the beam, both resulting in further reduced intensity of the incident x-rays. A filter can also be present to suppress the $K\beta$ characteristic x-rays in favor of the more intense $K\alpha$ radiation. The last two major components of the X-ray diffractometer are the goniometer and the detector. The goniometer is necessary to execute precise movements of both the sample stage and detector while the x-ray source is held fixed [60, 61]. The UAB system has two detectors: a gas-filled proportional counter and a silicon strip. The former is an inexpensive and robust detector with limited resolution, while the latter allows for high speed data collection without the need for exotic cooling. The diffractometer was run in grazing incidence mode in order to probe on the surface layer given the large interaction volume normally probed. A glancing angle of 3° was utilized and samples were measured in a 2θ range of 20-85° with a total scan time of 2.5-3 hours.

2.2.4 *X-ray Photoelectron Spectroscopy*

X-ray photoelectron spectroscopy (XPS) is an experimental method used not only for determination of elemental composition but also chemical bonding state. Additionally, it is a surface sensitive technique with an average analysis depth of about 5 nm making it an excellent choice for thin film characterization. UAB's PHI VersaProbe X-ray photoelectron spectrometer operates a focused Al Kα X-ray source (E = 1486.6 eV) at 25 W with a 100 µm spot size. A cold cathode electron flood source and low-energy Ar-ions provide charge neutralization. Spectra were collected at room temperature and at an argon working pressure of 2×10^{-6} Pa; the base pressure of the system was approximately 4 × 10−8 Pa. Survey scans were taken at 187.85 eV pass energy, with a 0.8 eV step; high-resolution scans were taken at 23.5 eV pass energy, with a 0.2 eV step. Sweep averaging was used to improve the signal to noise ratio to acceptable limits. Multipak v9.0 is incorporated to determine chemical bonding states of obtained spectra. Surface contamination is removed prior to data collection via Ar-ion sputter etching for 15 min at an accelerating voltage of 1 keV. The Ar-ion gun also provides the capability of depth profiling in conjunction with XPS measurements. Spectra were collected at room temperature

The guiding principle behind the use of XPS is the photoelectric effect which occurs through irradiation of a material with X-rays. This results in the liberation of electrons from the sample which possess discrete energies allowing for identification of elements present. During photoemission, a photon is absorbed by an atom which results in a core electron being ejected. The ejected electron leaves the sample with some kinetic energy that can be measured by the spectrometer and then related to the binding energy.

The sample and spectrometer use the Fermi level as a reference for measuring an electron's energy. An X-ray with energy, hv, produces a photoelectron with kinetic energy, KE_s, which is relative to the vacuum level of the sample. The work functions of the sample and spectrometer can be offset depending on the materials and they are designated by ϕ_s and ϕ_{spec} respectively. The kinetic energy of the electron as measured by the spectrometer, KE_{spec}, can be related to the contact potential difference (difference of the work functions) and KE_s. The binding energy can then ultimately be written as,

$$E_b = hv + KE_{spec} + \phi_{spec}.$$

Secondary emission processes follow with the ejection of core electrons: X-ray fluorescence or Auger electron production. These occur as a result of the hole left behind by the initial photoionized electron. An outer shell electron will fall to fill the core hole reducing its energy state, and the released energy leads to either the production of an X-ray or the ejection of a second electron known as an Auger electron. These secondary emission processes are the basis for other surface analytical techniques: X-ray fluorescence spectroscopy and Auger electron spectroscopy. The reason for XPS being a surface sensitive method is the ejected electrons must exit the solid without losing any kinetic energy. This only occurs near the top of the sample given the substantial possibility of an ejected electron interacting with another atom and being inelastically scattered. Thus, XPS is not a great choice for studying a bulk material, but it is well-suited for probing thin coatings and interfaces. In terms of spectral features, two are of the utmost importance. The first is the splitting of an elements peaks into doublets due to spin orbit coupling. This deals with the orbital angular momentum coupling between the magnetic field produced by the intrinsic spin of the electron and its angular momentum

resulting from "orbiting" the nucleus. An exchange interaction can occur between the photoelectron and the valence electrons depending on if they are parallel (triplet state) or antiparallel (singlet state). Splitting occurs only for the p, d, and f electron subshells, and the relative intensity is given by the ratio of the multiplicity for the respective levels. Thus for a 2p level with **J** equal to 3/2 or 1/2, the ratio of the peak intensity's would be 2:1. In addition to the higher **J** value having the larger peak intensity, it also occurs at a lower binding energy. The second feature in an XPS spectrum which is exploited is the chemical shifts observed for elements. Effort has been invested in attempting to calculate these binding energy shifts, but the factors that are involved are numerous and not fully understood. Thus, one uses experimental data in addition to any knowledge of the sample preparation to determine the various chemical states. The general idea behind the chemical shift is that the orbital position for an atom is susceptible to the chemical bonding conditions. The shift can be linked to overall charge on an atom where an increased charge results in a decreased binding energy which is determined by the molecular bonding [62-64].

There are several components comprising the X-ray photoelectron spectrometer. The most obvious is the X-ray source that is produced by firing an electron gun at an elemental target. Considerations must be met when choosing a source including the energy of the photons (to excite a wide array of photoelectrons) and their resolution. As an example, Cu Kα has ample excitation energy but its line width is more than desired for achieving good spectral resolution to differentiate between chemical states. The monochromatic sources of choice are Al Kα or Mg Kα, and used together, they can circumvent signal overlap. As with XRD, water cooling is required to prevent damage of

the anode and sample due to the high power requirements for sufficient photon creation. The second system piece is the vacuum pump. An ultrahigh vacuum environment (1 x 10^{-9} Torr) is needed to prevent photoelectrons from inelastically scattering before reaching the detector, to prevent damage to the anode, and to drastically reduce the time of surface contamination. Next, sample charging is offset using an electron flood gun which prevents the buildup of charge that would otherwise occur on nonconducting samples leading to erroneously measuring higher binding energies. The energy analyzer is another crucial component of the system which is the instrument allowing for not only element identification but also chemical bonding state. The detector is a concentric hemispherical analyzer (CHA) which can determine the intensity of electrons for a specified kinetic energy. Photoelectrons pass through electron optics which focus them to the entrance slit of the CHA. A potential difference is applied between the inner and outer hemispheres which will only allow photoelectrons with a certain kinetic energy to completely travel through the CHA's median path trajectory. Electrons travelling too fast will crash into the outer hemisphere and vice versa. The potential difference can then be varied to determine the intensity of electrons with various kinetic energies [62-64]. The last major system component is the argon ion sputtering gun. This is used to remove surface contamination such as adventitious carbon and oxides, and it also allows for depth profiling. Argon gas enters the gun where it is ionized by electrons emitted from a filament and the ions are accelerated toward the sample. Control of the accelerating voltage and time of sputtering varies the amount of material removed.

2.2.5 *Scanning Electron Microscopy*

Scanning electron microscopy (SEM) is a flexible technique that allows for high resolution imaging of surfaces and the analysis of chemical and microstructural composition. While optical microscopes directly image using visible light, they have a low achievable resolution (on order of 1 μm) due to the diffraction limit. Using electrons to image instead with their vastly reduced wavelength, especially at high accelerating voltages, can result in a resolution limit on the order of 10 nm. An additional advantage of SEM over optical microscopy is the large depth of field bringing more of the surface into focus, especially when large topographic features are present. Sample preparation is fairly routine for SEM, though surface contamination is readily seen at SEM magnification levels. Some nonconducting samples may need a metal coating, usually a thin layer of sputter coated gold/palladium in an argon atmosphere, to reduce charging and enhance electron emission for topographic imaging. UAB's SEM imaging system is a Quanta FEG 650 Scanning Electron Microscope (SEM) under high vacuum with accelerating voltages of 15 and 20 keV. Energy-dispersive X-ray spectroscopy (EDS) is performed with an EDAX TEAM EDS Analysis System to study elemental composition with distance using a step size of 0.1 μm and accelerating voltage of 4 keV.

Many types of signals are produced as a result of the electron beam interacting with the sample. Elastic scattering results in incident electrons being scattered through an angle greater than 90° after interacting with an atom's nucleus, and these are known as backscattered electrons (BSE). BSEs escape out of the sample's surface with an energy of at least 50 eV. They are highly influenced by atomic number as heavier atoms produce more BSEs which gives this imaging mode compositional data in addition to topography.

The large energy of BSEs means they produced at fairly large depths in comparison to another electron produced during SEM: secondary electrons (SE). SEs are the primary signal associated with SEM. These are loosely bound electrons that are emitted by interaction of atoms with the incident electron beam. They are of much lower energy with an average of about 4 eV which results in them only escaping from a few nanometers into the surface. SE images are used primarily for their topographic overview of the sample. Only SEs that are able to reach the detector contribute to the image which means surface features, angle of the incident beam, and the location of the detector all play a role in forming the SE image. As with XPS, both characteristic X-rays and Auger electrons can be produced through secondary emissions as an outer electron falls to fill an inner core hole. Characteristic X-rays can be used to obtain chemical information about a sample in addition to atomic concentration employing energy-dispersive X-ray spectrometry (EDS). Bremsstrahlung X-rays are likewise produced via inelastic scattering and they form the background noise of and EDS signal [65].

A diagram showing the major system components is seen in Figure 10. The main system component is the electron gun which is required to produce the stable electron beam. Early SEM systems used a tungsten hairpin cathode gun but more recent ones use a field emission source providing for lower energy spread, improved lifetime, and higher allowed currents. They utilize a single crystal tungsten wire that is formed into a sharp tip. An intense electric field forms at the tip which pulls electrons to the anode which are then accelerated by a secondary anode. Following the production of the electron beam, a series of electron lenses are used to focus the beam through magnetic fields. First, a condenser lens (or possibly two) and aperture converges and collimates the beam. Next,

the objective lens further focuses the beam to a small spot size on the sample's surface. Apertures are necessary to prevent scattered electrons from being included as well as to control spherical aberration of the final lens. A stigmator is incorporated to correct for astigmatism which occurs from lens defects and contamination of the column. Scanning coils are used to deflect the electron beam to various spots on the sample so that it can be rasterized to form an image. Multiple detectors can be included depending on the system requirements: solid state BSE detectors, the Everhart-Thronley detector for SEs, EDS for characteristic X-rays, etc. Similar to XPS, ultrahigh vacuum is required for SEM operation to prevent contamination and electron beam scattering. A combination of two different pumps, such as a diffusion pump and mechanical pump, are usually implemented, one for fast initial pump down of the loading chamber and a second to achieve the ultrahigh vacuum (10^{-9} Torr for field emission guns) [65].

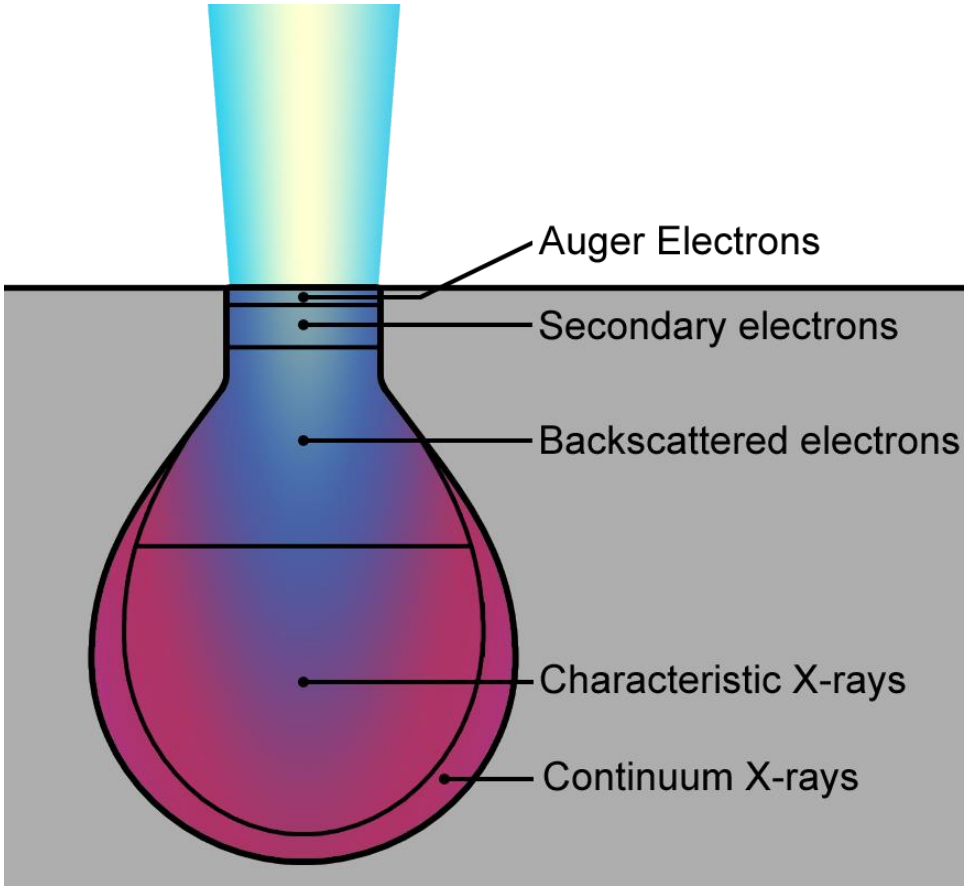

Figure 10: Interaction volume showing the various signals produced and the relative depths from which they are collected due to the electron beam interacting with the material.

2.2.6 *Atomic Force Microscopy*

Atomic force microscopy (AFM) is another imaging technique similar to optical and electron microscopes for studying the surface of a material while additionally providing three dimensional information and physical surface properties. Instead of using electrons or photons that are focused by lenses onto a surface, it relies on a sharp probe whose tip interacts with forces of the sample's surface. As with the other imaging methods, no diffraction limit is present to limit the resolution of AFM; only the sharpness of the tip and the cantilever spring constant are responsible for achieving better resolution. AFM can be operated in different modes which produce varying forces on the

tip. Contact mode brings the tip within a few angstroms of the sample where a strong repulsive force exists. The origin of this force is the exchange interactions resulting from overlap of the electron orbitals at these small distances. A secondary imaging mode operates under attractive forces arising from the Van der Waals interaction created by polarization of an atom inducing polarization of nearby atoms, and this is known as non-contact mode given the larger distance (5-15 nm) between the sample and tip. An intermediate operating mode is known as tapping mode which operates similar to non-contact mode with the cantilever continually oscillating but allowing the tip to impact the surface. This has the benefit of imaging the actual sample topography as opposed to any surface contamination that would otherwise result in a misrepresentation [66].

AFM uses a light lever for accurately measuring the forces between the surface and cantilever tip. A laser is focused on the back of the cantilever and reflects into a photodiode detector. This allows for measuring the varying deflection of the cantilever as it is scanned across the surface where the interaction forces change based on the surface topography. The bending of the cantilever causes the path of the reflected laser to change which is measured by the sections of the photodiode. Piezoelectric transducers, materials that respond precisely to applied potentials, are required for precise control of the position of the cantilever relative to the sample. Force transducers are used in AFM and can be capable of measuring forces on the order of 10 pN. Finally, a feedback control system is important for automated control of the system such as in contact mode where the deflection of the cantilever is kept constant as the probe is raster scanned across the varying topography. The z-piezo is continually altered to minimize the deflection change of the laser and this results in height data of the AFM image. In addition to imaging

topography, contact mode can be used to measure surface friction as the cantilever twists depending on the coefficient of friction, and in tapping mode, phase imaging can be performed by observing the phase lag between the driving signal and the cantilever output oscillation signal where properties such as elasticity and friction can be observed. Conveniently, both topography and the secondary phase imaging can be collection simultaneously [66]. The UAB atomic force microscope (AFM; Nanoink DPN5000) also has the ability to perform nanofabrication where the probe tip is coated with ink that is transferred to the substrate surface to write nanoscale patterns.

3. RESULTS AND ANALYSIS

3.1 440C Stainless Steel

3.1.1 *TiN Interlayer*

The first set of experiments focused on TiN coated 440C stainless steel bearings. A stage was designed and machined to allow for proper heat sinking of the bearings. This consisted of a titanium cylinder with a round indentation. The round inset allows for maximum contact between the bearing and holder for optimal thermal dissipation, and the inset itself drastically effects the temperature by controlling the amount of the ball exposed to the plasma (only the top third of the bearing protrudes out of the stage and is coated). Pressure was varied from 30-40 Torr and microwave power was adjusted from 0.60-1.20 kW with other parameters held constant. This led to a range of average temperatures during diamond deposition of 550-850 °C. First, the standard gas chemistry that has been well-studied at UAB for producing adherent and continuous nanostructured thin films on Ti-6-4 was implemented. This includes respective gas flows of 500, 88, and 8.8 sccm for H_2, CH_4, and N_2 [16, 17]. Figure 11 shows the XRD spectra for both a TiN coated 440C stainless steel bearing and a diamond film on a TiN interlayer. The α' peaks associated with a body-centered cubic lattice of martensite are observed in both spectra as well as peaks due to TiN. No crystalline graphite peak is observed at 26.5° in the coating which is required for an effective diffusion barrier and high quality diamond film. This is not a confirmation of the absence of sp^2 bonded carbon in the coating since XRD has

difficulty with detection of amorphous materials. After diamond coating, the relative intensity of the largest TiN peak with respect to the greatest intensity α-iron peak is reduced. Since the main diamond peak overlaps with this α' peak at 44°, this suggests the presence of at least a partial diamond coating on the surface of the sample. However, the secondary α' peak at about 64° likewise increases relative to the TiN peaks, but there is no overlapping diamond peak at this location. The (220) diamond peak should be observed near 76°, but no such peak is present in the spectrum of the diamond coated bearing. Thus, XRD is unable to solely confirm the presence of a diamond film. The change in intensity could be the result of heating of the steel during CVD processing resulting in grain refinement, or it could simply be due to an altered positioning of the bearing for the XRD scan.

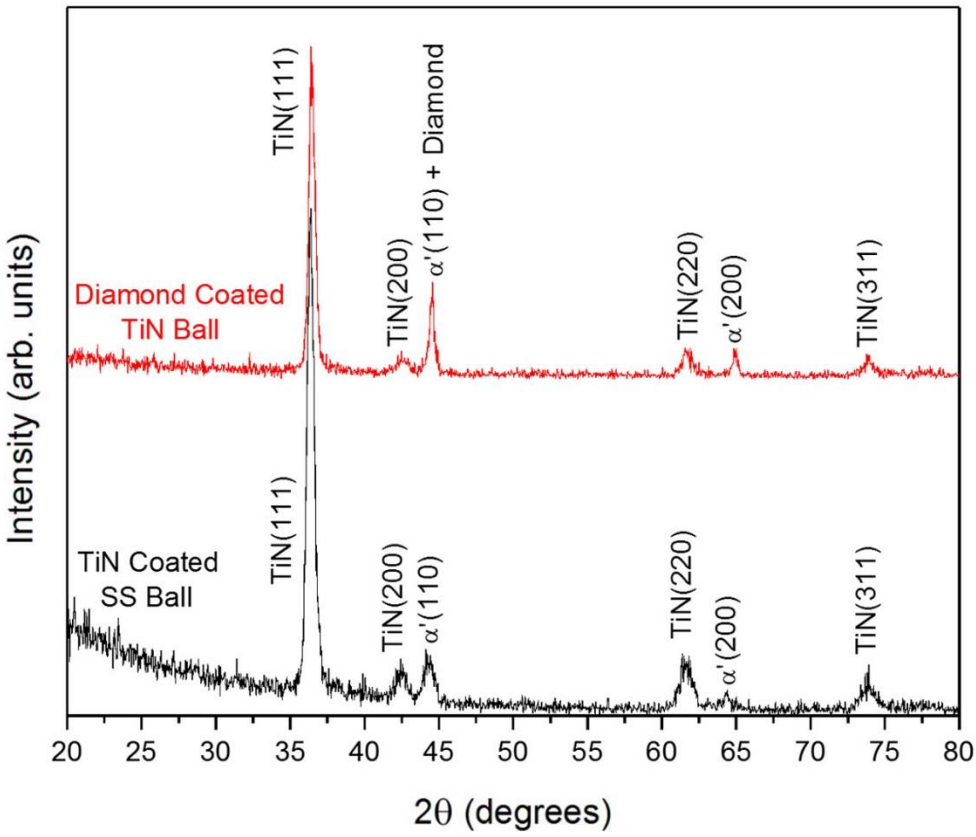

Figure 11: XRD spectra for both a TiN coated 440C bearing and a CVD diamond film on TiN coated bearing. TiN and α' peaks are seen in both spectra with no clear evidence of diamond and no interfacial TiC observed.

Raman spectroscopy is the main characterization technique for CVD diamond films. It is ideal for determining the quality of the diamond film as well as the presence of sp^2 bonded carbon in its various forms. Since it is commonly utilized, comparison of spectra with proven diamond coatings on other substrates is possible (such as Ti-6-4 where the same gas chemistry is known to allow for well-adhered nanostructured diamond films). The spectrum for each bearing was found to be very dependent on the position of the ball from where the laser spot was focused. Figure 12 shows a pair of spectra obtained from the same bearing. One scan is taken at the very top of the ball (red) while the other is taken half-way down the coated region of the bearing (black).

CVD conditions for diamond growth on this bearing include 40 Torr and 0.85 kW leading to an average temperature of 700 °C. Two peaks that are present for the middle scan at 1190 cm^{-1} and 1460 cm^{-1} are not observed in the scan at the top. These peaks are associated with trans-polyactylene (TPA) found in the grain boundaries of the film; they are not due to nanocrystalline diamond as was originally believed in academia [58]. However, they still are a common attribute of a Raman spectrum for nanocrystalline diamond films. The diamond component of the film can be observed near 1332 cm^{-1}. Slight down shifting of this peak is caused by residual stresses following cooldown due to the thermal expansion coefficient mismatch between diamond and the TiN interlayer. A peak at 1535 cm^{-1} for the middle scan is the G band associated with amorphous carbon consisting of both sp^2 and sp^3 bonded carbon. Variation in the G band including the shape as well as the position can be linked to the amount of order of the sp^2 phase, the ratio of sp^2/sp^3 content comprising the amorphous carbon makeup, and the inclusion of H and N in the film given their presence in the feedgas [14, 67-69]. The intensity of the G band peak is greater than that of the diamond peak, but this is due to the much larger scattering cross section of sp^2 bonded carbon versus sp^3 sites. Finally, a tail on the right side of the diamond peak near 1350 cm^{-1} is known as the D band and associated with amorphous carbon in the diamond film. The spectrum for the top of the bearing appears to have only two peaks located at 1350 and 1580 cm^{-1}. A double peak spectrum of these wavelengths are indicative of microcrystalline graphite [14]. This is an unexpected result since TiN should be an effective interlayer to block the diffusion of iron and prevent graphitization on the surface. The inconsistency in the coating could potentially be related to the spherical geometry of the bearing with various positions relative to the

plasma producing a range of temperatures on the surface with the temperature at the top not being ideal for diamond growth.

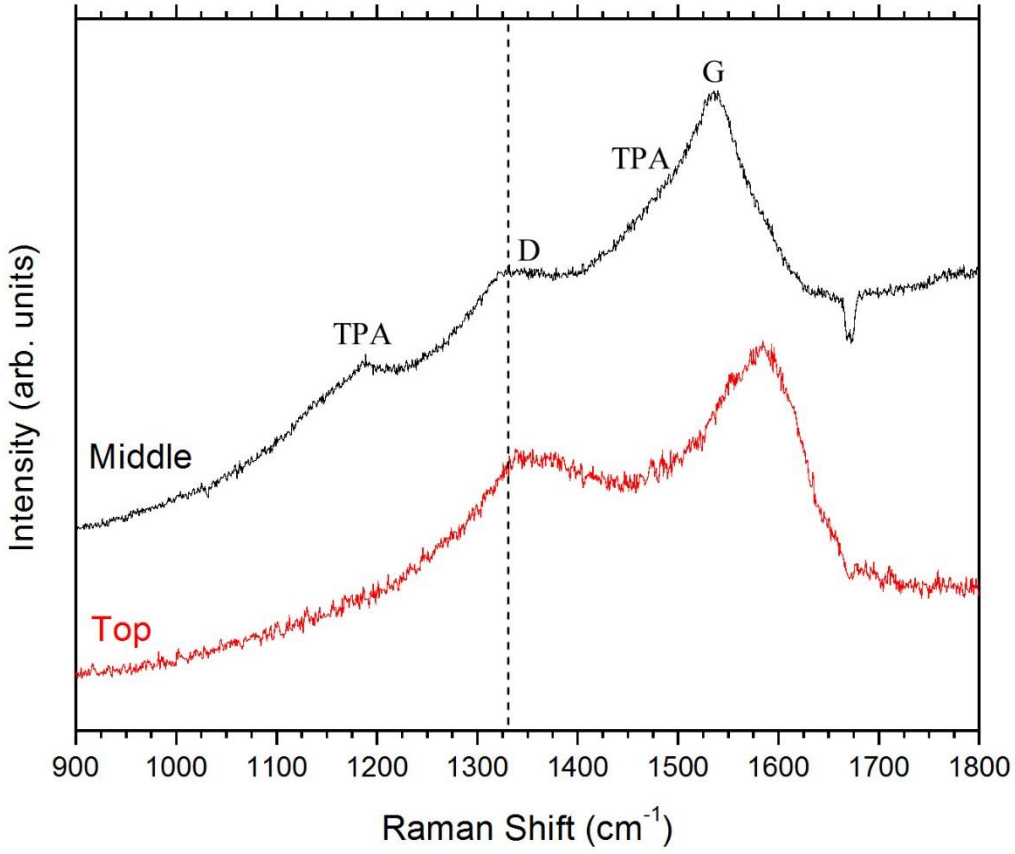

Figure 12: Raman spectra of a diamond coating deposited at 40 Torr and 0.85 kW at both the top of the bearing and midway down the coated area. An NSD signal is observed for the middle scan while microcrystalline graphite is detected at the top.

An additional set of spectra is shown in Figure 13 for a diamond coating deposited using the same gas chemistry and pressure but with a higher power of 1.20 kW. This applied microwave power resulted in an average deposition temperature of 780 °C. For the middle spectra, the diamond peak is observed at about 1320 cm^{-1}. The peak is much sharper corresponding to larger diamond grains and a higher quality film. This higher quality film also results in greater stress after cooling since the film is not as compliant

which is why such a large shift is seen from the expected diamond peak position. The tail on the right side of this peak again corresponds to the D band. Likewise, the G band is seen at approximately 1530 cm^{-1}. Finally, TPA peaks are present as well at around 1130 and 1460 cm^{-1}. Figure 13 also presents a Raman signal from the top of the diamond coated bearing. Compared to the previous TiN coated bearing with diamond grown at 0.85 kW, this signal differs somewhat. All peaks for an NSD film are observed in this spectrum as seen for the middle location. The diamond component is not as sharp or intense and the G band has a greater intensity similar to that observed for the 0.85 kW bearing's middle spectrum. The uniformity of this coating is obviously much improved and the lack of graphitic carbon is as expected and desired.

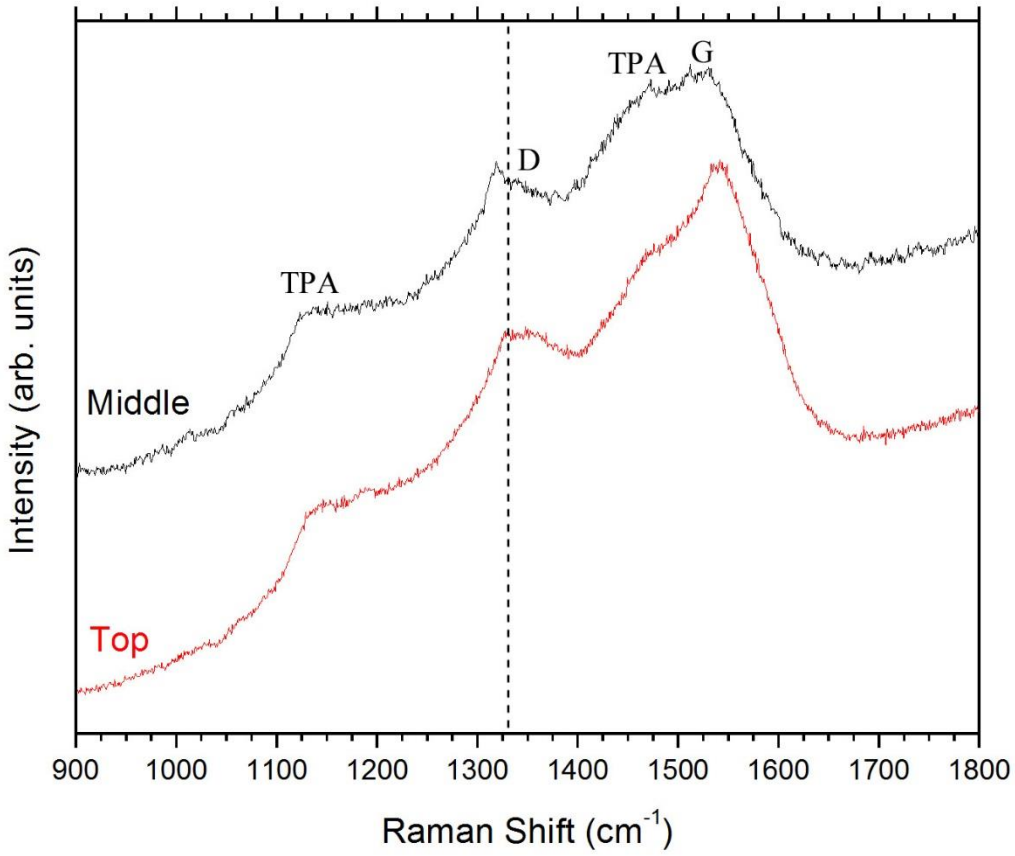

Figure 13: Raman spectra of a diamond coating deposited at 40 Torr and 1.20 kW at both the top and the middle of the coated surface. NSD signals are observed at both locations with a sharp diamond peak seen for the middle scan.

Finally, Figure 14 displays the Raman spectra for a diamond coating grown at 40 Torr and 0.60 kW leading to the lowest temperature of approximately 600 ºC. Scans for the top and middle are extremely well-matched and thus indicative of the most uniform coating deposited. Both display a broad peak from 1320-1400 cm^{-1} consisting of the diamond and D band peaks. Peaks at 1185 cm^{-1} in both spectra, while occurring at slightly higher Raman shift, are due to TPA. A sharp sp^2 bonded carbon peak of the G band is observed at 1550 cm^{-1}. A tail of this aforementioned peak on the left side at approximately 1490 cm^{-1} is additionally related to TPA.

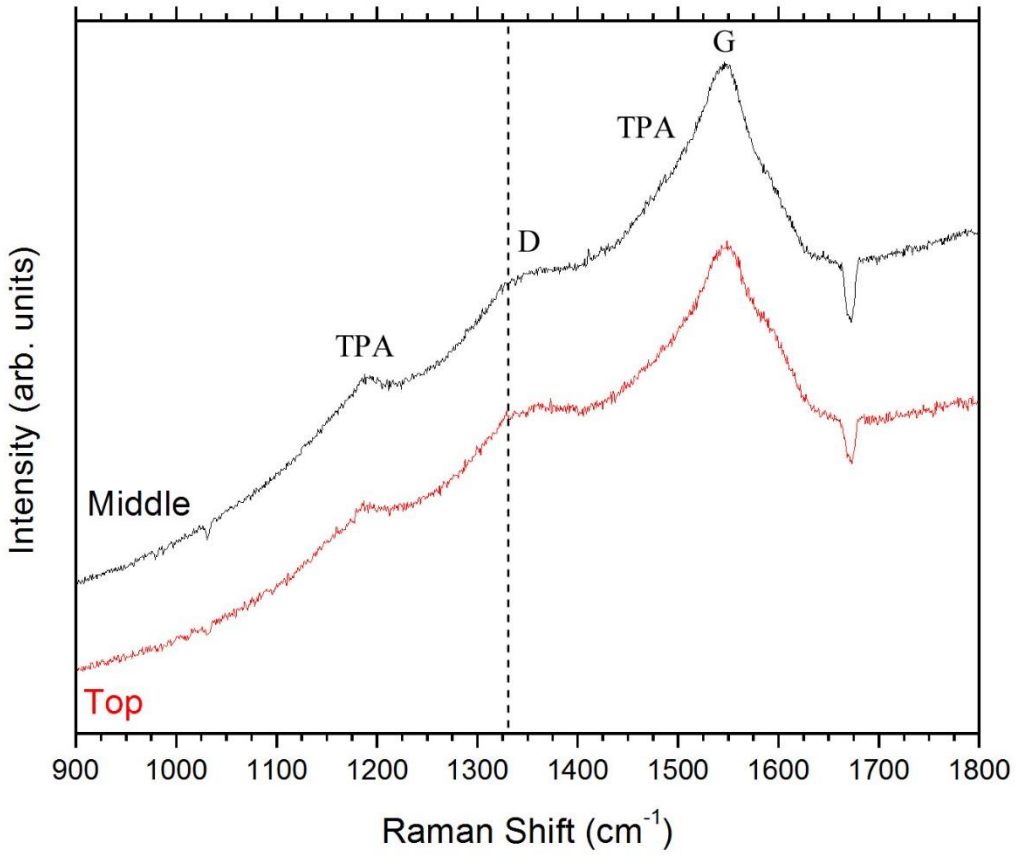

Figure 14: Raman spectra of a diamond coating deposited at 40 T and 0.60 kW at both the top and the middle of the coating. Well-matched spectra are obtained which contain all components of a common NSD spectrum.

Next, a diamond film was deposited using a lower methane flow of 10 sccm. Nitrogen flow was again maintained at 10% of the methane flow, or 1 sccm. The purpose of this was to grow a diamond film with a higher quality diamond component. Low temperature conditions produced the most uniform coating for the standard gas chemistry, so they were once more implemented. Deposition parameters include 40 Torr and 0.60 kW leading to an average deposition temperature of 590 °C. Three different Raman spectra, as opposed to only two for the previous scans, are shown in Figure 15 each corresponding to a different location on the coated bearing relative to the area that was

coated. The TPA peak at 1190 cm^{-1} is observed in the middle and bottom spectra only. The additional TPA peak near 1470 cm^{-1} can be observed as the tail of the G band for the top and bottom scans. It is least evident in the middle spectrum, though still present. A sharp G band is present at 1540 cm^{-1} for the middle and bottom, while a broader peak extending out to 1600 cm^{-1} is present for the bearing's top. The D band is not readily observed in the bottom scan relative to the strong background but has a strong presence at the top of the bearing. Finally, a strong diamond component is observed at 1322 cm^{-1} in all spectra as predicted. The middle and especially the bottom have a much sharper diamond peak than observed in most of the larger methane flow Raman spectra. This is obviously due to the lower methane flowrate resulting in higher quality diamond films and likely a larger grain size. The sharpest diamond peak occurring at the bottom is unexpected given the lowest temperature of the bearing occurring closest to the substrate holder. Quality diamond films are normally grown at higher temperatures since more sp^2 bonded carbon is deposited simultaneously at lower temperatures leading to a film of lesser quality.

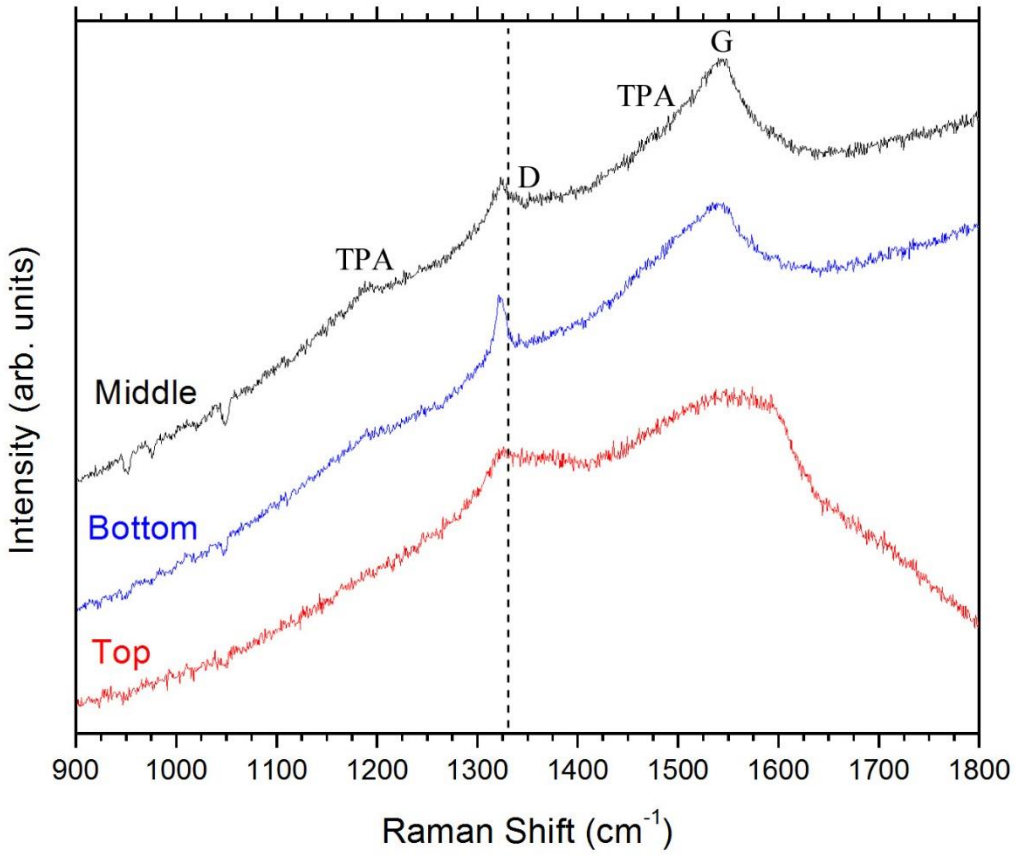

Figure 15: Raman spectra of a diamond coating using a low methane concentration deposited at 40 Torr and 0.60 kW at three different locations on the bearing: top, middle, and bottom of the coated surface. A sharp diamond peak at 1324 cm^{-1} is observed for the bottom.

Lastly for a TiN interlayer on 440C stainless steel, we consider the Raman spectra of a low methane flow gas chemistry grown at an increased temperature of 720 °C via CVD conditions of 40 Torr and 0.9 kW. The two spectra for the top and middle of the bearing are shown in Figure 16. TPA is again observed in both spectra with the 1190 cm^{-1} peak more prominent in the middle scan. The TPA peak at 1440 cm^{-1} as well as the G band command the bearing's top spectrum. The D band's presence is lacking in both spectra. However, the diamond peak is located around 1330 cm^{-1} in both spectra suggesting very small residual stresses. This is likely due to the extreme delamination

where only loosely adhered flakes remain following cooldown which has released most of the stress they would otherwise experience. The diamond peak is extremely weak at the top of the bearing suggesting a smaller presence and lower quality while the middle of the ball has an extremely sharp peak.

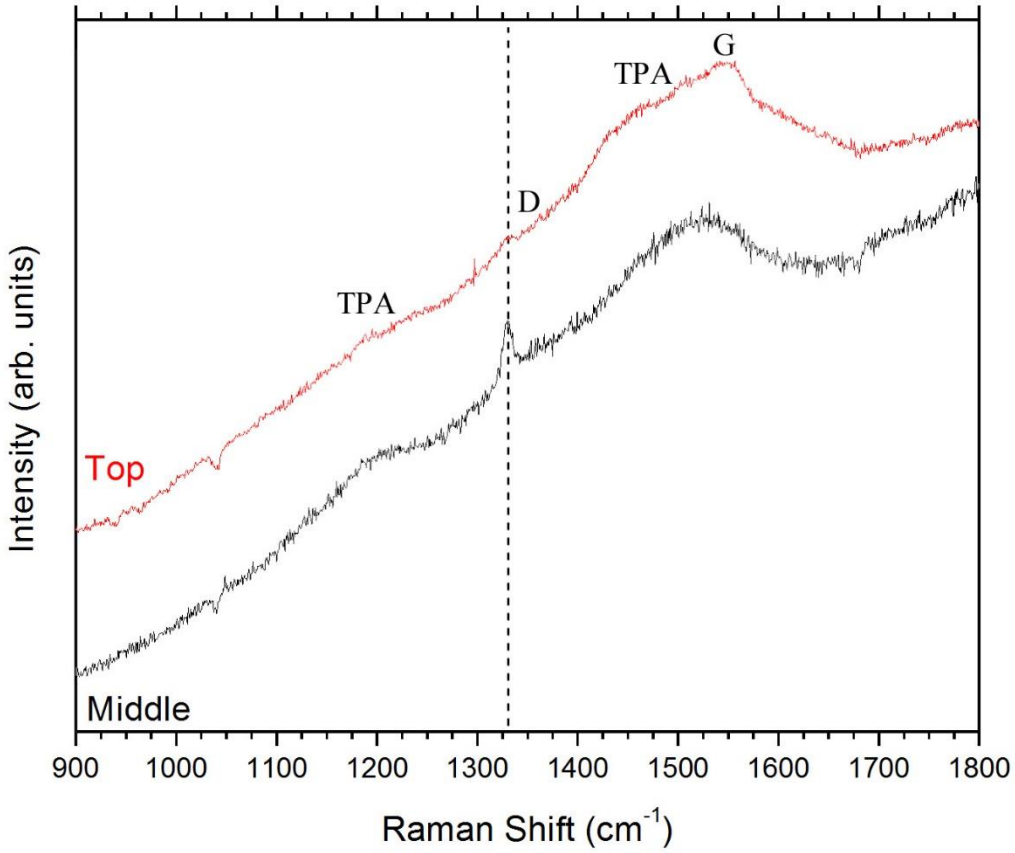

Figure 16: Raman spectra of a diamond coating using a low methane concentration deposited at 40 Torr and 0.90 kW at both the top and the middle of the coating. With most of the coating delaminated, flakes remaining in the middle region showed an intense diamond component.

NSD films were deposited on TiN coated bearings. Unfortunately, adherence was poor for all growth conditions. Lower temperature diamond depositions resulted in greater remaining surface coverage following cooldown; however, the coating flakes could still be easily removed simply by wiping with a cotton swab. The improved

surface coverage on lower temperature runs is likely due to lower residual thermal stress as a result of less cooling needed to reach room temperature after deposition because of coefficient of thermal expansion mismatch. Additionally, XRD spectra of diamond on TiN coated bearings showed no presence of an interfacial TiC phase which is a customary indicator of adhesion strength. This is in fairly good agreement with previous work of CVD diamond on TiN interlayers of iron or low alloy steels with the lack of an interfacial carbide forming, poor adhesion, and high residual stresses resulting in cracking and delamination of the film.

3.1.2 *Borided Interlayer*

Surface boriding as an interlayer is advantageous compared to TiN as it is a diffusion based interlayer without a discrete interface between the interlayer and stainless steel. Instead, a graded interface with a gradual change in mechanical properties. Two XRD scans are shown in Figure 17. These include an uncoated 440C stainless steel bearing and a bearing that has been borided at 740 °C for 1 hour and then diamond coated. Only two peaks are detected for the bare stainless steel: one at 44.2° and one at 64°. These peaks correspond to the α' martensitic phase (body-centered cubic) of iron which forms after the heat treatment procedure of austenitizing, cooling, and tempering. After boriding and diamond deposition, the α' peaks shift to slightly higher 2θ values and the peak at 64° becomes sharper. If a shift was present from the interstitial incorporation of boron which would likely lead to an expansion of the unit cell and thus edge length, it would be accompanied by a shift to lower 2θ. One possible explanation is residual stress in the film after surface hardening producing a shift in the diffraction peaks to lower 2θ

as observed for nitriding. The main α' peak shifts about 0.6° and the secondary peak at 64° shifts approximately 1.0°. Since the shifts are not equal, this is not a measurement artifact known as zero error. Two boride phases are able to be assigned to most of the peaks: FeB and Fe_2B. These are the common phases present when boriding steel which is expected. Two diamond peaks are able to be indexed at 43.8° and 75.5°. Finally, remaining peaks from 39.5° to 52° correspond to various chromium carbide phases, Cr_xC_y. The carbide phase(s) that forms prior to the diamond coating is encouraging and suggests some level of adhesion strength of the diamond coating to the boride interlayer. This carbide phase was not present for TiN interlayer depositions which likely contributed to the poor adhesion on those bearings. Additional peaks in the range of 60-66.5° of relatively low intensity are unable to be indexed to common boride byproducts. Of paramount performance is the lack of a peak at $2\theta = 26.5°$. This is the location for crystalline graphite that would readily form without the interlayer's presence. While not enough to confirm the interlayer as a successful diffusion barrier, it is an essential finding.

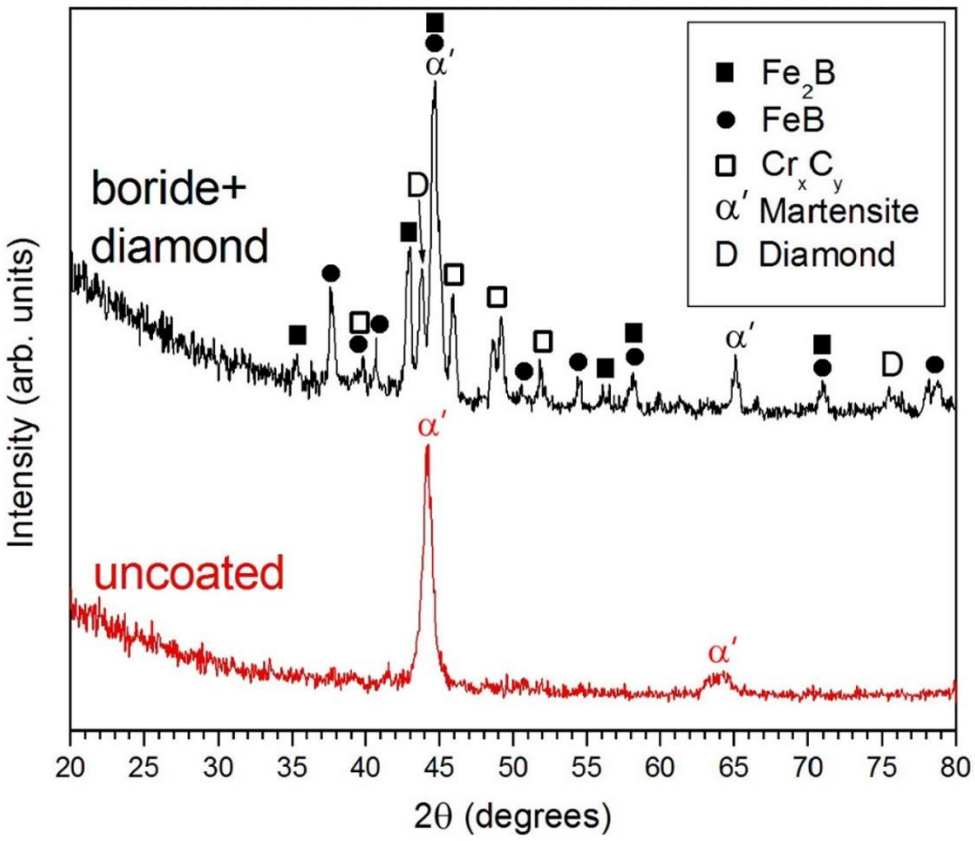

Figure 17: XRD spectra of a bare 440C stainless steel bearing and a 440C bearing with a CVD diamond coating on a boride interlayer produced at 740 °C for 1 hour. Martensite is the only phase present for the uncoated bearing, and after boriding and diamond deposition, multiple phases corresponding to various iron borides, chromium carbides, and diamond appear.

Figure 18 contains the Raman spectra of a diamond coated 440C bearing that was borided for 1 hour at 50 Torr and 0.67 kW resulting in a deposition temperature of approximately 750 °C. Gas flow rates include 500 sccm of H_2 and 2 sccm of B_2H_6. Diamond deposition occurred using the standard gas chemistry (500, 88, and 8.8 sccm of H_2, CH_4, and N_2 respectively) at 40 Torr and 0.60 kW yielding a deposition temperature of 640 °C. As before, spectra at multiple positions on the coated surface of the bearing were collected, and both scans contain the usual nanostructured diamond spectral features. TPA peaks at 1190 and 1470 cm^{-1} are present in both spectra. A broad peak

encompassing the diamond peak and D band stretches from 1300-1400 cm^{-1}. Lastly, the G band at the top of the bearing is much sharper and of greater intensity relative to the diamond peak. The diamond component at the middle of the ball is larger relative to the sp^2 bonding peaks.

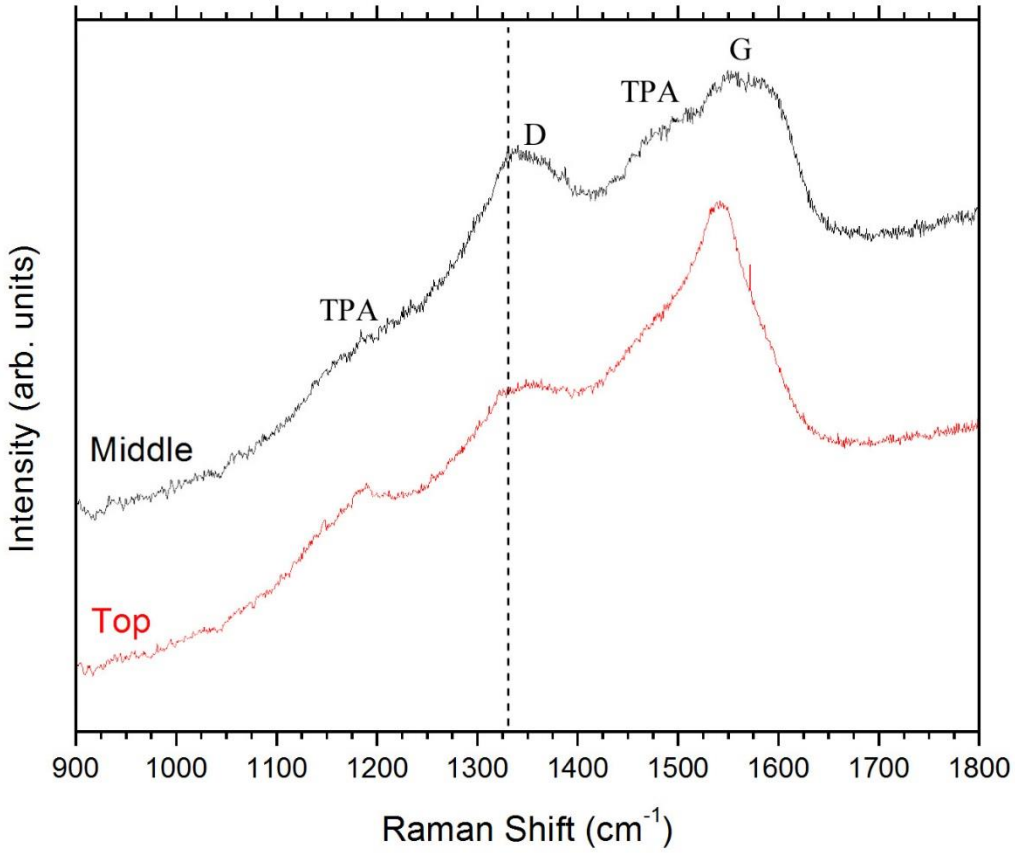

Figure 18: Raman spectra of a diamond coating on a borided bearing using the standard methane concentration and deposition parameters of 40 Torr and 0.60 kW at both the top and the middle regions of the coating. All NSD spectral features are present with slight nonuniformity observed due to the temperatures variation across the surface.

Various scanning electron micrographs are presented in Figure 19 of this same NSD coated 440C ball bearing. These correspond to secondary electron imaging mode using an accelerating voltage of 20 keV. In Figure 19 (a), a 600 μm^2 area is shown with dark areas being the remaining diamond film and lighter sections corresponding to areas

of delamination. A 10 μm^2 area seen in Figure 19 (b) shows a close-up of the diamond film. Clustering of the diamond grains into balls or what is commonly referred to as "cauliflower morphology" is observed. While the grains may be of small size, the clustering leads to a rough surface finish. Further increased magnification of the diamond film shows the nanoscale nature of the diamond grains in Figure 19 (c). The diameter of the largest grains is 25 nm. The image is somewhat blurry in comparison as the resolution limit of the SEM is approached. Finally, Figure 19 (d) is a 3μm^2 magnified view of a region of delamination. Many spherical particles are seen ranging in size from 250 nm to 30 nm. These remaining particles correspond to either interfacial Cr_3C_2 as was detected via XRD or borides that have nucleated on the surface of the stainless steel bearing. XPS with its surface sensitivity could potentially determine the composition, though precise placement of the beam on these fairly small delamination regions could be problematic.

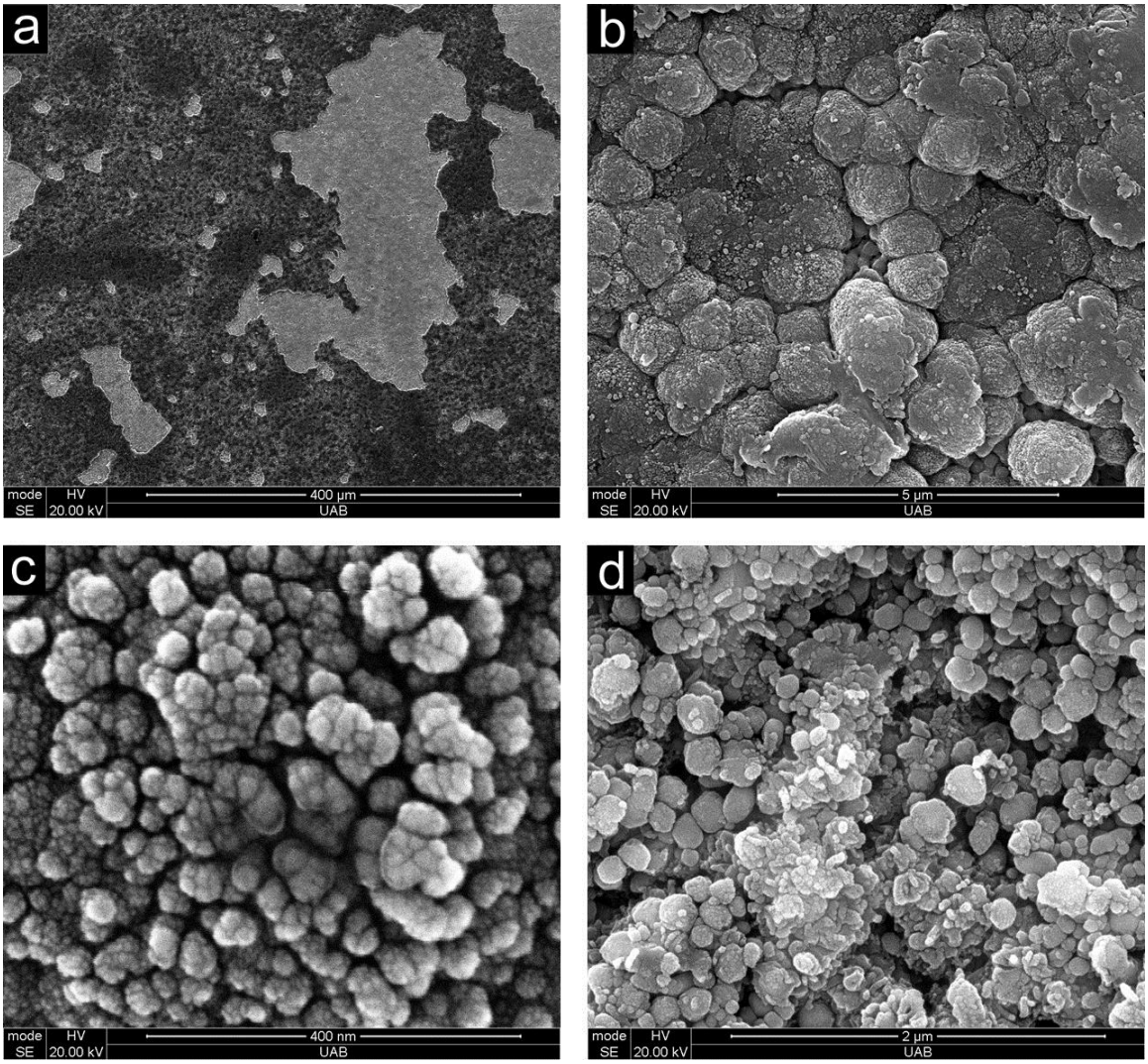

Figure 19: Scanning electron micrographs of the diamond coated 440C bearing whose Raman data was presented first. Low magnification image showing remaining diamond film (dark) and delamination zones (light) (a). Clustering of diamond grains (b). Nanocrystalline nature of film (c). Region of delamination (d).

A second 440C bearing was borided and then coated with NSD using the same CVD conditions resulting in almost identical deposition temperatures. The Raman spectra for this disc are seen in Figure 20. Almost identical spectra are produced at both the top and middle regions with the only noticeable difference being a slightly smaller G band in the middle spectrum compared with the previous bearing in Figure 18. This indicates excellent reproducibility of both the boriding and diamond deposition steps that

microwave plasma CVD is known to possess. Figure 21 displays three secondary electron images of this same 440C bearing. Figure 21 (a) is a 280x280 μm^2 region of the diamond film where dark areas correspond to delaminated regions or areas where the film did not coalesce and lighter regions are the adhered diamond coating. This lower magnification image allows for the evaluation of the overall adherence of the diamond film which is seen to be approximately 90% coverage. Figure 21 (b) is a magnified view of the diamond film. Once again, diamond grains cluster together into a rough cauliflower morphology. However, the size of the ball clusters appears to be smaller than before. This is likely due to the different position from which the SEM micrographs are obtained resulting in a different deposition temperature at this region of the coating. The images of the first ball were taken toward the top of the ball while the second set was taken near the middle of the exposed surface of the ball. Individual grains are not as easily discerned for estimating the individual crystallite size. Figure 21 (c) displays a higher magnification image in a region where the NSD coating either delaminated or did not fully coalesce. Many roughly spherical-shaped particles of varying in size are present. These are likely intermediate phases of chromium carbides that nucleate at the initial stage of the NSD deposition. Of critical importance is the tubular features observed within the image. These are most likely carbon nanotubes that often nucleate from transition metals such as iron. They pose a significant problem to NSD film adhesion and are therefore undesirable. They indicate the presence of elemental iron at the bearing surface in sufficient concentration to promote the formation of sp^2 bonded carbon.

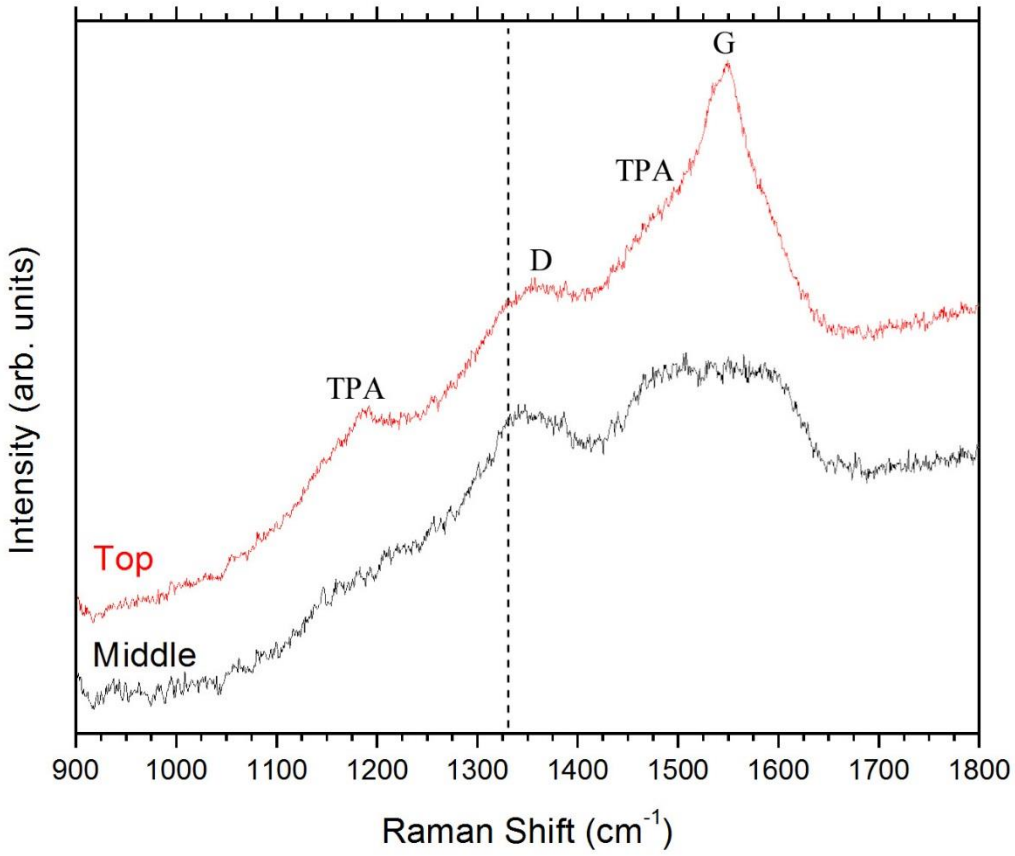

Figure 20: Raman spectra of a duplicate diamond coating on a borided bearing using the same parameters for boriding and diamond deposition at both top and middle coating positions. Very consistent spectra are produced at the relative locations compared to the previous bearing which confirms the reproducibility of the surface modifications.

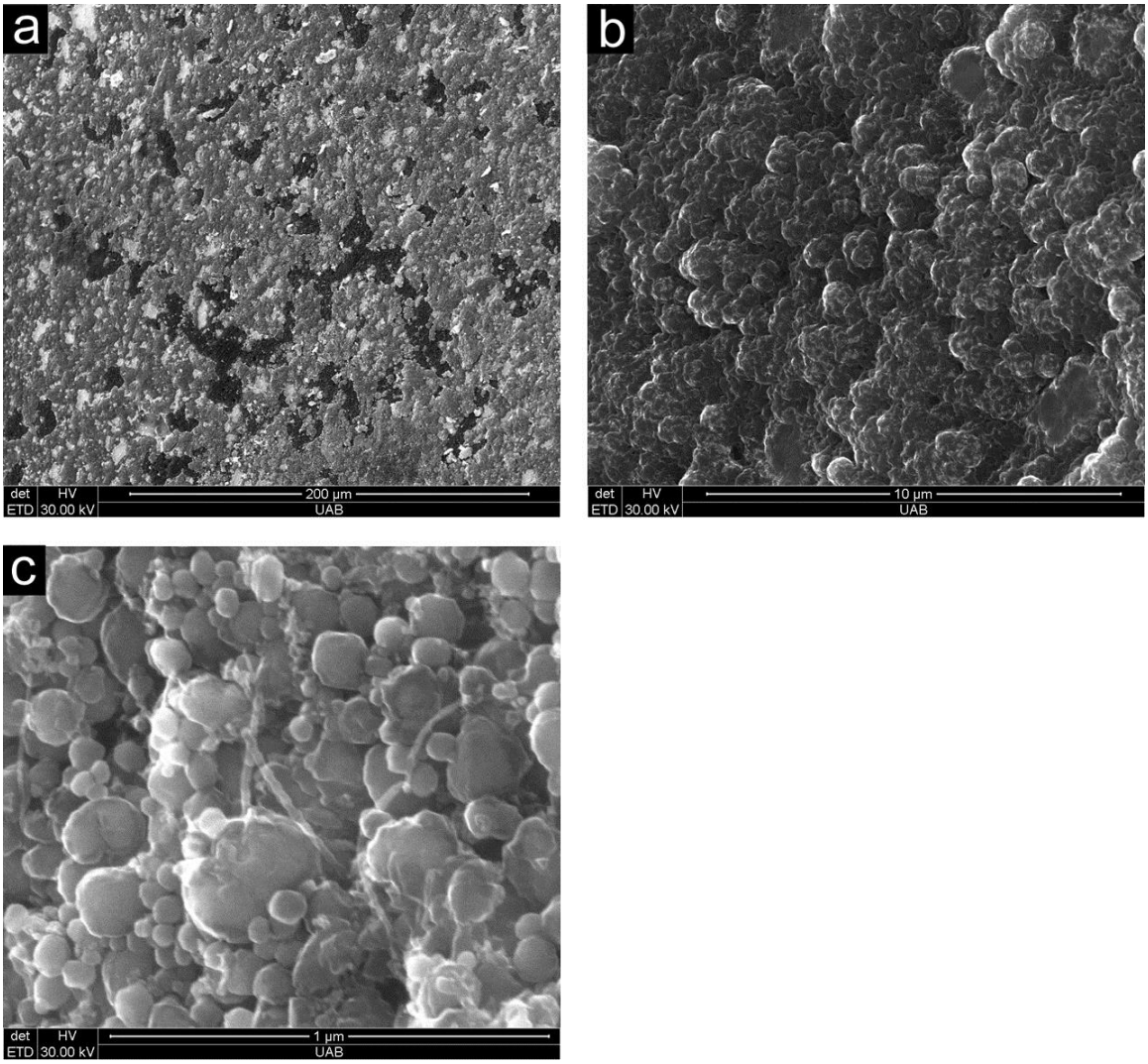

Figure 21: Scanning electron micrographs of the diamond coated 440C bearing whose Raman data was presented second. Low magnification image showing remaining diamond film (light) and limited delamination (dark) (a). Cauliflower morphology of diamond surface (b). Delamination region showing tubular structures (c).

A dual-phase boride interlayer of FeB+Fe_2B was formed on 440C stainless steel bearings. Following diamond deposition, XRD revealed the presence of an interfacial system of chromium carbides. This indicator of adhesion proved useful with films showing drastically improved adhesion strength compared to the use of TiN interlayers. Scanning electron micrographs of 440C bearings showed excellent coverage of the bearing surface which was likewise improved relative to TiN interlayers. However,

regions of delamination or where the film did not fully coalesce were still identified. Higher magnification of these zones showed grouping of spherical particles (likely chromium carbides or iron borides) with tubular structures on the surface. These probably correspond to sp^2 bonded carbon nanotubes formed by the presence of elemental iron. However, since they were observed on only one of the bearings and a multitude of these uncoated zones were not imaged, it is hard to make a definitive conclusion of the interlayer's ability to block iron outward diffusion. Finally, Raman spectra showed characteristic NSD signals with good reproducibility, but the clustering of diamond grains resulting in a rough surface morphology is not ideal for wear applications.

3.2 316 Stainless Steel

3.2.1 *Uncoated Stainless Steel*

A typical XRD spectrum of a punched and polished 316 stainless steel disc is shown in Figure 22. As expected, austenite (γ-Fe), which is face centered cubic (FCC), dominates the spectrum. However, a lower intensity phase attributed to α'-martensite (BCC) is also detected. This is the same phase that comprises the 440C stainless steel bearing and seen via XRD in Figure 17. This is referred to as deformation induced martensite and is a result of plastic deformation [70] such as during cold rolling to form sheet metal [71, 72]. Two mechanisms for this transformation include stress-assisted and strain induced with the latter happening at higher temperatures including room temperature. The kinetic transformation from the austenite phase to the α'-martensite phase include γ-austenite → ε-martensite → α'-martensite [73]. A direct transformation

is also possible through dislocation reactions: $\gamma \rightarrow \alpha'$ [74]. Many factors influence the amount of austenite that is transformed including the stainless steel composition, strain, temperature, grain size, and deformation mode.

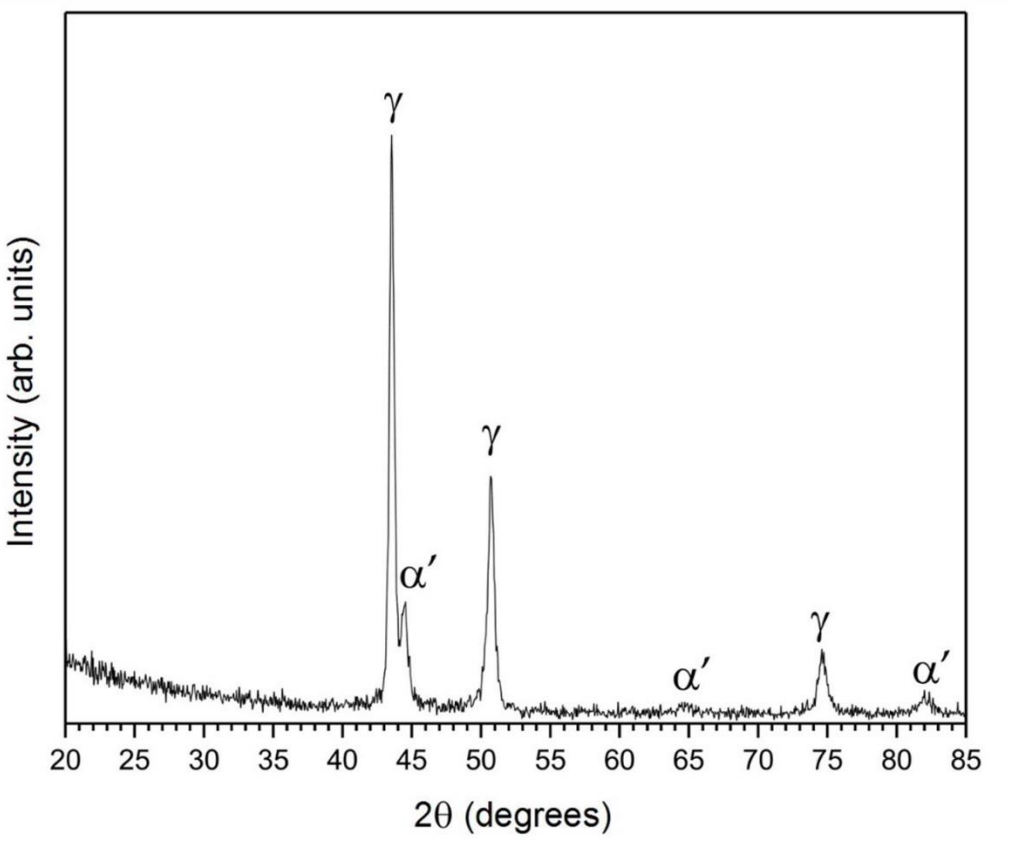

Figure 22: X-ray diffraction pattern of a bare 316 disc that was punched and polished.

In order to limit the amount of α'-martensite present in the 316 stainless steel discs, annealing in both air and nitrogen furnaces was explored. The addition of a protected environment substantially reduced the amount of scale formation as desired given the difficulty of scale removal from the side of the discs. XRD was performed on the annealed samples in both atmospheres after polishing, and the resultant patterns are shown in Figure 23. The relative intensities of the two primary peaks (43.6° for austenite

and 44.5° for α'-martensite) for each phase, $I_\gamma/I_{\alpha'}$, was approximately 3.5 for both discs. This is actually worse than that of the as-punched disc in Figure 22 (4.8).

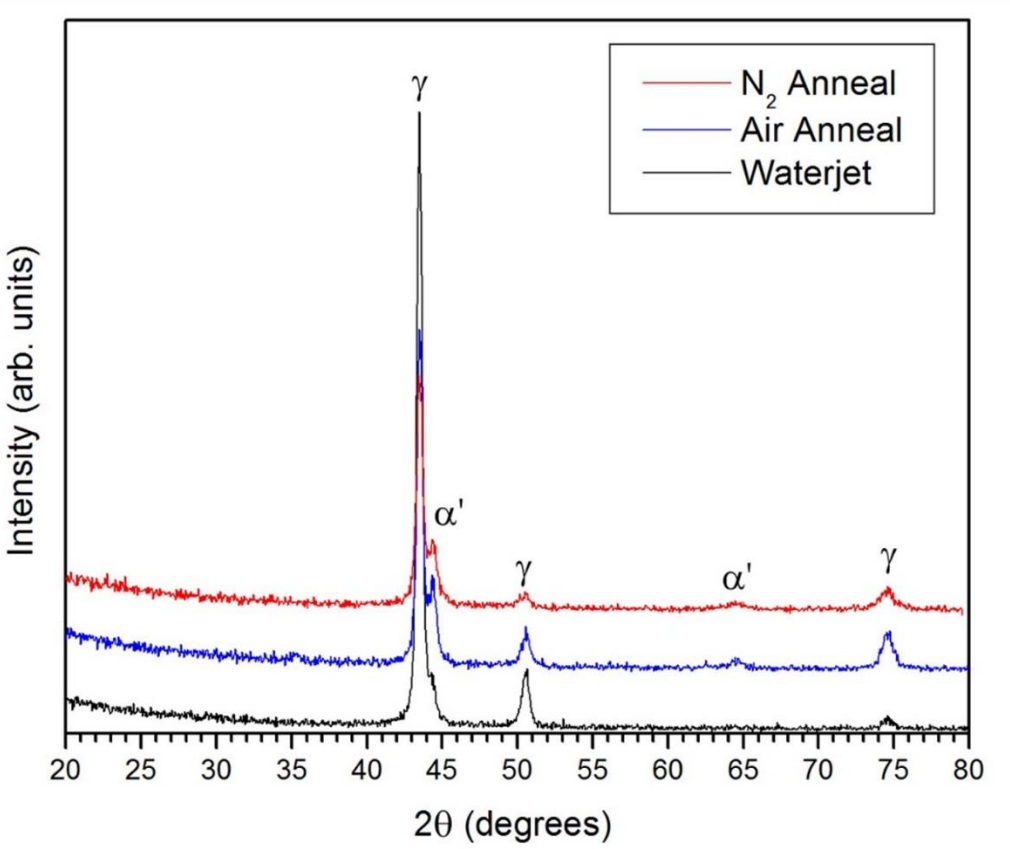

Figure 23: XRD scans comparing uncoated 316 stainless steel discs that are either punched, annealed, and sanded or waterjet cut and sanded to compare the relative amounts of austenite and deformation induced martensite.

In addition to the sheet's cold rolling, even sanding of stainless steel can provide the energy needed for martensite transformation [75]. Because punching of the discs results in curved surfaces on the top and bottom, heavy sanding is required on both sides to obtain a flat specimen. Starting at a substantially finer sandpaper such as 400 grit was a poor option given the amount of material that needed to be removed. Thus, a different method was researched to obtain discs cut from sheet metal which could maintain the parallelism of the disc's top and bottom. Waterjet cutting proved to be the most attractive

alternative to overcome this problems of punching. An XRD pattern of a representative disc of waterjet cutting followed by less destructive sanding is also shown in Figure 23. This scan obviously has the least amount of deformation induced α'-martensite compared to the desired austenite phase. Thus, waterjet cutting with its maintained parallelism allows for a less aggressive initial sanding step leading to less plastic deformation on the surface which is responsible for the martensite presence.

CVD diamond was deposited directly onto a 316 stainless steel disc as a comparison for later diamond depositions on surface nitrided and borided interlayers. An XRD pattern of a diamond deposition with conditions of 40 T, 0.70 kW, 500 sccm H_2, 44 sccm CH_4, and 2 sccm 4.4 sccm N_2 resulting in an average temperature of 630 °C is presented in Figure 24. Numerous peaks are detected corresponding to various carbides in addition to the base metal austenite and martensite. Surprisingly, no crystalline graphite is detected at 26.6°, though this likely delaminated with any diamond that formed on top. A set of Raman spectra for a direct diamond deposition without an interlayer is presented in Figure 25. These spectra contain primary peaks c.a. 1350 and 1580 cm^{-1} but no well-resolved crystalline diamond component located at 1332 cm^{-1}. This is a similar spectrum to what is seen for multi-walled carbon nanotubes composed solely of sp^2 bonds. The two spectra correspond to different locations on the surface of the disc to probe variation in the deposited coating. The spectra here show little variation at the different locations indicating a uniform deposit.

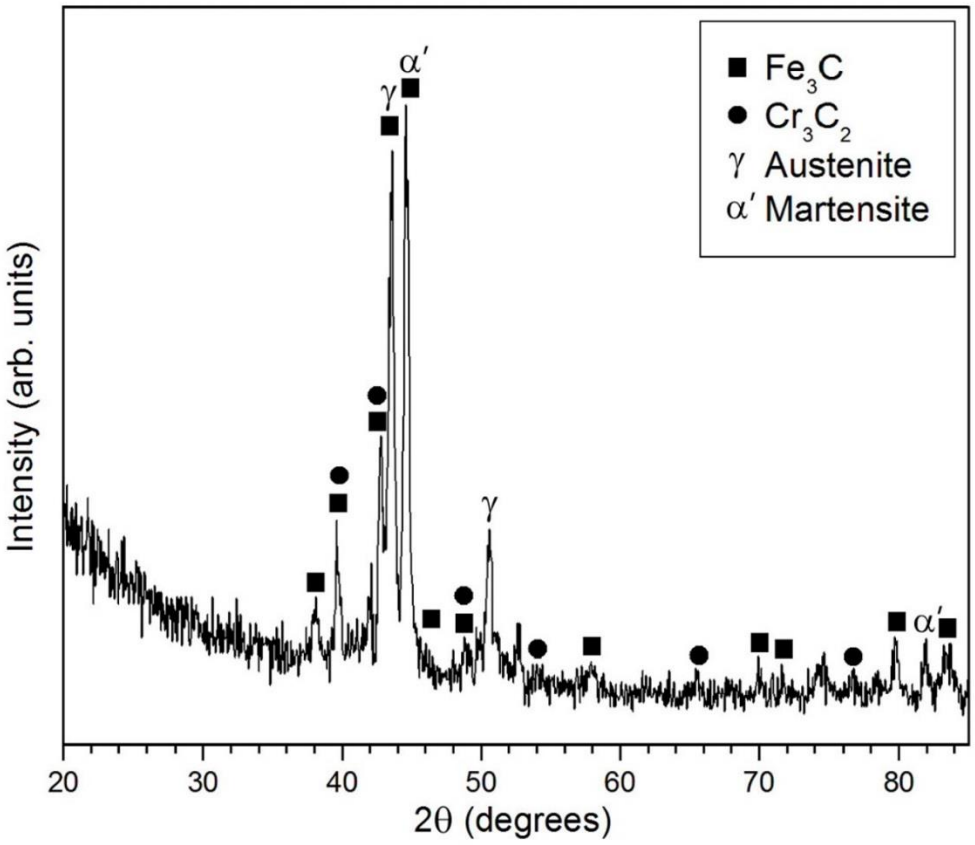

Figure 24: XRD pattern of a direct diamond deposition onto 316 stainless steel showing various carbide soot formation and the base metal peaks.

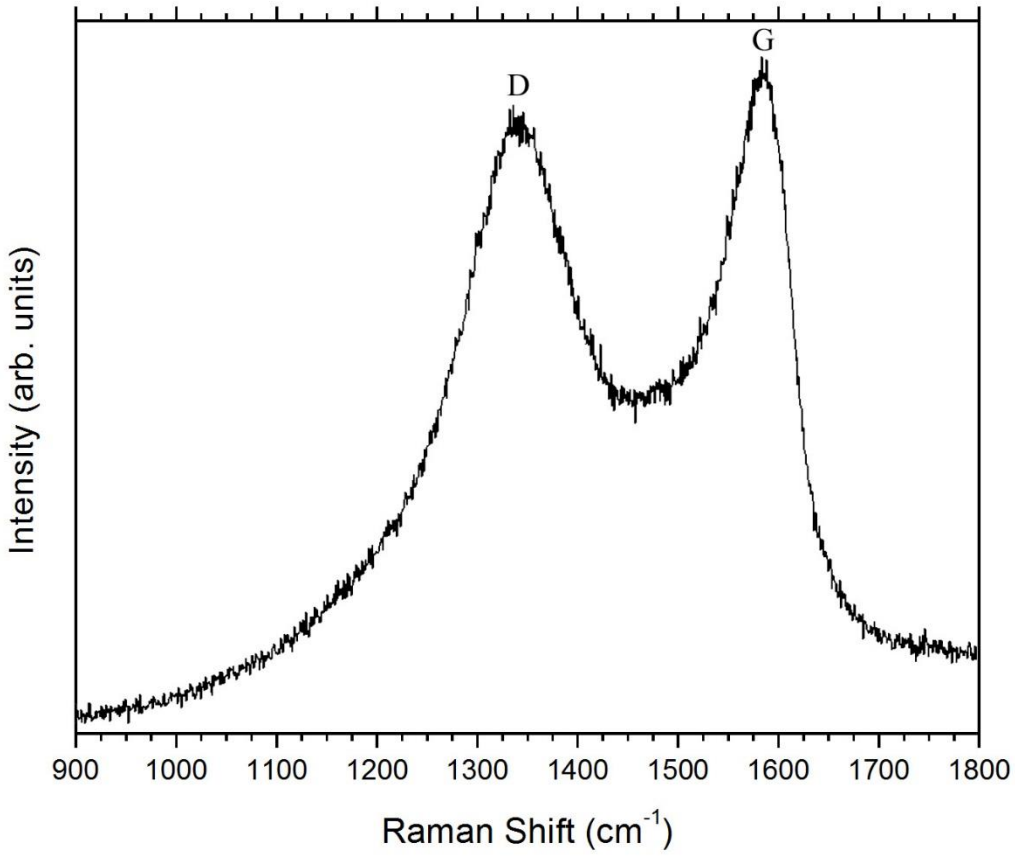

Figure 25: Raman scan of a direct diamond deposition on 316 stainless steel displaying a double peak spectrum indicative of sp^2 bonded carbon.

Deformation induced martensite, resulting from cold rolling and surface preparation, is an issue for austenitic stainless steels which can influence the physical properties. Attempts to produce phase pure austenite were not wholly successful, but substantial reduction was achieved by waterjet cutting combined with less aggressive sanding. Attempting direct diamond deposition onto stainless steel results in sp^2 bonded carbon and various carbide soot that is poorly adhered. Any diamond that does form during the CVD process readily delaminates upon cooling and is not detected via XRD or Rama spectroscopy.

3.2.2 *Borided Interlayer*

Given the promising results of borided surfaces as an interlayer for subsequent diamond deposition on 440C stainless steel bearings, the work was continued on 316 stainless steel discs. XRD studies were conducted on as-borided 316 discs to determine the effect of temperature on the metal boride phases present at the surface. CVD parameters were varied to achieve a range of starting temperatures from 550 to 800 °C in 50 °C increments. Figure 26 shows a typical XRD pattern for a disc borided at a starting temperature of 550 °C. Only one metal boride phase was detected in the XRD pattern beyond the expected face-centered cubic austenitic iron peaks associated with bulk stainless steel. All peaks beyond those of the 316 stainless steel base metal can be assigned to orthorhombic CrB. Neither of the two iron boride structures that commonly result from the pack boriding process (Fe_2B and FeB) were detected. However, the pack boriding process is usually done at temperatures over 800 °C. Figure 27 shows three XRD patterns for 600 °C, 650 °C, and 700 °C. In addition to the single detected phase in the low temperature boriding, a second metal boride phase is also observed in these scans: Fe_2B (body-centered tetragonal). Austenite is present in the 600 °C XRD pattern but is only minimally observed in the 650 °C and 700 °C patterns. While a thicker coating should be obtained at higher temperatures, the lack of any austenite is surprising, especially at only 650 °C. The amount of CrB appears to be diminishing in favor of more Fe_2B as the temperature is increased. From this data, one would expect the CrB to eventually disappear altogether if the temperature is repeatedly elevated. Figure 28 displays two more XRD scans at 750 and 800 °C. From these patterns, it does indeed appear that CrB has vanished and the singular metal boride phase of Fe_2B exists.

Therefore, we find that for the range of boriding temperatures studied, increasing temperature results in the sequence of phase formation given by: (CrB) → (CrB+Fe_2B) → (Fe_2B). This demonstrates that boride stoichiometry can be easily tailored by adjusting substrate temperature during CVD processing. While all phases may not prove useful as an interlayer for subsequent NSD growth (depending on factors such as diffusion characteristics, microstructure, fracture toughness, etc.), it allows flexibility in finding an effective interlayer through CVD plasma boriding. At no point was the relatively brittle and undesirable FeB phase detected via XRD as a result of MPCVD boriding on 316 stainless steel.

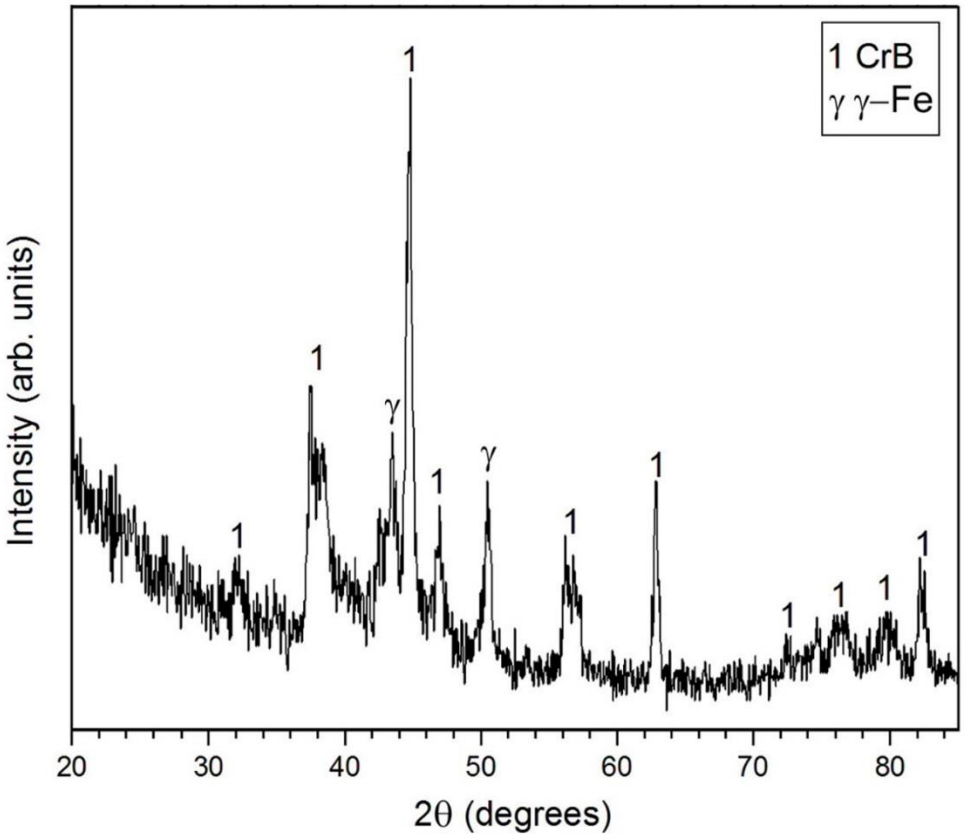

Figure 26: XRD pattern of 316 disc borided at a starting temperature of 550 °C. CrB is the only phase detected in addition to austenite.

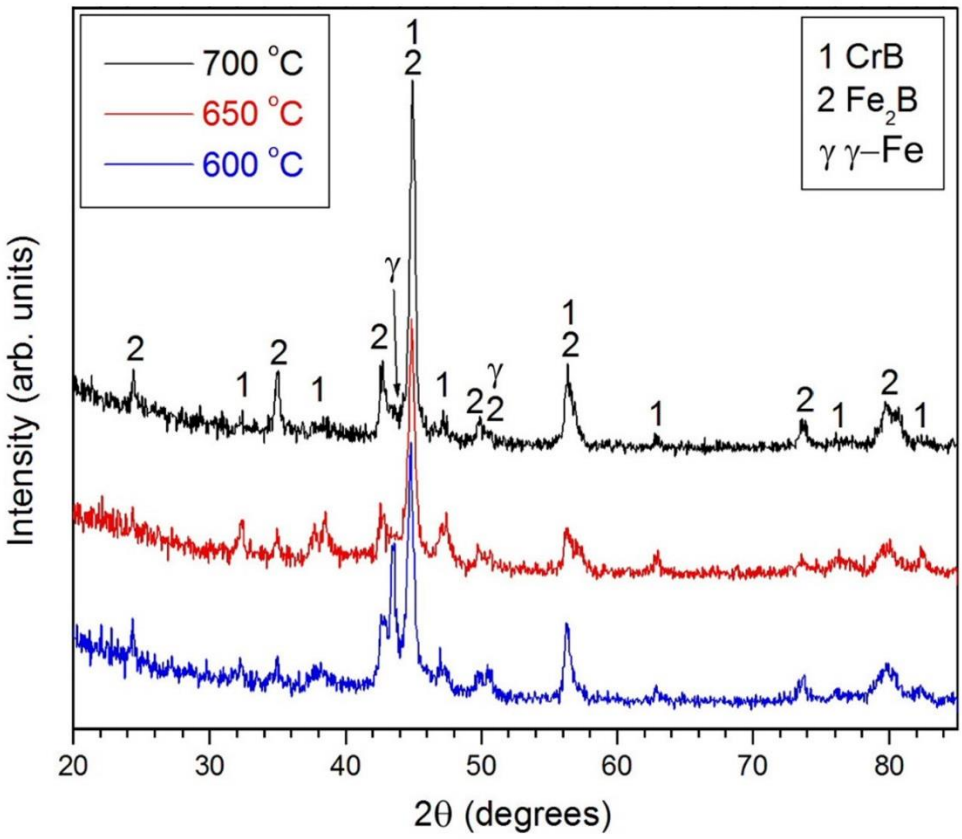

Figure 27: XRD patterns of discs borided at starting temperatures of 600, 650, and 700 °C. Both CrB and Fe_2B phases are present in addition to austenite.

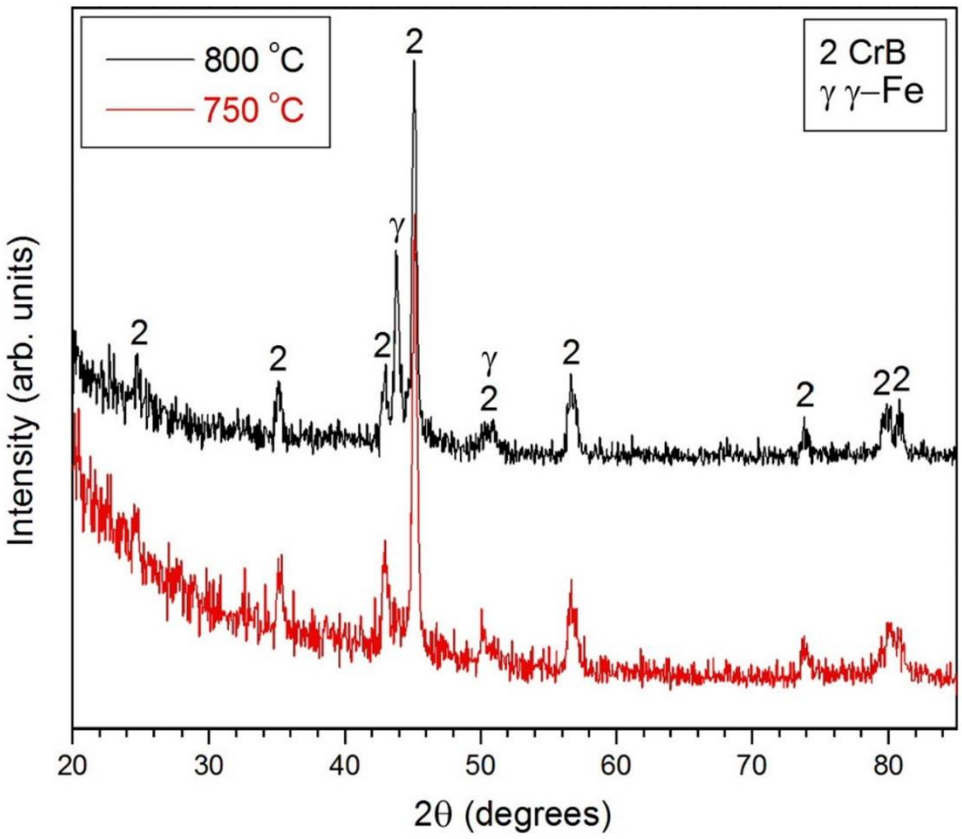

Figure 28: XRD patterns of discs borided at starting temperatures of 750 and 800 °C. Beyond austenite, only Fe_2B is detected.

Indentation testing was performed on borided 316 stainless steel discs with the use of a Rockwell indenter equipped with a tungsten carbide ball of 1/8 in. diameter. After indentation, optical microscopy was first used to detect any broad scale delamination or cracking. However, no discs showed any visible failure via optical microscopy, so scanning electron microscopy was then employed given its larger depth of field and greater magnification. Additionally, the backscattered electron imaging mode is useful for detecting crack propagation around and in the indentation that would otherwise be more difficult to identify. Loads of 60 and 100 kg were first applied a set of test boride

coated discs. When no cracking or spallation was observed at these minimal loads, a maximum load of 150 kg was then applied to the center of each boride disc in this study.

Shown in Figure 29 is a set of SEM images of the 150 kg load used to indent a disc that was borided with a starting temperature of 550 °C. Figure 29 (a) is in the normally used secondary electron mode for imaging topography with an accelerating voltage of 15 keV. This image shows the remaining crater after indentation with a diameter of 1.1 mm. No spallation is observed in or around the crater while faint cracking can be seen near the interior edge of the crater. The cracking is enhanced in Figure 29 (b) which is the same area in backscattered electron imaging mode. As expected, the resultant creacking is more evident using backscattered electrons. Circumferential cracking is mainly present in the interior of the crater, but minimal cracking is also seen slightly outside the crater's edge. A higher magnification image of the bottom right portion of the edge of the crater is shown in Figure 29 (c). This higher magnification secondary electron micrograph of the indentation's edge shows the circumferential cracking present at the edge and mainly in the interior (shown as lighter gray) of the indentation. Even at this magnification, no additional cracking or delamination is observed of the borided surface. Based on the Rockwell C adhesion scale, this would be classified as HF1 since coating failure associated with radial cracking and coating delamination outside of the indent. In this case, cracking is almost exclusively limited to the interior of the indentation and is circumferential in nature. This is evidence of good adhesion for low temperature boriding which is likely aided by the limited diffusion depth of the borided surface since the same deposition time is employed for all coatings.

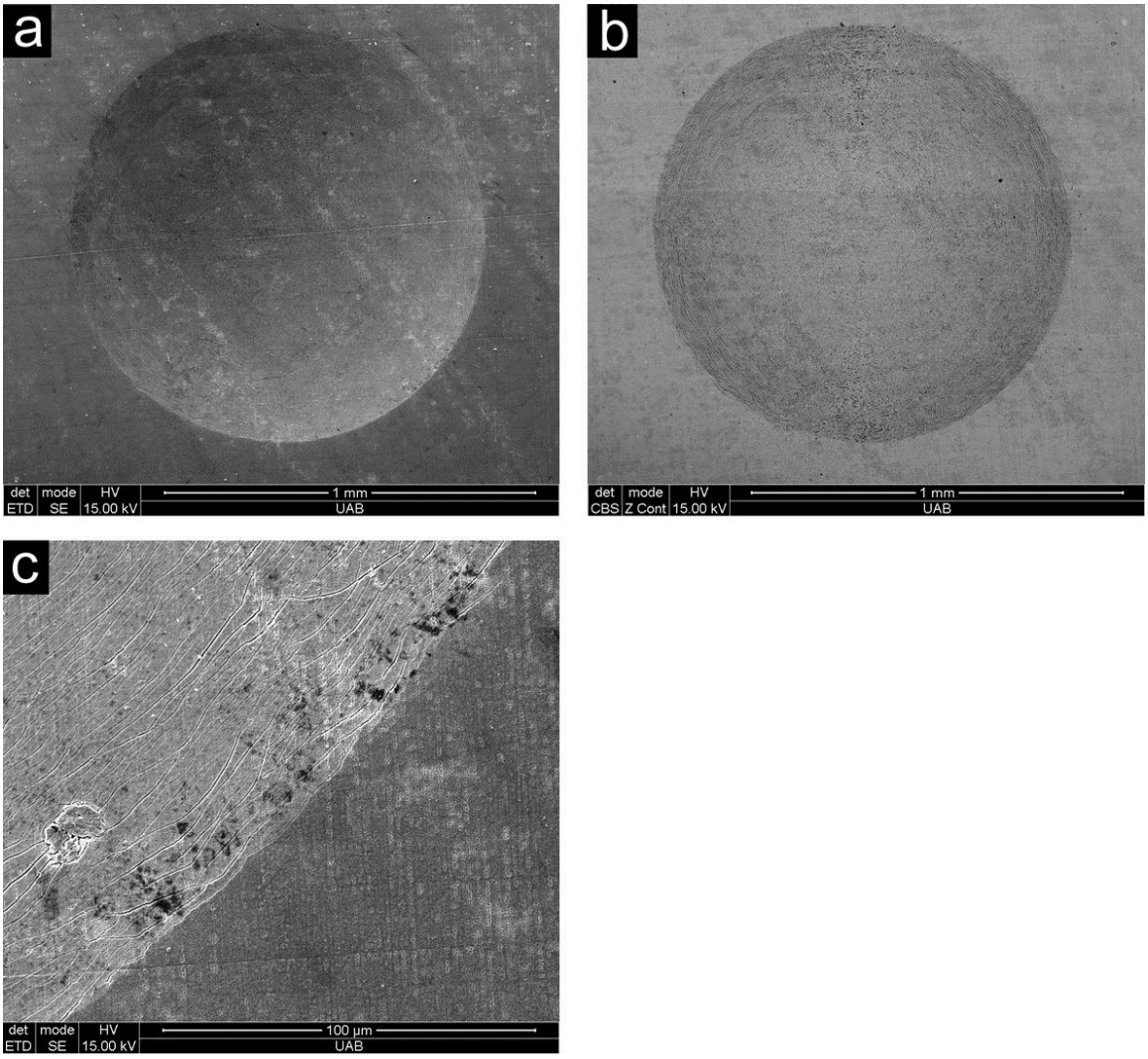

Figure 29: Secondary and backscattered electron SEM images of a 150kg load indentation on a 316 disc borided at 550 °C.

Next, a disc borided at a starting temperature of 600 °C for 30 min was indented at the same standard load of 150 kg. Figure 30 (a) shows an overview scanning electron micrograph of the 1.1 mm diameter indentation. While the indentation is hard to see because of the backscattered electron mode, it serves to enhance any visible cracking on the surface. However, no cracking is seen at this low magnification. This is in contrast to the indentation on the previous disc borided at 550 °C where circumferential cracking was evident within the interior of the indent. As before, a close-up of the edge of indent

corresponding to the bottom-right of the previous image is presented in Figure 30 (b). Cracking that is hard to see in the secondary electron version of this image is clearly visible in this backscattered electron mode. Particles resulting from growth of borides on the surface partially obscure the cracking. In comparison to the lower temperature borided disc, while circumferential cracking is still present, it is less evident and not as prevalent. This disc would also be classified as HF1 given the lesser extent of cracking compared to the last disc and lack of delamination or radial cracking.

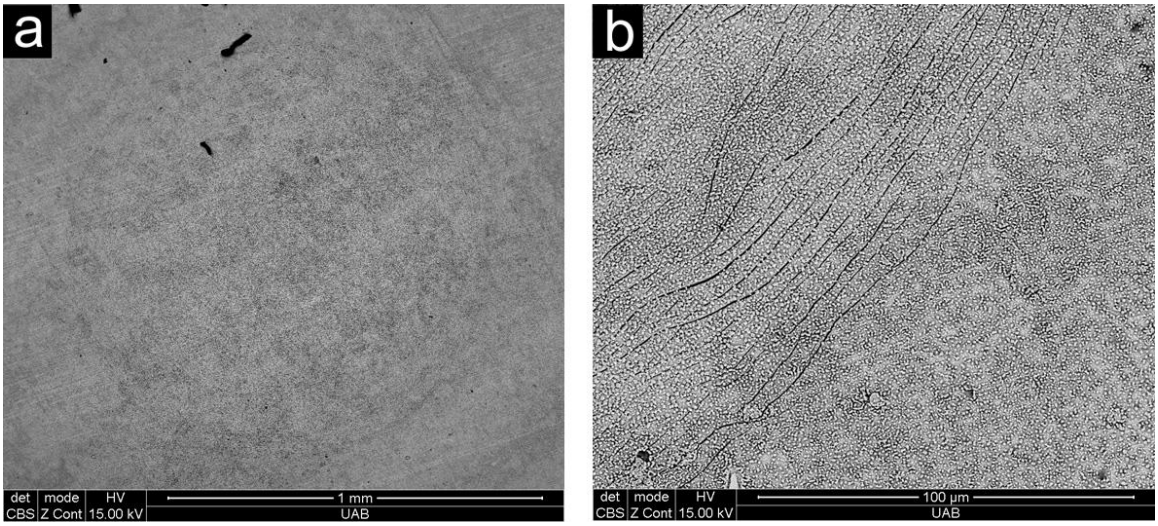

Figure 30: Backscattered electron micrographs of a 150kg load indentation on a 316 disc borided at 600 °C.

A third disc was borided at a starting temperature of 650 °C and SEM images of the 150 kg indentation are shown in Figure 31, (a) and (b). This disc appears to have some contamination shown in black that may have been present on the indenter which was then transferred to the borided disc after indentation and unloading as seen in the secondary electron image of Figure 31 (a). No cracking can be observed. However, the light and dark areas of the disc's surface suggest incomplete coverage of the disc and a non-uniform boride coating. Figure 31 (b), a magnified backscattered electron view of the

indentation edge, shows the presence of fine circumferential cracks in the interior of the indent similar to the previous two discs. The quantity of cracking appears greater than the previous two discs, but this is a result of a lower magnification image. Nucleation of smaller grains compared to the previous disc borided at 600 °C are observed. The quantity of these surface features is also greater, and some regions have extremely heavy nucleation which appeared as the lighter areas in the overview image that seemed to imply incomplete coverage of the boride interlayer. The grains also appear elongated versus the more rounded grains of the lower temperature boriding. While providing yet another HF1 adhesion rating, the incomplete coverage likely an unideal diffusion barrier.

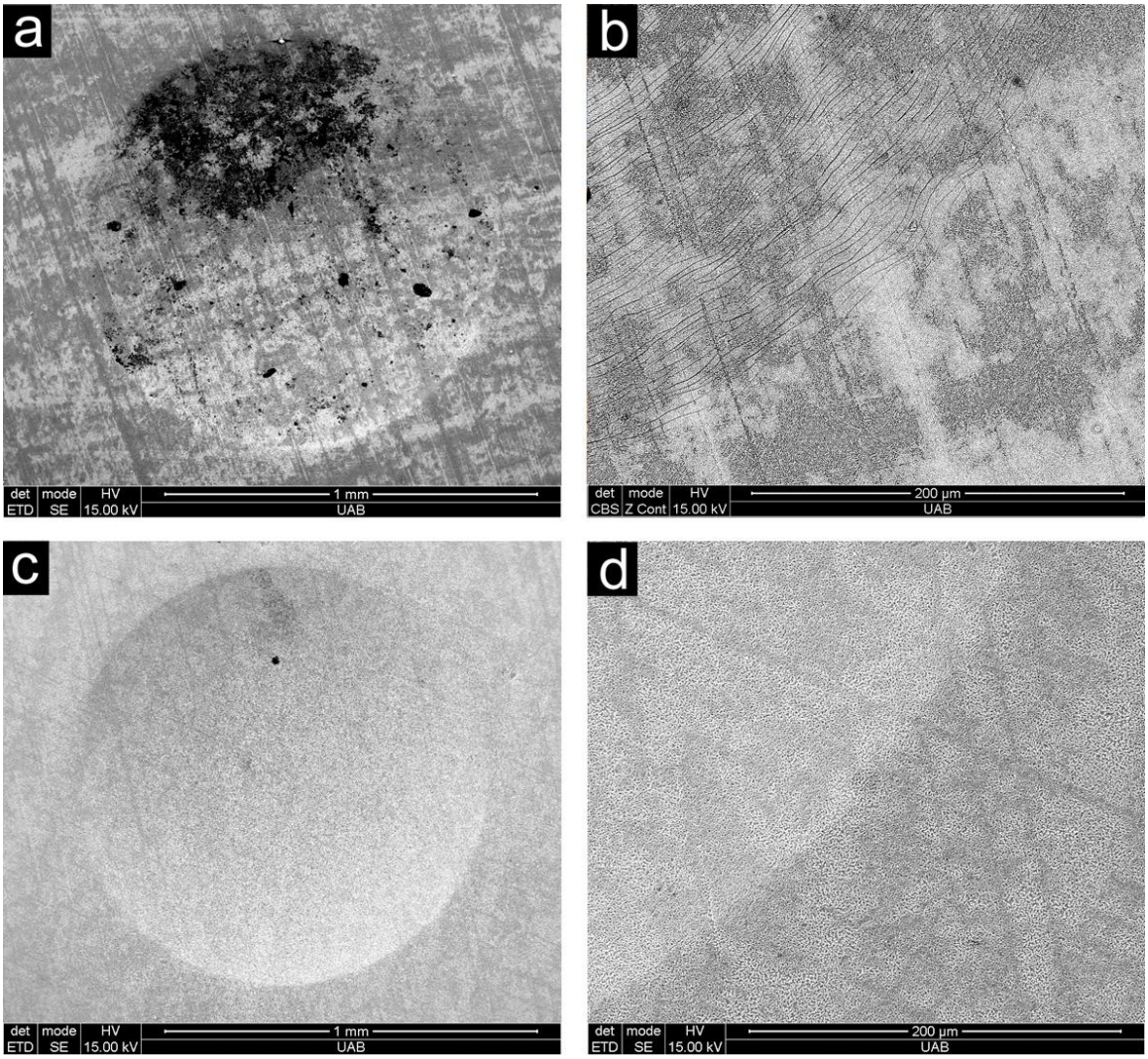

Figure 31: SEM images of 150 kg indentations on discs borided at 650 °C (a) + (b) and 700 °C (c) + (d).

Figure 31 (c) and (d) show secondary electron micrographs for the overview of the remaining plastic deformation on a disc with a starting boriding temperature of 700 °C. No cracking or spallation of the boride coating is detected in the overview of Figure 31 (c). Parallel lines running from the upper-left to the bottom-right as well as lines running almost vertically are the result of the finishing 1200 grit sanding step. A secondary electron image in Figure 31 (d) has the indentation corresponding to the upper-left region shown as lighter in shade. After probing much of the edge and interior of the

remaining indent, this micrograph was one of only a few regions showing only minimal cracking near the edge of the indentation. Given the lack of any large scale cracking compared to the preceding three discs, this shows the best adhesion yet and achieves an HF1 classification.

750 °C was the next increment for boriding of 316 stainless steel. Figure 32 (a) and (b) show the scanning electron micrographs of various magnifications for this indentation. In Figure 32 (a), the overview of the remaining indent is imaged and found to have a diameter of 1.1 mm after unloading. As before, no delamination or cracking is observable at his magnification as has been the case for the last few boriding temperatures. Figure 32 (b) shows the secondary electron image of a 150x150 μm^2 enlarged area of the edge of the indent. At this magnification, no cracking can be detected throughout the indent for the 316 stainless steel disc borided at 750 °C. Many regions of the indent were probed, but even cracking was no longer existent. The uniformity, complete surface coverage, and the HF1 adhesion rating make this a capable candidate for subsequent diamond deposition.

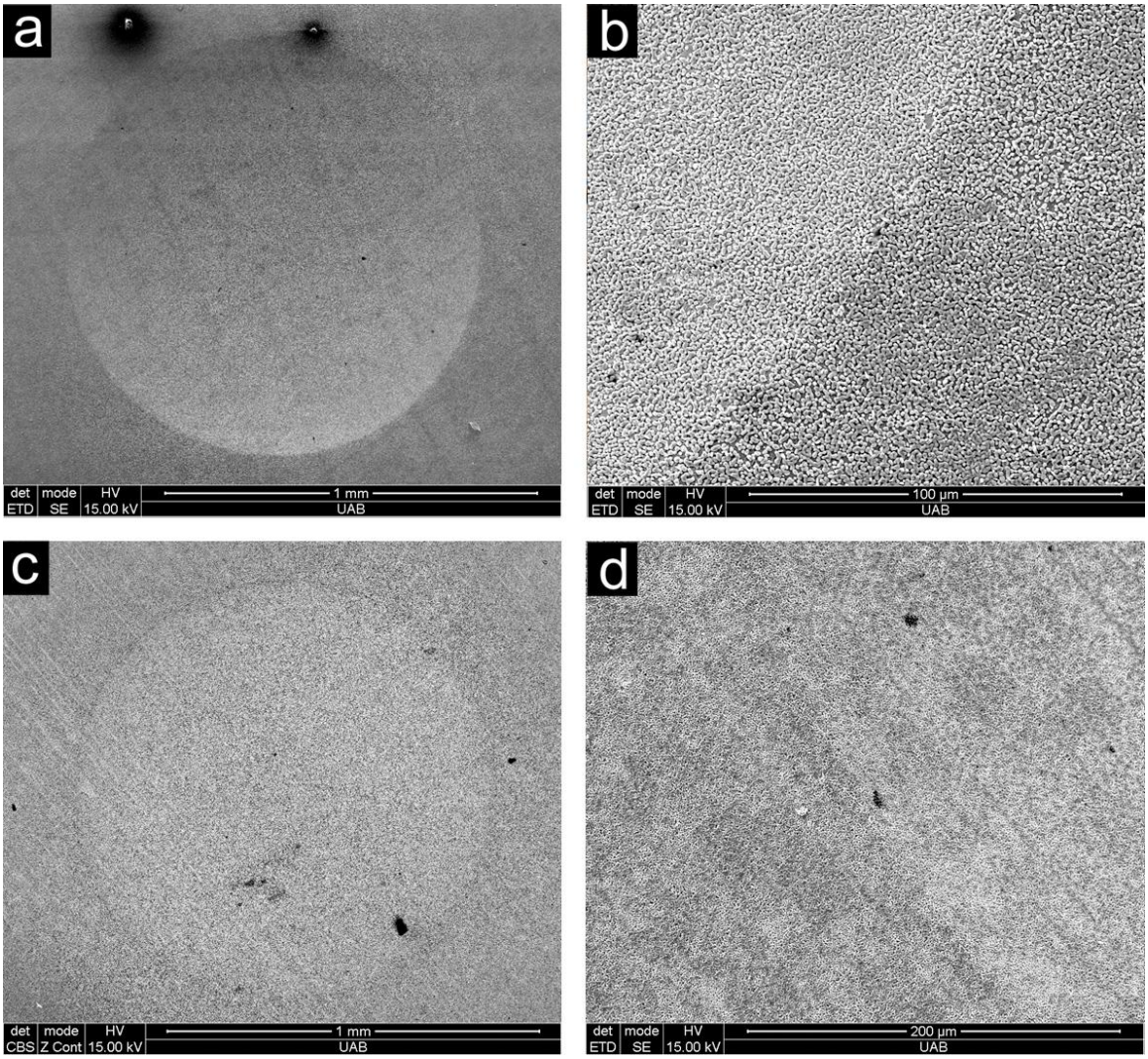

Figure 32: SEM images of 150 kg indentations on discs borided at 670 °C (a) + (b) and 800 °C (c) + (d). Excellent surface coverage by the nucleated borides and no cracking is detected for either disc.

Finally, a disc was borided at the highest starting temperature of 800 °C. A 1.5x1.5 mm^2 backscattered electron SEM image of the entire indentation is displayed in Figure 32 (c). The backscattered mode makes the indentation less visible without the shading, resulting from topography, from the secondary electron mode. Parallel lines running from the top-left to the bottom-right once again are the result of the final sanding step. No failure modes can be seen at this magnification. Thus, a higher magnification is

presented in Figure 32 (d). This secondary electron micrograph of a 200x200 μm^2 area of the indentation edge reveals no cracking of any nature. This is in good agreement with the previous disc that was borided at a 50 °C lower temperature but produced a similar coating appearance. Yet again, an HF1 adhesion rating is achieved, but the lack of any visible cracking even within the interior of the indent confirms this to be one the best adhered coatings obtained in this study.

Adhesion testing via Rockwell indentation was used to compare various adhesion levels of boride coatings. Failure modes present as cracking (circumferential and radial) and delamination. All boride temperatures produced good results with only circumferential cracking observed. No radial cracking or catastrophic spallation of the coating was detected for any borided disc. The general trend observed is that increasing the temperature of the boriding step results in reduced cracking. The lowest temperature boride coatings presented stable circumferential cracking at the edge and interior of the indentation. After increasing average boriding temperature to 750 °C, no cracking can be detected at the edge or within the indentation interior. Based on the XRD data and progression of the metal boride phases present at each temperature, the cracking appears linked to the presence of CrB. Only at 750 and 800 °C is no CrB present and the interlayer is composed solely of Fe_2B. The lack of any FeB phase produced at any boriding temperature is one likely explanation for the adhesion strength given its higher thermal expansion coefficient combined with brittleness.

Boride interlayers produced at various temperatures and resulting phases were probed by Raman spectroscopy. No literature data exists on Raman modes for these phases and no peaks were observed. Scanning electron microscopy was also used to

study the surface of as-borided 316 discs. Shown in Figure 33 are a set of micrographs at various magnifications for a disc borided at 750 °C.

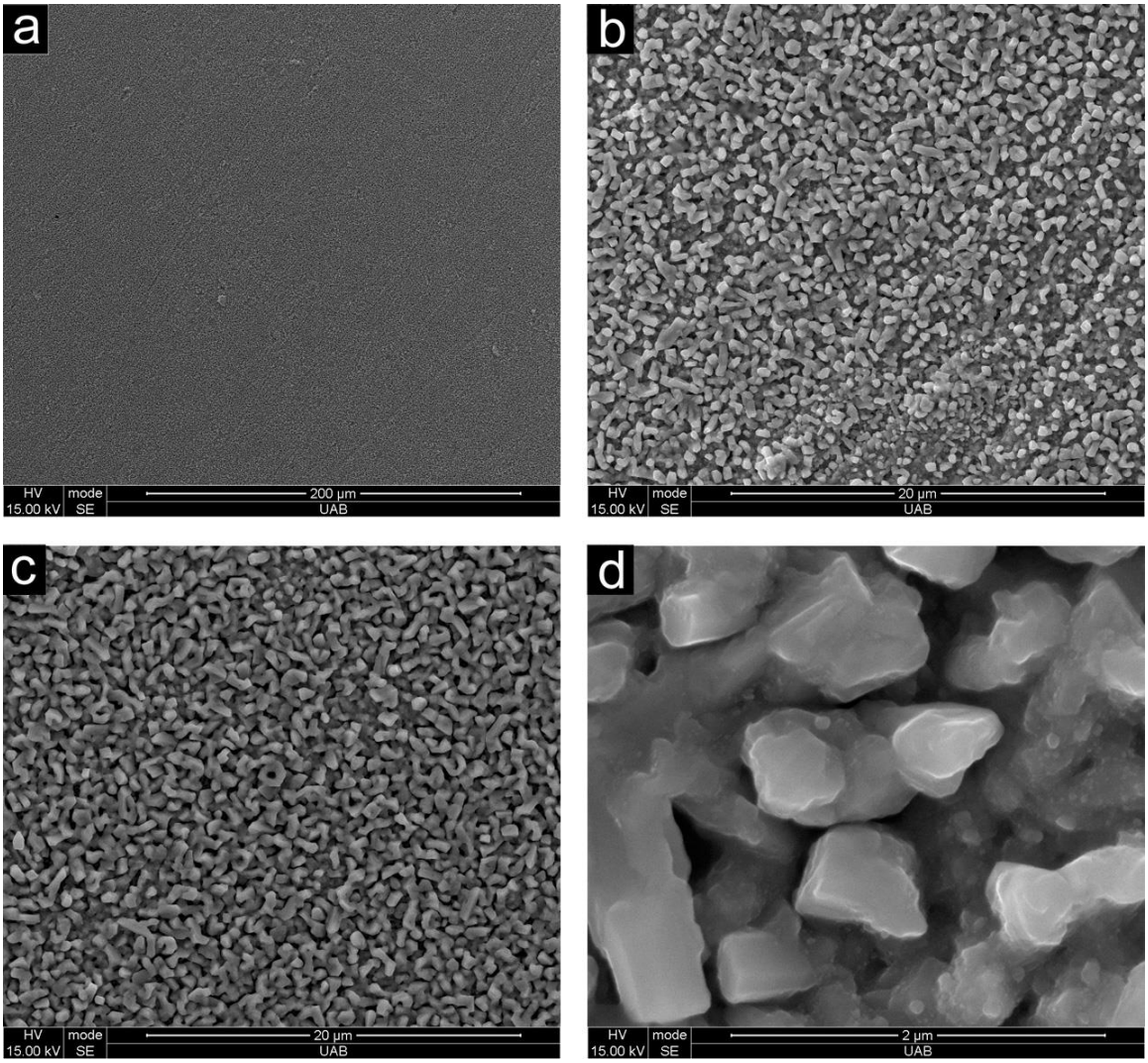

Figure 33: SEM images of various magnifications of a 316 stainless steel disc borided at 750 °C.

The lowest magnification image, Figure 33 (a), shows uniform coverage of the disc. Increasing to higher magnifications, Figure 33 (b) shows the presence of rod-like grains, making up a very uniform, albeit rough, morphology over the entire surface. The uniformity of the coating is confirmed by imaging various regions across the surface. Figure 33 (b) was taken toward the center of the disc and (c) corresponds to a region near

the edge. Finally, a higher magnification image in Figure 33 (d) shows a close-up of these grains which shows evidence of smaller particles that may be the initiation of secondary nucleation of further boride structures. The rough surface is reminiscent of a coral structure and is potentially problematic given the voids that are associated with it which the diamond coating must fill-in to achieve a dense microstructure. Additionally, diamond is expected to deposit conformally via microwave plasma CVD on this surface which could likewise yield a rough diamond film.

In conjunction with SEM, EDS was implemented on a cross-sectioned 316 stainless steel disc that had been borided for 10 minutes at 700 °C. Cross-sectioning was conducted using a diamond saw; the interior surface was then sanded with 400 to 1200 grit sandpaper and polished up to a 1 μm diamond slurry. The resultant scanning electron micrograph of the disc while mounted in polyester resin is shown in Figure 34. The lighter area on the left-hand side is the bulk stainless steel and the dark region on the far right corresponds to the resin. The boride coating is indicated by the red arrow. The coating appears to have a porous nature that is heavily contrasted by the bulk metal. A similar result was observed for pack boriding on 316 steel [51]. A flat transition from the bulk metal to the metal boride is observed which is less desirable than the sawtooth morphology obtained on low alloy steels since a mechanical interlocking effect can aid film adhesion. The reason for this flat interface versus the jagged interface for regular steels is the addition of substantial alloyihng elements including Cr and Ni. These act to form a diffusion barrier to the inward boron diffusion thus resulting in both thinner boride layers and flatter interfaces [39, 76]. An EDS line profile was performed as shown by the orange line of the SEM image. This was done using a low accelerating voltage combined

with quality electron optics allowing for higher spatial resolution on the order of a 100 nm [76]. The elemental composition results as a function of distance are shown in Figure 35 for Fe (a) and B (b). The level of boron diffusion into the steel tapers off significantly but is higher near the surface as expected where iron borides dominate. However, a sharp interface is not observed as desired which prevents a dramatic change in the properties of the material and should reduce the risk of delamination. This is evidenced by the gradual increase in boron concentration when following the line scan from the bulk steel to the borided surface. While a somewhat noisy spectrum is detected for boron, the trend of the data is apparent and aided by a polynomial trend line. Correspondingly, a decrease in the iron concentration is seen as the scan nears the surface. While not shown, other steel elements including chromium, nickel, and molybdenum all display the same trend as expected. Oxygen contamination was detected throughout the sample at fairly consistent levels. Lastly, significant carbon content was detected despite no NSD coating and minimal carbon presence in the steel. This is a result of the sanding stage using SiC sandpaper (as silicon is likewise observed) and the polishing step using NSD slurries.

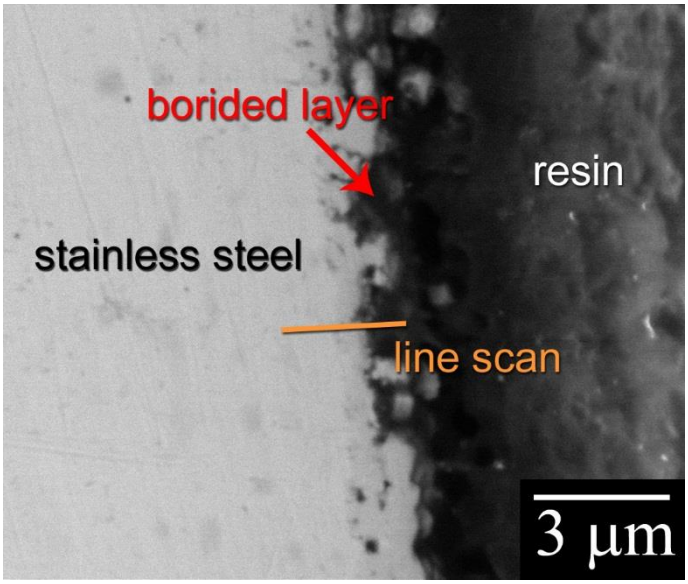

Figure 34: SEM image of cross-sectioned borided 316 stainless steel disc mounted in polyester resin. The bulk metal is on the let shown in white and the resin is seen in black on the right. The boride coating is denoted by the arrow. The line corresponds to the EDS line scan taken for elemental composition.

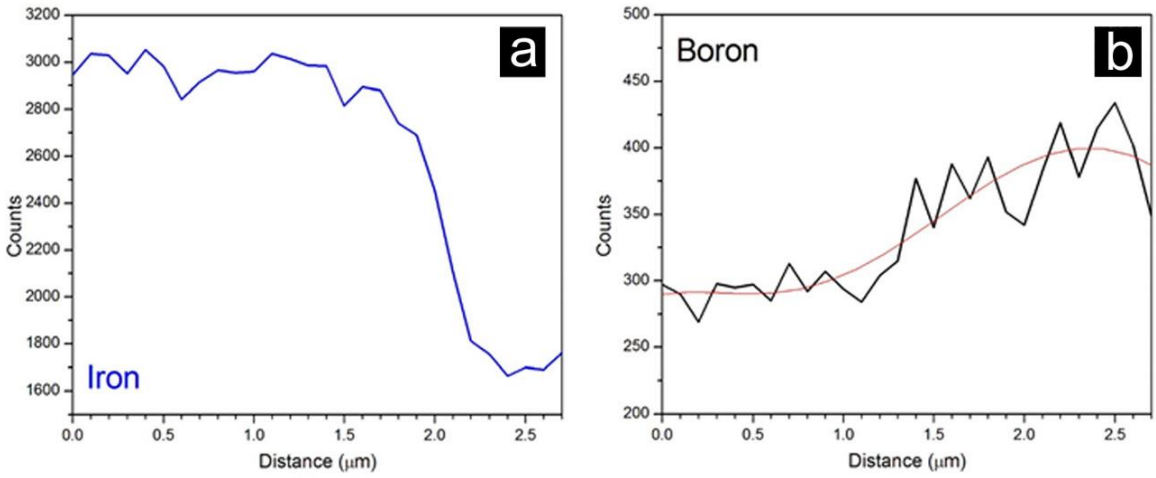

Figure 35: Elemental composition of borided 316 steel disc as a function of depth for Fe (a) and B (b) collected using the line trace from the SEM image in Figure 34.

Various diamond depositions were attempted on 316 discs borided at a range of temperatures. Raman spectra are shown in Figure 36 for one such disk borided for one hour at 57 Torr and 1.50 kW for a resultant temperature of 730 °C. Approximately 750

microns of diamond film were then deposited at 675 °C via 54 Torr, 1.20 kW, and the standard NSD gas chemistry. A scan near the center is shown in black, and a scan toward the edge is shown in red. Excellent agreement is seen from the two scans. A broad peak is observed in the range of 1300-1400 cm^{-1}. This corresponds to the combined diamond peak and D band of graphite. The peak at 1470 cm^{-1} is due to TPA. Finally, a broad peak of the greatest intensity at 1540 cm^{-1} is associated with the graphitic G band. The additional TPA peak at 1190 cm^{-1} is not detected, likely due to the noisy background coupled with a signal count.

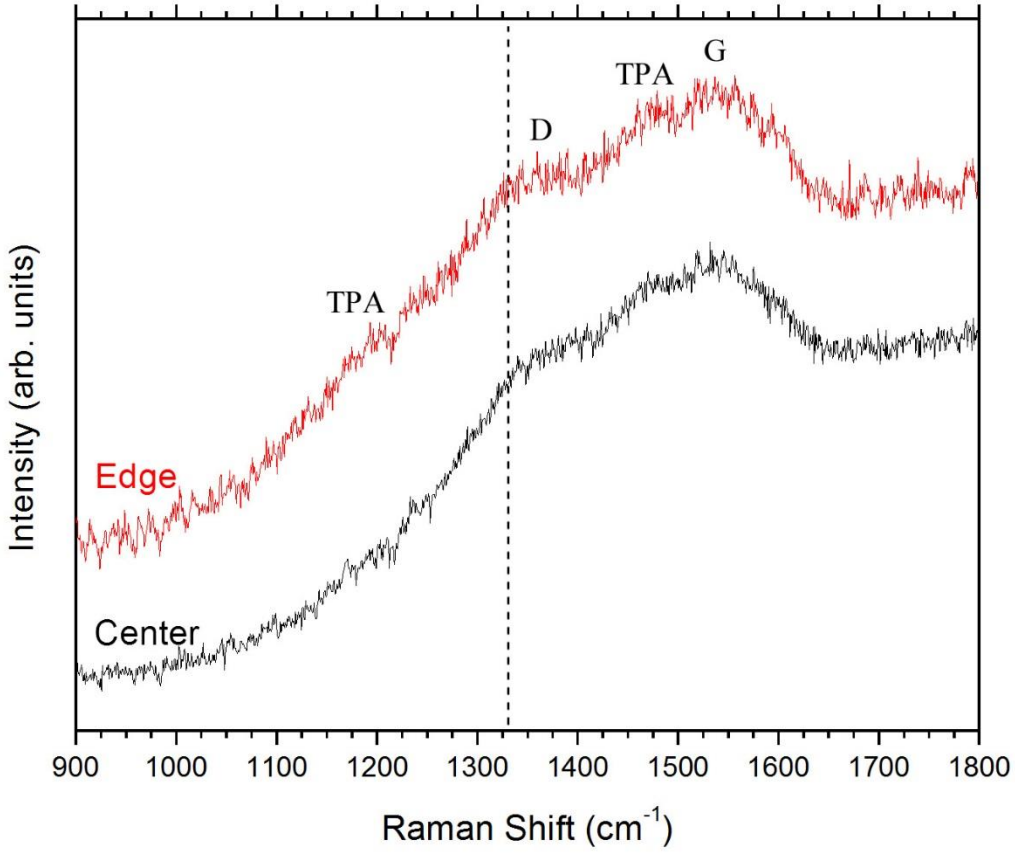

Figure 36: Raman spectra of the edge (red) and center (black) of a diamond film on a borided 316 stainless steel disk displaying well-matched, NSD spectra.

Corresponding scanning electron micrographs are shown in Figure 37 for the previous disc. Figure 37 (a) is a low magnification micrograph showing substantial coverage of the disk by remaining diamond film with only a few areas of delamination or non-coalescence of the film (lighter areas). Figure 37 (b) is an enhanced SEM image showing a magnified view of a region with no diamond film. The surrounding diamond film are grouped into balls relating to the clustering of the small crystallites as seen with the diamond on borided 440C bearings. Cracking of the diamond coating around the region suggests this is in fact where diamond has delaminated due to residual stresses arising from thermal expansion mismatch and cooling from the elevated CVD temperatures. A further magnified view is seen in Figure 37 (c) of this same delamination zone and diamond film interface. The clustering of diamond grains is more clearly seen with an average size of about 2 μm in diameter for the balls. In addition the cracking that was present in the diamond around the delaminated regions, cracking of the coating underneath the diamond is also seen. This is also likely a stress relieving mechanism due to the large residual stresses after cooldown from the thermal expansion coefficient mismatch at both the diamond/boride interface and the boride/steel interface.

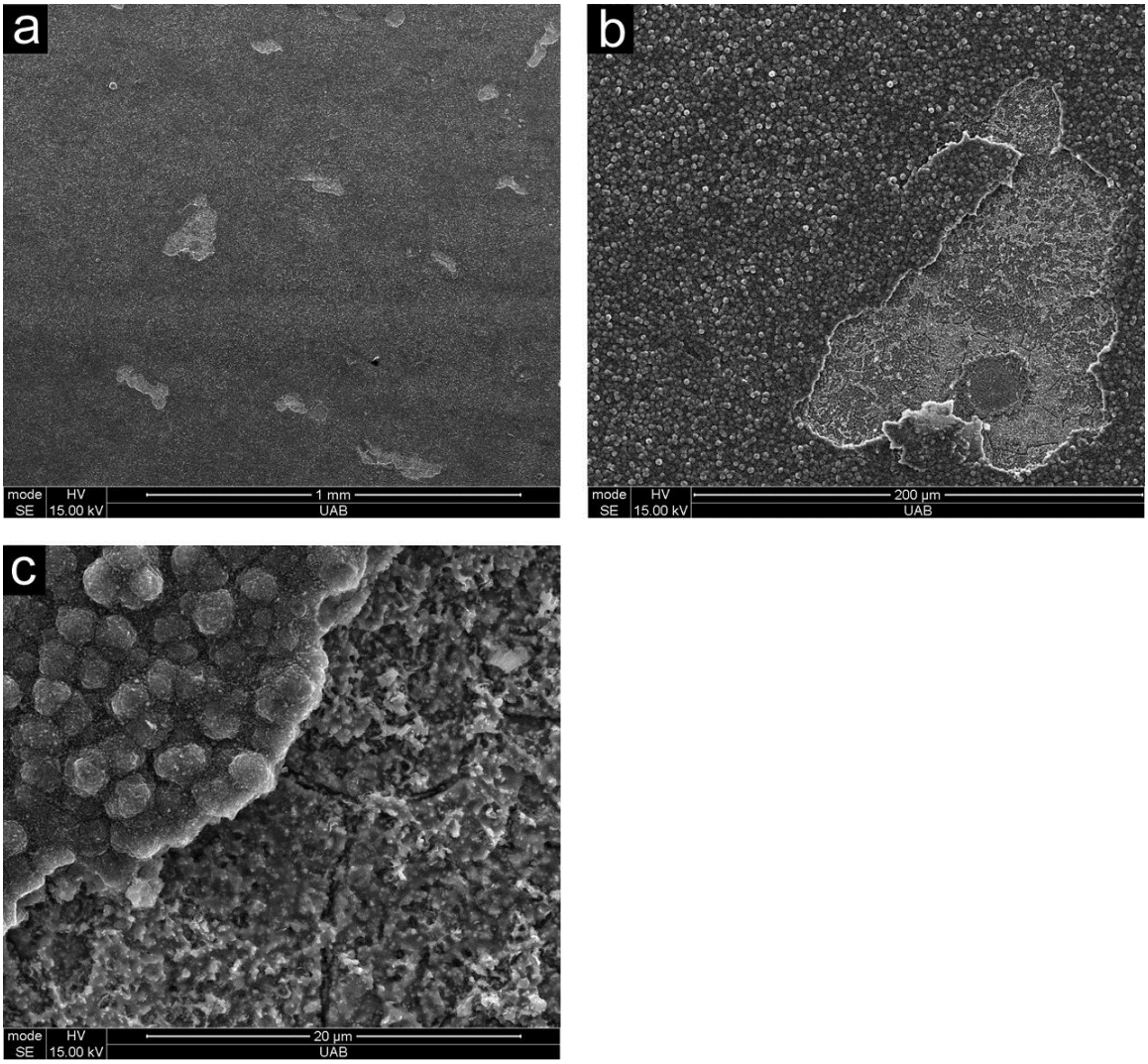

Figure 37: SEM images of a diamond coating showing excellent coverage and enhanced views of a delaminated region.

Another a 316 disk was borided at 55 Torr, 1.15 kW, and 750 °C for one hour using 500 sccm of hydrogen and 2 sccm of diborane. A 700 µm diamond film was then deposited using the standard gas chemistry, 45 Torr, and 1.05 kW for an average temperature of 620 °C. Raman spectra for this disk are displayed in Figure 38. As with the previous disk's Raman spectra, the edge (red) and center (black) share the same peaks. Yet again, the spectra at both locations agree very well and are indicative of a uniform coating across the surface. As before, a broad peak associated with diamond and

the D band is in the range of 1290-1410 cm^{-1}. The G band is also present, but it now possesses a much sharper characteristic. The larger area of this peak is the result of more disordered sp^2 bonded carbon in the film's composition and thus a film of lower quality. This is the result of the lower CVD diamond deposition average temperature which is usually closer to 800 °C. A shoulder on the left of the G band corresponds to one of the TPA peaks, and the additional TPA peak at 1190 cm^{-1} is also detected which was not the case the spectra of the previous disc

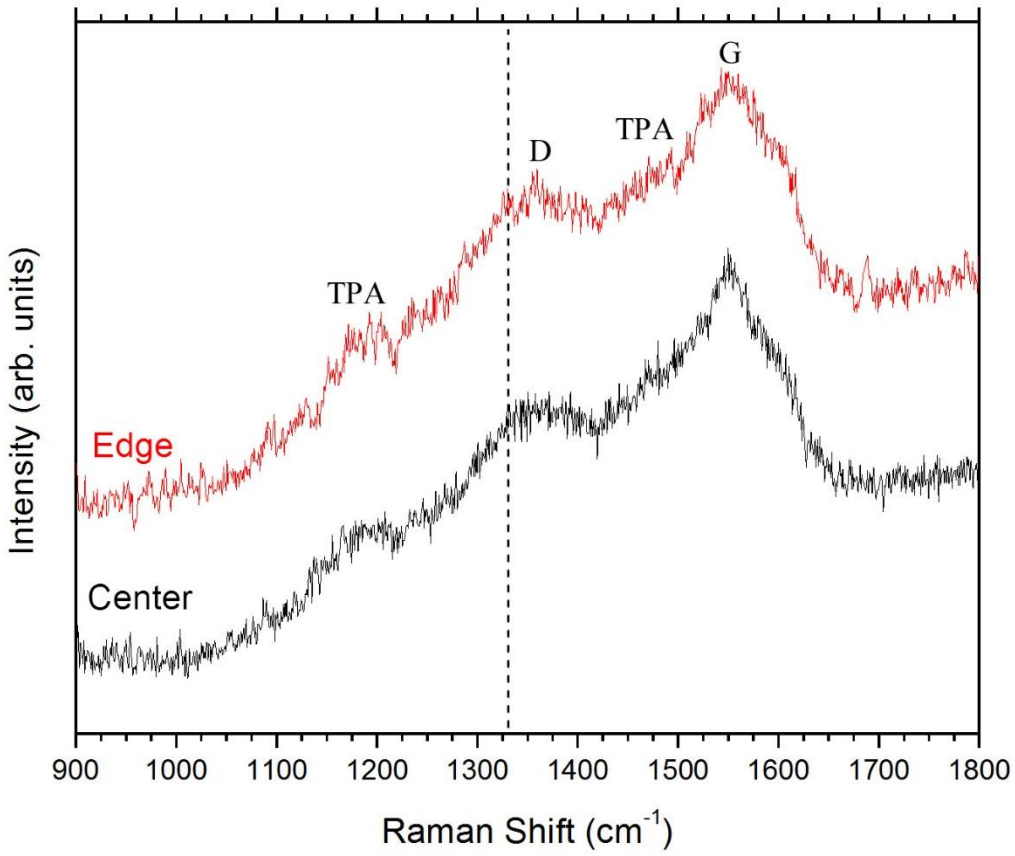

Figure 38: Raman spectra of the edge (red) and center (black) of a diamond film on a borided 316 stainless steel disk. A characteristic NSD signal is observed and the scans advocate for a uniform coating.

Figure 39 shows three secondary electron scanning electron micrographs for the previous disc take at an accelerating voltage of 15 keV. Figure 39 (a) is a broad overview image displaying large area coverage of the diamond film with no regions of delamination. A 30x30 μm^2 magnified view is seen in Figure 39 (b). Similar clustering of the diamond grains in ball-like structures results in a rough surface topography. Charging of the surface is observed with some ball clusters appearing bright due to electric charge buildup resulting from the nonconducting surface which was not sputter coated with a thin layer of gold/palladium. The last image of Figure 39 (c) is the largest magnification to view the individual grains of the diamond clusters. Most of the grains appear to be in the 50 to 20 μm with only a few larger ones with diameters over 100 μm. The roughly spherical particles indicate non-uniform nucleation/growth of the NSD film, and while the resulting rough surface is not ideal for many applications, it is an encouraging step toward the ultimate goal.

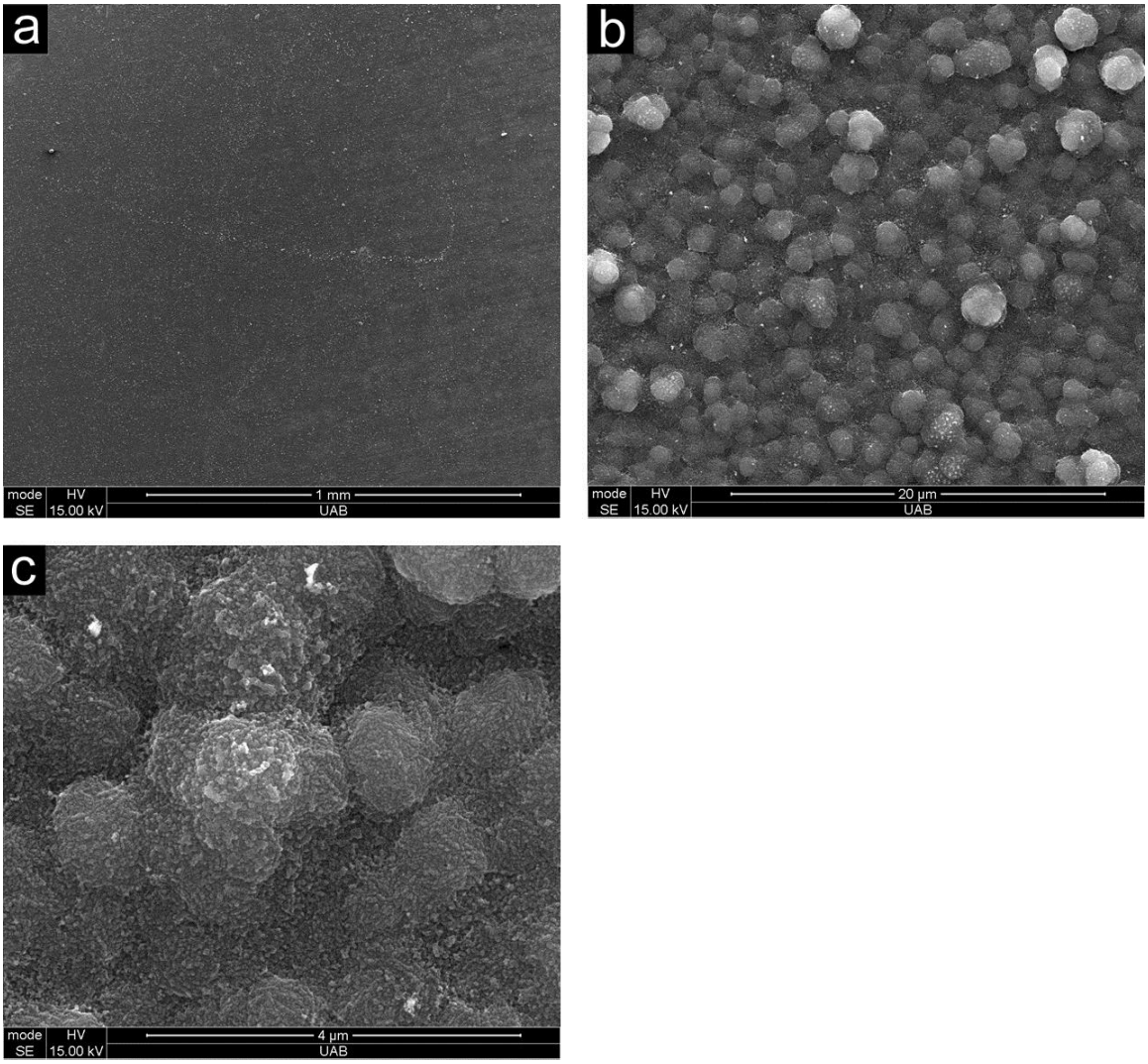

Figure 39: SEM images of a diamond coating with perfect coverage and enhanced views of the "cauliflower morphology."

A third 316 stainless steel sample was borided using 110 Torr, 1.65 kW, 500 sccm H_2, and 2 sccm B_2H_6. The resulting average temperature for the run was 820 °C, and the time of deposition was one hour. Diamond deposition utilized 60 Torr, 2.00 kW, 710 °C, standard nanocrystalline gas chemistry, and a film thickness of about 800 µm. Figure 40 shows two Raman scans at the center (black) and edge (red) of the disk. The most distinguishing characteristic of both scans is the sharp diamond peak at about 1328 cm^{-1} in both spectra. Downshifting from 1332 cm^{-1} is a result of residual stresses in the

diamond film. This would normally be the result of a larger grain diamond film such as microcrystalline diamond. All remaining NSD signatures are seen. The graphitic D band is present to the right of this peak, though its contribution is minimal compared to the diamond signal. The two TPA associated peaks are present with the smaller Raman shifted band seen as a very small, broad hump of the large background signal. Lastly, the G band is present at 1550 cm^{-1} in the edge scan and 1580 cm^{-1} for the central scan. The larger diamond peak combined with the vastly smaller sp^3 bonded carbon scattering cross-section (relative to sp^2 bonded carbon) indicates a substantially higher quality diamond film compared with the previous two discs.

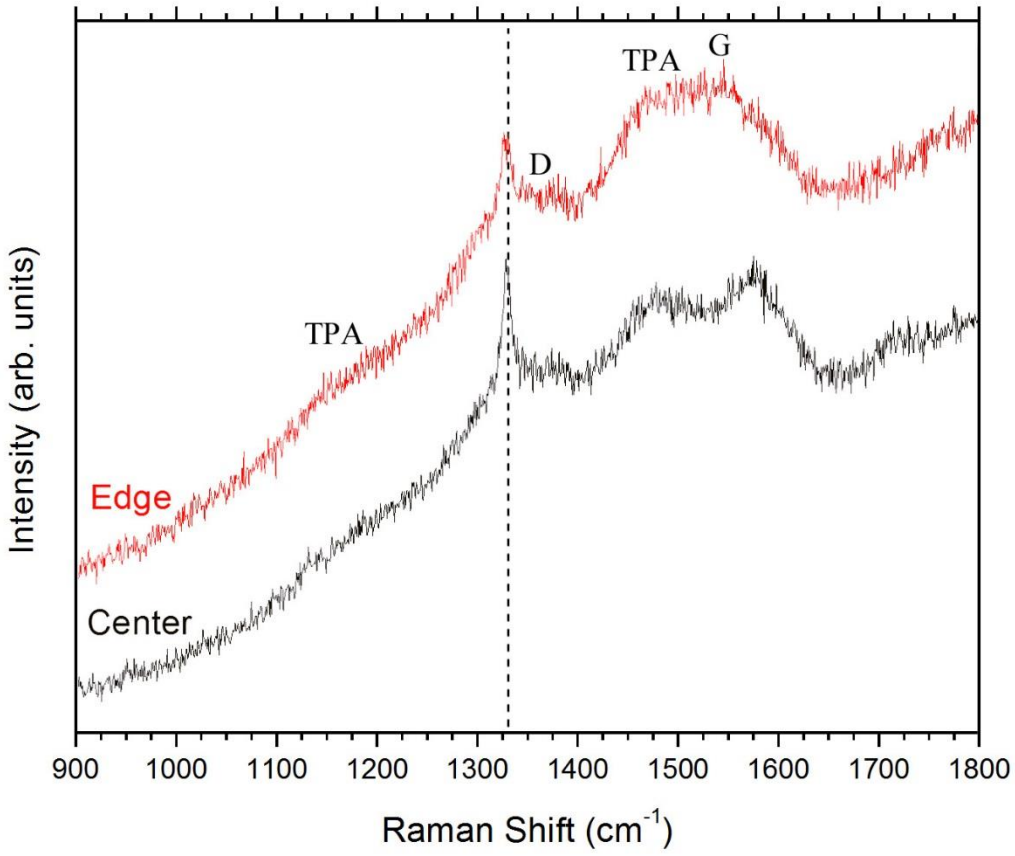

Figure 40: Raman spectra of the edge (red) and center (black) of a diamond film on a borided 316 stainless steel disk. The most prominent feature is the sharp and intense diamond peak.

Figure 41 (a) is a low magnification overview of the previous disc. Poor surface coverage is seen with either substantial delamination or a lack of diamond coalescence. Remaining diamond is seen as the lighter areas of the secondary electron micrograph. Figure 41 (b) is a 30x30 μm^2 micrograph of the interface of one of the uncoated regions. Remaining diamond film is present on the lower left area of the image. The delaminated zone appears cloudy and is rather different in comparison to Figure 37. What remains is likely a result of the underlying boride layer and any chromium carbides that form at the initial stages of diamond nucleation. The diamond film also appears to be of larger crystallite size in agreement with the sharp diamond signal observed in the Raman spectra. Lastly, a different region of the surface showing remaining diamond film is shown in Figure 41 (c). This clearly supports the larger crystallite size observed in the previous image as well-faceted crystallites are evident. The diamond clustering combined with the faceted grains produces an even rougher surface compared to the previous disc. The larger, faceted diamond crystallites are unexpected given the same standard gas chemistry is utilized with only a marginally higher average deposition temperature.

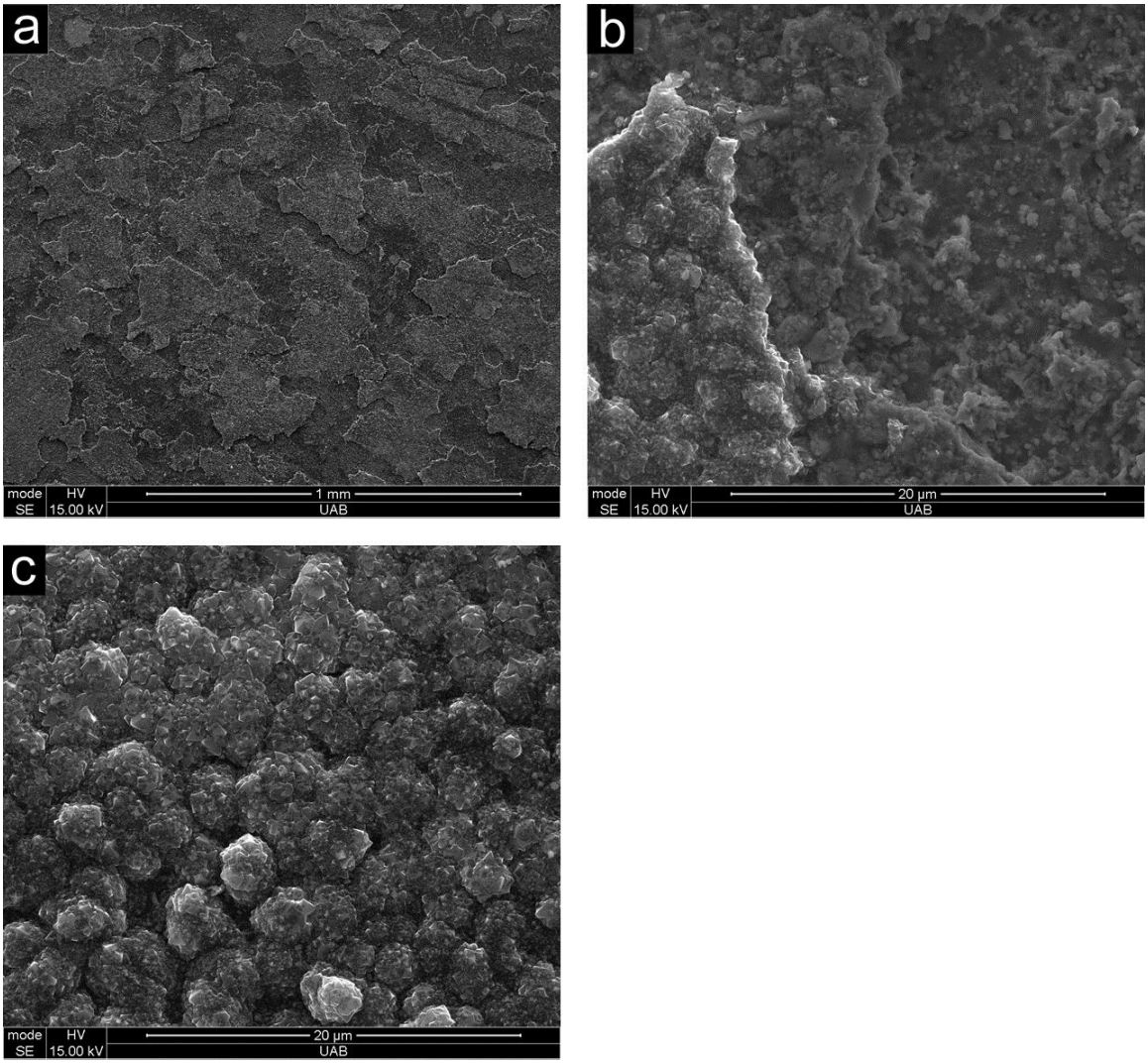

Figure 41: SEM images of a diamond coated borided 316 disc showing poor coverage likely a result of delamination and larger, faceted diamond grains.

Subsequent NSD deposition on 316 stainless steel discs revealed that the Fe_2B phase is the most desirable phase for producing a continuous and adhered film. Figure 42 shows XRD patterns for discs borided at 750 °C (a) prior to and (b) after NSD deposition. NSD deposition was conducted using a modified gas chemistry of 500 sccm of H_2, 50 sccm of CH_4, and 5 sccm N_2. The reduced methane, and corresponding reduction of N_2 to maintain the 10% of methane, were implemented to form a film with an enhanced diamond signal. The Fe_2B peaks still dominate the patterns, and austenite can still be

detected. Several low intensity peaks, mainly in the range of 35-55°, become evident after NSD growth. These are associated with two chromium carbide phases, Cr_3C_2 and Cr_7C_3. This is significant because it is known that metal-carbides can contribute to the graded interfacial structure to yield well-adhered diamond films, such as in the case for titanium [17]. These intermediate carbides likely have some degree of intermixing with the boride interlayer prior to NSD nucleation/growth. The (111) and (220) XRD peaks for crystalline diamond are located at 44° and 75°, respectively. While the (111) reflection overlaps with the dominant Fe_2B peak near 44°, the (220) reflection near 75° is clearly present and supports the existence of crystalline diamond in the film. No peaks could be indexed to graphite (primary peak at 26.5°), the undesirable phase that would otherwise be detected if NSD deposition were attempted on bare steel.

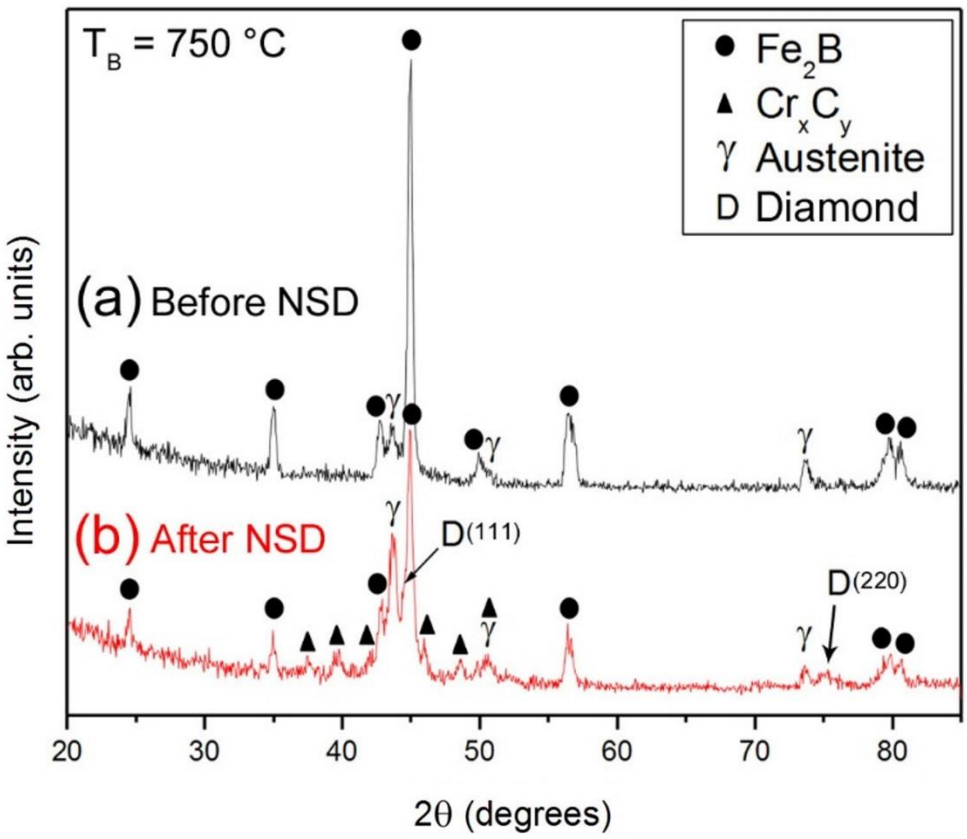

Figure 42: XRD scans of a 316 steel disc after boriding at (a) 750 °C and (b) following subsequent NSD deposition. The additional peaks in (b) correspond to either diamond or chromium carbide phases.

A Raman spectrum of an NSD film produced with the modified gas chemistry is seen in Figure 43. A dashed line at 1332 cm^{-1} corresponds to the location of the peak attributed to stress-free crystalline diamond. A fairly sharp crystalline diamond peak is present in this scan with only minor downshifting. The broad bands c.a.1350 cm^{-1} and 1580 cm^{-1} are typically denoted as being the "D" and "G" bands which are attributable to disordered carbon having both sp^3 and sp^2 hybridization. Again, crystalline graphite was not detected by XRD. The broad bands c.a. 1140 cm^{-1} and 1480 cm^{-1} are associated with trans-polyacetylene. Additional spectra taken at various locations across the surface match well to this one indicating a uniform NSD coating.

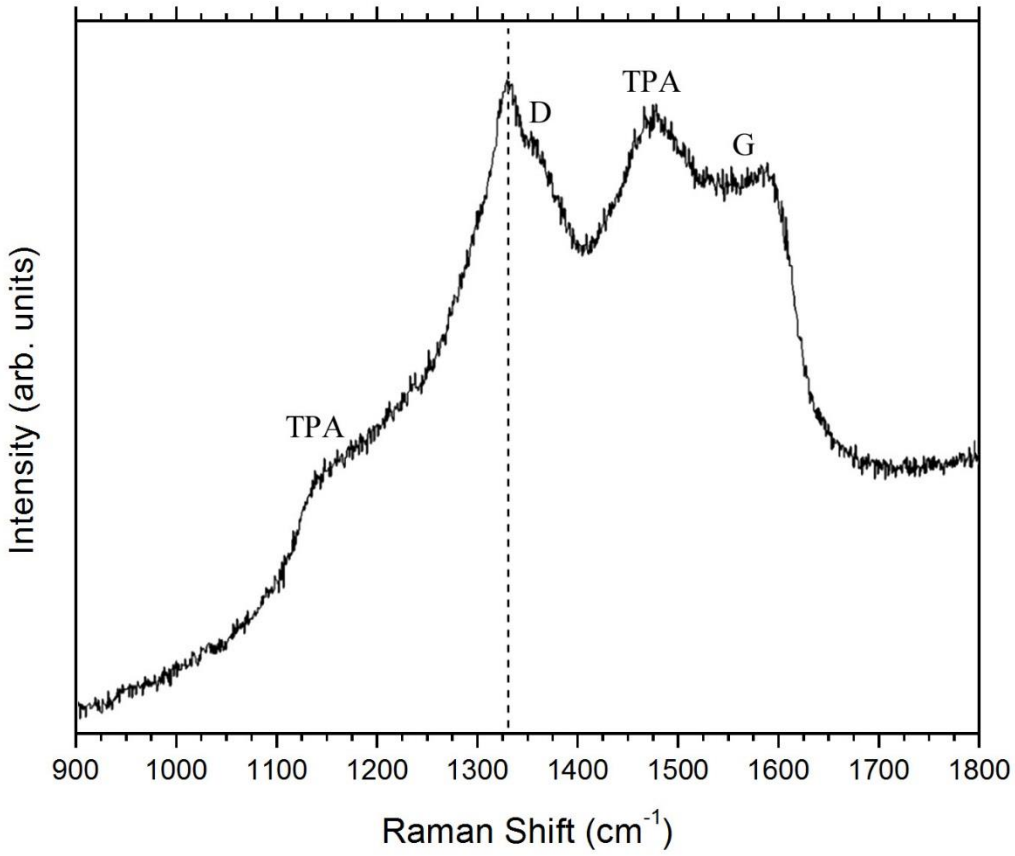

Figure 43: Raman spectrum of a 316 steel disc borided at 700 °C and after subsequent NSD deposition using modified gas chemistry with reduced CH_4 and N_2 flowrates. (a) Raman spectra taken at center and edge locations of the NSD coating. The dashed line corresponds to the position (1332 cm^{-1}) of stress-free crystalline diamond.

Atomic Force Microscopy (AFM) was utilized to probe the surface morphology and roughness after boriding and NSD deposition. Figure 44 (a) shows the AFM image of a borided disc while Figure 44 (b) displays that of a NSD coating. AFM of the surface after boriding confirms observations from SEM indicating rod-shaped faceted particles. Most of these features are on the order of one micron in length. In comparison, the grain size for the NSD film is well below 100 nm. As was determined by SEM, clustering of these grains into a "cauliflower-like" morphology results in a rough surface despite the nanocrystalline nature of the film. An additional image of the borided surface is seen in

Figure 45. This is a 5x5 μm^2 region once more displaying the coral-like structure of the borided surface. A height of approximately 0.88 μm is measured, though the depth of the voided regions may not have been accurately measured. An accurate surface roughness value is also impossible to obtain given the surface morphology.

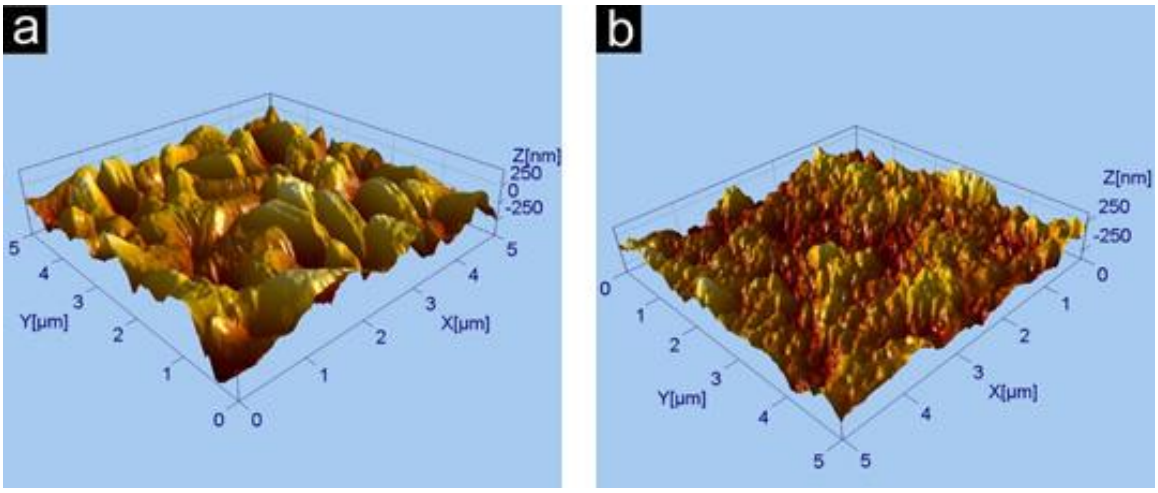

Figure 44: 25 μm^2 AFM 3D images for a borided 316 stainless steel disc (a) and a NSD coating on borided stainless steel (b).

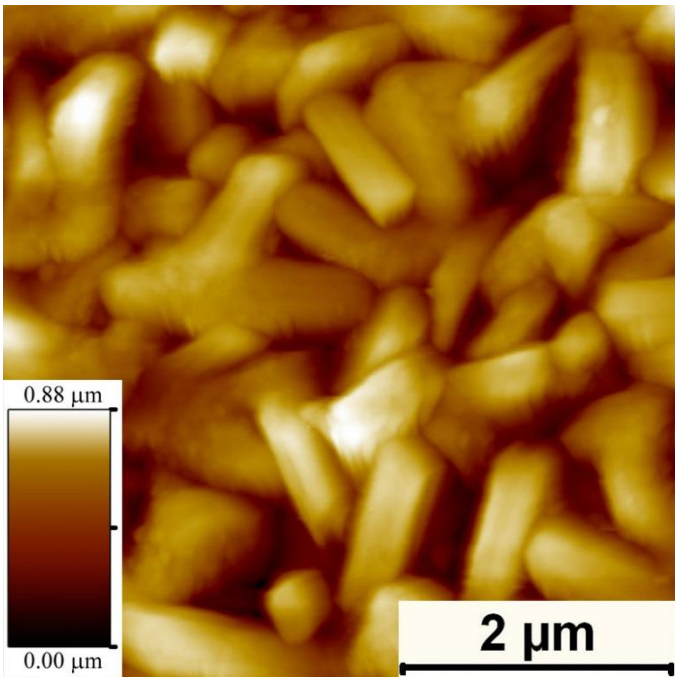

Figure 45: 25 μm^2 atomic force micrograph of a borided 316 stainless steel disc showing a rough, coral grain surface morphology.

X-ray photoelectron spectroscopy has been utilized to probe chemical states on the surface of both borided and NSD coatings. High resolution spectra for B 1s are shown in Figure 46 (a) and (b) of a disc borided at 700 °C both before and after Ar-ion etching respectively. Two chemical states for boron are present as BN or Fe_2B (in addition to a small amount of oxide before etching). After Ar ion-etching, the dominant peak is reversed from BN to Fe_2B consistent with nitrogen being associated with surface contamination. A high resolution scan of Cr 2p after etching is displayed in Figure 46 (c). Chromium is deconvoluted into two states associated with either elemental or oxide forms. The presence of chromium suggests that it could be defusing to the surface. However, given the chromium can form carbides, this could be beneficial if the surface is already carburized during the initial diamond nucleation stage. Chromium is not a transitional metal like iron so its presence is not necessarily a detriment, but the fact it is

present means elemental iron could be as well. The high resolution spectrum for Fe 2p after etching seen in Figure 46 (d) shows two primary states indicative of borides or oxides of iron. The boride is clearly the dominant phase and a stoichiometry of Fe_2B agrees with results from XRD. Likewise, the atomic concentration obtained shows the boron concentration as approximately half that of iron. Since Fe_2B was also dominant for the B 1s scan, this suggests that it is a boride bonding state. However, some elemental iron could still be present given the overlap of iron and Fe_2B states. A comparison of the survey scans (not shown) before and after etching show immense reduction of C, N, and O confirming that these elements are likely present only due to surface contamination. Finally, both the survey scan and high-resolution spectrum for Ni 2p showed a negligible contribution of nickel. This is slightly surprising given the substantial amount of nickel added to 316 stainless steel to stabilize the austenite phase. This is desired though since nickel, like iron, is a transition metal that can have a catalytic effect on the formation of sp^2 bonded carbon. This has been reported before with chromium preferentially substituting in the Fe_2B phase while nickel concentrates between this boride layer and the stainless steel matrix with a potentially limited solubility in iron borides [77, 78].

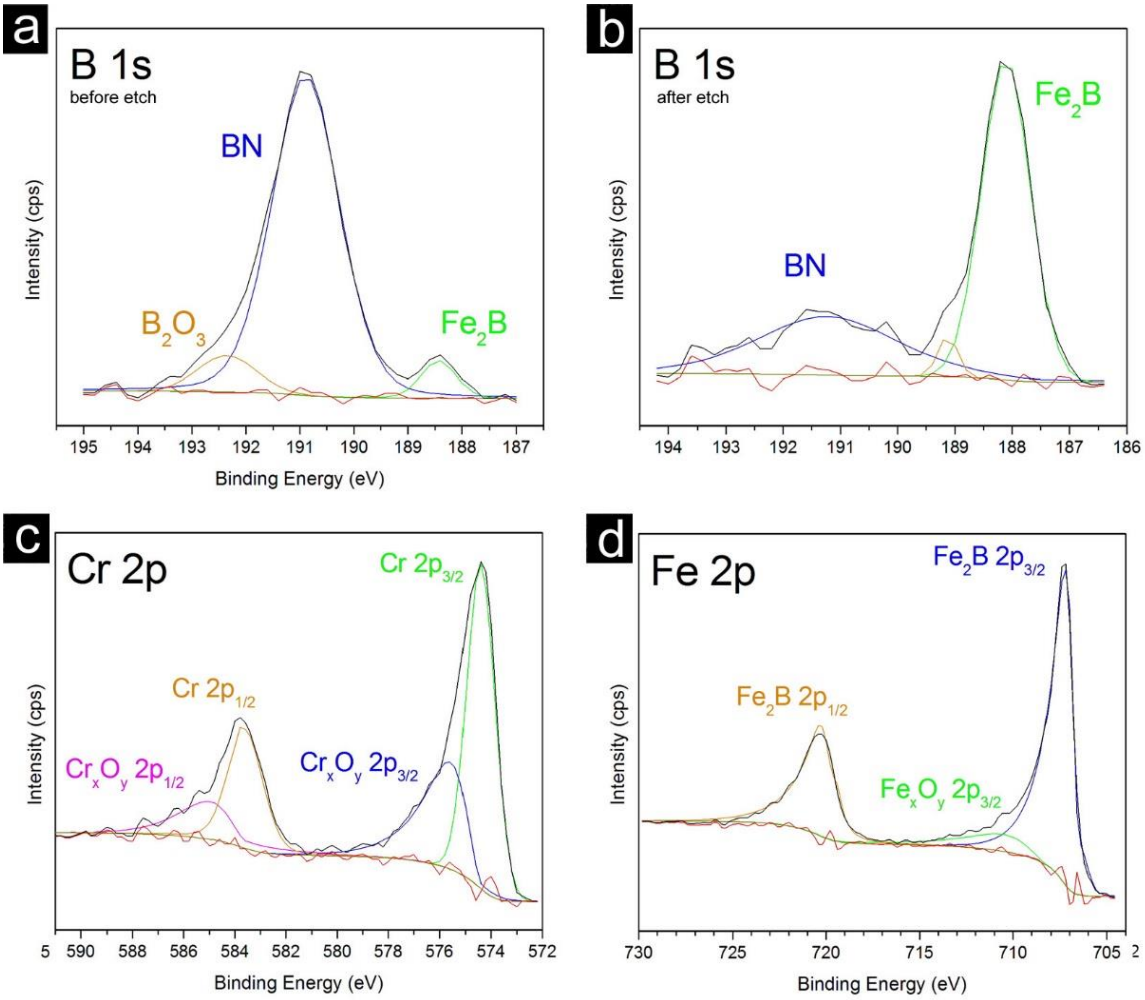

Figure 46: Various XPS spectra of borided 316 stainless steel are provided. High resolution spectra for B 1s are shown (a) before and (b) after sputter cleaning. High resolution spectra for (c) Cr 2p and (d) Fe 2p are also presented after etching.

XPS was also performed on a steel disc borided for 30 mins at 700 °C and deposited with NSD. During the diamond CVD process, optical pyrometer data was used to determine an in situ film thickness of approximately 0.7 μm. The resultant survey scan (not shown) following etching confirmed the dominant presence of carbon, as expected. 10(a) shows the high resolution scan for C 1s which can be used to determine the ratio of sp^2 to sp^3 bonded carbon [79]. The sp^3-bonded component is located at higher binding energies, closer to 286 eV, while the sp^2-bonded component occurs near 284.5 eV as

shown in Figure 47 (a). The peak deconvolution revealed a ratio of 2:3 sp^3-bonded carbon in the film relative to sp^2-bonded carbon. The C 1s peak deconvolution revealed a third peak near 283.5 eV which is related to a Cr_xC_y phase that was also evident from XRD data. The Cr 2p high resolution spectrum is presented in Figure 47 (b). This data is relatively noisy, but fitting shows two states as being either chromium oxide or carbide. From the C 1s peak, the carbide is obviously expected, and the remaining oxygen presence after etching suggests the oxide to be formed during NSD growth. Figure 47 (c) presents the high resolution scan of Fe 2p. The two chemical states are either elemental iron or iron oxide. However, as with the XPS data for the borided sample, fitting of the Fe 2p peak is made difficult by the overlapping peak locations for the boride and elemental states. It is possible that during the NSD nucleation stage, some elemental iron is able to migrate to the surface where the carbon coating is not fully coalesced over the very rough borided surface. The B 1s high resolution data is presented in Figure 47 (d) and shows nitrides and borides of iron. However, given that BN is the dominant bonding state in conjunction with the relative atomic concentration of iron to boron (2:1), the majority of the iron present must be elemental in nature. Subsequent SEM of this sample showed a non-continuous NSD film where many areas had either delaminated or not fully coalesced. Thus, given the spot size used for XPS, data collection was likely from regions containing NSD and/or uncoated boride interlayer. If the film was fully continuous, carbon and minimal nitrogen should be the only elements present after sputter-cleaning. Depending on how much of the surface remained uncoated with NSD, regions of chromium carbide or iron boride would be expected.

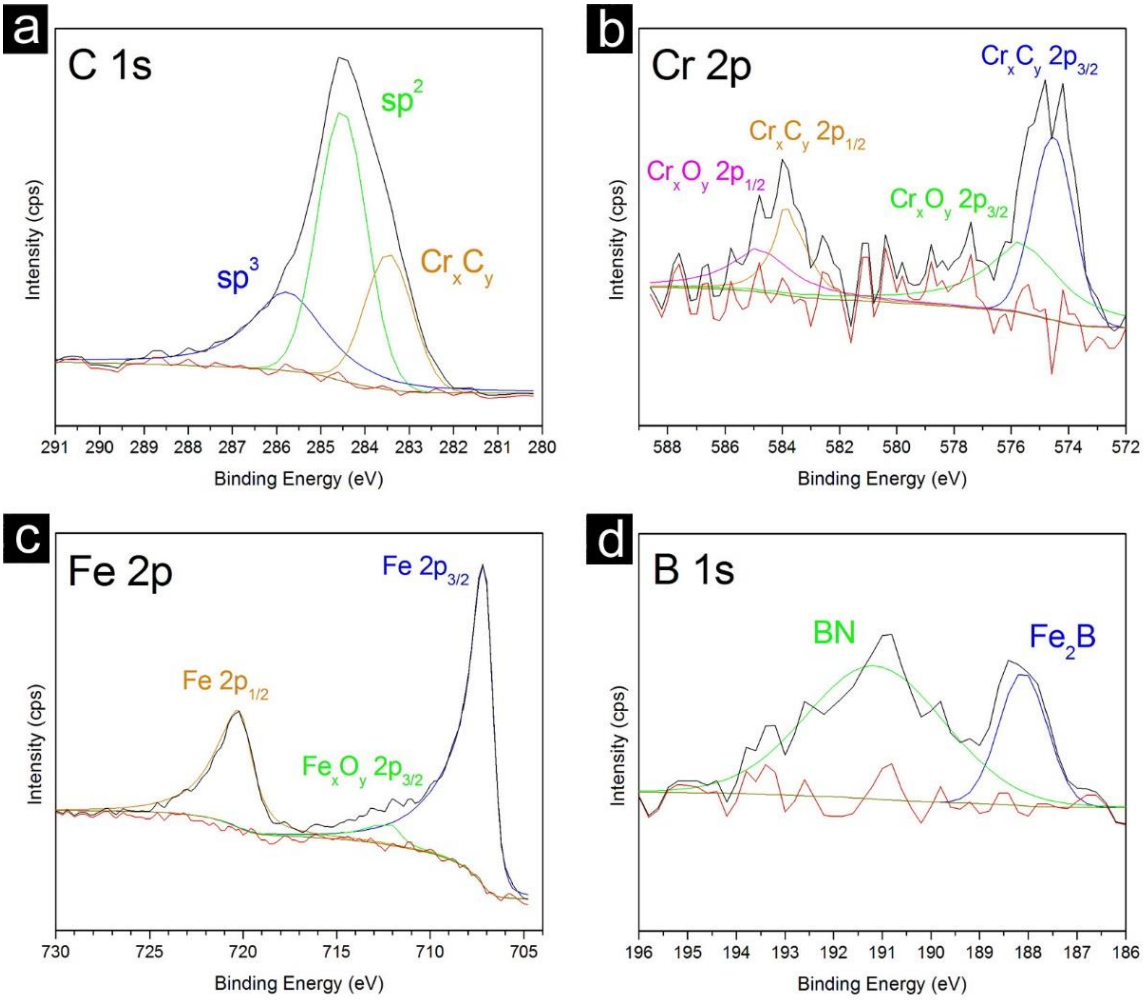

Figure 47: XPS spectra after a NSD deposition with partial delamination on borided steel. High resolution spectra for (a) C 1s, (b) Cr 2p, (c) Fe 2p, and (d) B 1s are all displayed after sputter-cleaning.

316 stainless steel was borided by microwave plasma CVD via thermochemical diffusion of boron into the surface. This resulted in the formation of temperature controlled phases with the reaction pathway being (CrB) → (CrB + Fe_2B) → (Fe_2B) as temperature is increased from 550 °C to 800 °C. Indentation testing showed higher temperature Fe_2B-based borided surfaces to have the best adhesion with no cracking observed after an applied load of 150 kg. Raman spectra of various diamond films on borided 316 stainless steel show characteristic NSD spectra, and XRD following NSD

deposition reveals Cr_xC_y and diamond phases. XPS data confirms an NSD coating containing both sp^2 and sp^3 bonded carbon yet revealed the presence of elemental iron on the surface which can only be explained as being from a region where the NSD coating and underlying boride interlayer both delaminated. Finally, SEM showed the promise of Fe_2B as an effective interlayer with the growth of a fully coalesced and adhered diamond coating exhibiting a rough, diamond-clustering morphology.

4. CONCLUSIONS AND FUTURE WORK

4.1 Conclusions

Microwave plasma chemical vapor deposition is used to deposit nanostructured diamond films on 316 and 440C stainless steels. The advantage of an NSD film is the reduced grain size resulting in low surface roughness through a microstructure consisting of nanocrystalline sp^3 diamond grains embedded within an amorphous carbon matrix consisting of both disordered sp^3 and sp^2 bonded carbon. These films have the potential of excellent adhesion and fracture toughness combined with the possibility of extremely low surface roughness producing a fairly compliant coating that has extreme hardness. Achieving diamond deposition onto stainless steel and other transition metal is difficult due to the catalytic effect on the formation of graphite. This combined with the large mismatch in thermal expansion coefficients (approximately 16 times greater for 316 stainless steel) results in a loosely attached layer of sp^2 bonded carbon and various carbides instead of a continuous and adherent diamond film. An intermediate layer applied between the diamond and stainless steel serves many purposes including the limiting of inward carbon diffusion, blocking outward diffusion of catalytic elemental iron, and offsetting thermal stress with an intermediate thermal expansion coefficient.

Two interlayers have been considered in this research: TiN applied by cathodic arc vacuum deposition and surface boriding grown by the novel method of microwave plasma CVD. The latter is expected to be advantageous given the lack of a discrete

interface between the stainless steel and interlayer by forming a diffusion-based graded microstructure. Interlayers were tested on two substrates including 440C martensitic and 316 austenitic stainless steel grades.

TiN interlayers applied to 440C martensitic stainless steel bearings were studied as a coating to block the mutual diffusion of carbon and iron allowing for growth of adhered NSD films. A range of deposition temperatures were tested as well as various gas chemistries to optimize parameters for growth. Lower temperature diamond depositions resulted in less coating delamination and thus greater remaining coverage following cooldown. The adhesion strength is hindered by the lack of a carbide phase formed during the initial nucleation stage because the of the interlayers ability to successfully block inward diffusion of carbon. This is a confirmation that limited carbon diffusion into the interlayer is desirable to allow for this carbide formation, but the coating must be thick enough to prevent diffusion entirely through the barrier. Beyond the incomplete surface coverage, the main issue is the adhesion strength as any remaining coating is easily removed by wiping. The improved surface coverage on lower temperature runs is likely due to lower residual stress as a result of less cooling needed to reach room temperature after deposition because of coefficient of thermal expansion mismatch. Additionally, the reduction in methane concentration of the feedgas produced higher quality diamond films as expected, but adhesion was still poor with the lack of any interfacial titanium carbide formation. Thus, while diamond growth was possible on TiN coated 440C bearings, continuity and adhesion of the films were poor for all conditions. This agrees with previous work on TiN in allowing for diamond films to be grown on ferrous substrates with a lack of interfacial carbide. The presence of titanium was

expected to allow for a titanium carbide phase to form during the initial diamond nucleation such as with well-adhered NSD films obtained on the titanium alloy, Ti-6-4. Additionally, while TiN has a slightly smaller linear thermal expansion coefficient than 440C stainless steel, it is still relatively high compared with diamond which aided in the delamination of most of the diamond films during sample cooling.

Novel microwave plasma CVD using H_2 and B_2H_6 feedgases allows for surface boriding of various metals as the diborane is dissociated and boron is diffused into the surface where it reacts to form metal boride phases. Surface boriding of 440C stainless steel produced a boride interlayer consisting of both Fe_2B and FeB. The presence of FeB is not necessarily an indicator of failure since it is unknown if it is forming a continuous outer layer. However, the absence of any FeB is ultimately preferred to avoid this issue altogether. Following diamond deposition on these borided bearings, XRD confirmed the presence of both diamond and interfacial chromium carbides. Carbide formation, which was absent on TiN interlayers, is a potential indicator of adequate adhesion. Raman spectroscopy confirmed the characteristic signal for an NSD coating. SEM imaging of the diamond films showed a majority of surface coverage, but regions still existed where the film delaminated or did not coalesce. Further examination of these regions revealed possible carbon nanotubes at some spots which are indicative of elemental iron reacting to form sp^2 bonded carbon. However, since coverage vastly improved over TiN interlayers, tubular structures were not detected in all uncoated regions, and both XRD and Raman data were favorable, this alone is not enough to dismiss the boride interlayer as a sufficient diffusion barrier. In terms of an application standpoint, the incomplete surface coverage is the first obstacle that must be overcome. Additionally, the rough

NSD film surface is a likely problem that would require a post-sanding step to obtain a reduced surface roughness ideal for wear applications.

Work then transitioned to 316 austenitic stainless steel discs which were optimized to have minimal α'-martensite. Direct diamond deposition with no interlayer was performed for comparison with subsequent results, and as expected, sp^2 bonded carbon and various carbide soot resulted as evidenced by Raman spectroscopy and XRD. Given the promise of MPCVD boriding on 440C stainless steel bearing, this interlayer was then employed on 316 discs. A chief result of the novel method of microwave plasma CVD boriding applied to 316 stainless steel is the ability to tailor the composition of the diffusion-based boride coating. Variation of temperature from 550 °C to 800 °C resulted in an evolution of present crystalline phases in the coating: (CrB) → (CrB + Fe_2B) → (Fe_2B). At no point was the problematic FeB phase observed. This is an important consideration since this phase is known to be brittle and has an even greater thermal expansion coefficient than 316 stainless steel which often results in cracking and potentially delamination merely after boriding. Following boriding, indentation testing results showed excellent adhesion for all coatings with only stable circumferential cracking present at low temperatures with continual reduction in the amount of cracking as temperature increased until it was no longer observed at 750 °C. This appears to be linked to the transition of phases with increasing boriding temperature yielding greater amounts of Fe_2B present in the interlayer until it is the sole phase at 750 °C. Cross-sectional SEM in combination with energy dispersive X-ray spectroscopy confirmed the results of a graded, diffusion-based coating in contrast to a discrete interface. Subsequent diamond deposition resulted in good coverage for discs with Fe_2B interlayers. SEM

revealed agglomeration of diamond nanocrystallites resulting in a rough surface morphology. Previous work on borided interlayers for subsequent diamond deposition also showed the promise of an Fe_2B interlayer allowing for continuous film growth. Clustering of grains into balls was also observed producing a rough surface. As with 440C bearings, prior to implementation of various tools, this will need to be addressed. The surface roughness could be associated with the rough, coral-grain morphology detected on Fe_2B-based interlayers with microwave plasma CVD producing a conformal film on this surface. While the borided interlayers formed by microwave plasma CVD shows excellent promise, work is still required on both the boriding and diamond deposition phases of research.

4.2 Future Work

Indentation testing was a preliminary method for qualitatively comparing the relative adhesion of the various boride layers. A more quantitative technique for obtaining a value for adhesion strength needs to be explored. Scratch testing is one such technique that can be used to obtain a critical load value. A continually increasing load is applied to a stylus that is moved across the surface and the point of coating failure is determined by using acoustic emission and imaging of the scratch track. A set of experiments using the same scratch adhesion testing system with the same tip and preferably the same coating thickness is required to make direct comparison between coatings. While rarely reported on in literature, scratch testing has been applied to borided steels [80]. Scratch testing can likewise be applied to diamond coatings in

addition to Rockwell indentation with a ball indenter which must be monitored given the hardness of the diamond material it is indenting [17].

In addition to scratch testing, further interfacial studies of the boride surface should be conducted. Cross-sectioning of borided discs from a range of temperatures producing an evolution of phases should be conducted and imaged. EDS can be performed, but it is preferable to use wavelength dispersive X-ray spectroscopy given its much improved resolution allowing it to resolve peak overlaps that plague EDS, and its ability to detect atomic numbers down to $Z = 4$. While EDS can detect down to $Z = 4$ (implementing a windowless or thin-window design), it is greatly inferior given its detection limits [81]. One drawback is the considerably longer scan time, approximately 30 minutes for a full wavelength spectrum with a sufficiently high sensitivity. This time length can be reduced using automation where only relevant peak positions are scanned. Additionally, a substantially higher beam current is needed because the diffraction process results in significantly lower efficiency. Also, fewer generated X-rays are actually detected given the spatial arrangement of the detector relative to the sample. Additionally, X-ray photoelectron spectroscopy can be employed in conjunction with argon-ion sputtering to perform depth profiling. Based on boride layer thickness measurements from cross-sectional SEM, a sputter rate can then be determined for calibration.

The interfacial chemistry is of paramount importance for obtaining an adhered film. Studies must be conducted on various boride chemistries using interrupted diamond depositions. After boriding, the sample is ultrasonically agitated in diamond slurry just as for a normal diamond deposition. The difference occurs by stopping the NSD diamond

deposition prior to achieving a coalescing film in order to study the initial stages of nucleation. A set time such as the first peak in the pyrometer measured temperature (diamond growth leads to changes in the emissivity of the film and substrate resulting from interference, absorption, and scattering which produces oscillations in the temperature reading and can be related to growth rate of the diamond film) will result in comparable nucleation times of the diamond film. The interface can then be probed by XRD for various crystalline phases such as interfacial chromium carbides or the presence of unwanted crystalline graphite. Even more important is XPS given its surface sensitivity which can also examine chemical bonding such as the existence of carbides, but more importantly, it can determine whether elemental iron or nickel are present on the surface.

REFERENCES

[1] R.S. Balmer, J.R. Brandon, S.L. Clewes, H.K. Dhillon, J.M. Dodson, I. Friel, P.N. Inglis, T.D. Madgwick, M.L. Markham, T.P. Mollart, N. Perkins, G.A. Scarsbrook, D.J. Twitchen, A.J. Whitehead, J.J. Wilman, S.M. Woollard, Chemical vapour deposition synthetic diamond: materials, technology and applications, Journal of Physics: Condensed Matter, 21 (2009) 364221.

[2] D.K.R. Jes Asmussen, Diamond Films Handbook, CRC Press, New York, 2002.

[3] A. Paoletti, A. Tucciarone, S.i.d. fisica, The Physics of Diamond, IOS Press, 1997.

[4] E.S. K. Fabisiak, CVD diamond: from growth to application, Journal of Achievements in Materials and Manufacturing Engineering, 37 (2009) 264-269.

[5] K.M. Kadish, R.S. Ruoff, Fullerenes: Chemistry, Physics, and Technology, Wiley, 2000.

[6] F. Langa, J.F. Nierengarten, R.S.o. Chemistry, Fullerenes: Principles and Applications, Royal Society of Chemistry, 2007.

[7] V.V.Z. O.A. Shenderova, and D.W. Brenner, Carbon Nanostructures, Critical Reviews in Solid State and Materials Sciences, 27 (2002) 227-356.

[8] N. Yahya, Carbon and Oxide Nanostructures: Synthesis, Characterisation and Applications, Springer Berlin Heidelberg, 2011.

[9] Carbon Nanotubes: Science and Applications, Taylor & Francis, 2004.

[10] M.J. O'Connell, Carbon Nanotubes: Properties and Applications, CRC Press, 2006.

[11] W. Choi, J. Lee, Graphene: Synthesis and Applications, Taylor & Francis, 2011.

[12] M.I. Katsnelson, M.I. Katsnel′son, Graphene: Carbon in Two Dimensions, Cambridge University Press, 2012.

[13] J. Robertson, Diamond-like amorphous carbon, Marterials Science and Engineering R, 37 (2002) 129-281.

[14] A.C. Ferrari, J. Robertson, Raman spectroscopy of amorphous, nanostructured, diamond–like carbon, and nanodiamond, 2004.

[15] J. Filik, Raman spectroscopy: a simple, non-destructive way to characterise diamond and diamond-like materials, Spectroscopy Europe, 17 (2005) 10-17.

[16] S.A. Catledge, V. Thomas, Y.K. Vohra, Nanostructured diamond coatings for orthopaedic applications, Woodhead publishing series in biomaterials, 2013 (2013) 105-150.

[17] L. Booth, S.A. Catledge, D. Nolen, R.G. Thompson, Y.K. Vohra, Synthesis and Characterization of Multilayered Diamond Coatings for Biomedical Implants, Materials, 4 (2011) 857-867.

[18] S.A. Catledge, R. Vaid, P. Diggins, J.J. Weimer, M. Koopman, Y.K. Vohra, Improved adhesion of ultra-hard carbon films on cobalt–chromium orthopaedic implant alloy, Journal of materials science. Materials in medicine, 22 (2011) 307-316.

[19] L. Tang, C. Tsai, W.W. Gerberich, L. Kruckeberg, D.R. Kania, Biocompatibility of chemical-vapour-deposited diamond, Biomaterials, 16 (1995) 483-488.

[20] R. Narayan, Diamond-Based Materials for Biomedical Applications, Elsevier Science, 2013.

[21] J.R. Davis, Alloy Digest Sourcebook: Stainless Steels, ASM International, 2000.

[22] P. Marshall, Austenitic Stainless Steels: Microstructure and Mechanical Properties, Springer, 1984.

[23] M.F. McGuire, Stainless Steels for Design Engineers, ASM International, 2008.

[24] G.E. Totten, M.A.H. Howes, Steel Heat Treatment Handbook, Taylor & Francis, 1997.

[25] R. Haubner, B. Lux, Diamond deposition on steel substrates using intermediate layers, International Journal of Refractory Metals and Hard Materials, 24 (2006) 380-386.

[26] A.H. Lettington, J. Steeds, Thin Film Diamond, Springer Netherlands, 2012.

[27] R.F. Davis, Diamond Films and Coatings: Development, Properties, and Applications, Noyes Pub., 1993.

[28] X. Chen, J. Narayan, Effect of the chemical nature of transition‐metal substrates on chemical‐vapor deposition of diamond, Journal of Applied Physics, 74 (1993) 4168-4173.

[29] T.S. V.F. Neto, M.S.A. Oliveira,, J.G.a.N. Ali, Polycrystalline diamond coatings on steel substrates, International Journal of Nanomanufacturing, 2 (2008).

[30] M.A. Nicolet, Diffusion barriers in thin films, Thin Solid Films, 52 (1978) 415-443.

[31] M. Östling, S. Nygren, C.S. Petersson, H. Norström, R. Buchta, H.O. Blom, S. Berg, A comparative study of the diffusion barrier properties of TiN and ZrN, Thin Solid Films, 145 (1986) 81-88.

[32] P.S. Weiser, S. Prawer, A. Hoffman, R.R. Manory, P.J.K. Paterson, S.A. Stuart, Carbon diffusion in uncoated and titanium nitride coated iron substrates during microwave plasma assisted chemical vapor deposition of diamond, Journal of Applied Physics, 72 (1992) 4643-4647.

[33] N.Y. Filonenko, O.Y. Beryoza, O.G. Bezrukava, The effect of carbon on phase composition and phase transformations in Fe-B system alloys, Problems of Atomic Science and Technology, 87 (2013) 168-171.

[34] B.D. Sartwell, Metallurgical Coatings and Thin Films 1990, Elsevier Science, 2012.

[35] M. Ohring, Engineering Materials Science, Academic Press, 1995.

[36] A.I.H. Committee, ASM handbook: Heat treating, ASM International, 1991.

[37] H. Shih, A Systematic Study and Characterization of Advanced Corrosion Resistance Materials and Their Applications for Plasma Etching Processes in Semiconductor Silicon Wafer Fabrication, INTECH Open Access Publisher, 2012.

[38] J.B. Cohen, T. Bell, K. Funatani, G.E. Totten, A. International, A.S.M.H.T.S.C. Exposition, A.S.M.H.T. Society, Heat Treating: Including Advances in Surface Engineering, an International Symposium in Honor of Professor Tom Bell, and Professor Jerome B. Cohen Memorial Symposium on Residual Stresses in the Heat Treatment Industry : Proceedings of the 20th Conference, 9-12 October 2000, St. Louis, Missouri, A S M International, 2001.

[39] J.R. Davis, Surface Hardening of Steels: Understanding the Basics, A S M International, 2002.

[40] H. Li, M. Gowri, J.J. Schermer, W.J.P. van Enckevort, T. Kacsich, J.J. ter Meulen, Bias enhanced diamond nucleation on Mo and CrN coated stainless steel substrates in a HFCVD reactor, Diamond and Related Materials, 16 (2007) 1918-1923.

[41] G. Negrea, G. Vermesan, Investigations of diamond layers growth on steel, Journal of Optoelectronics, 2 (2000) 698-703.

[42] J.G. Buijnsters, P. Shankar, W. Fleischer, W.J.P. van Enckevort, J.J. Schermer, J.J. ter Meulen, CVD diamond deposition on steel using arc-plated chromium nitride interlayers, Diamond and Related Materials, 11 (2002) 536-544.

[43] C.-L. Chang, D.-Y. Wang, Microstructure and adhesion characteristics of diamond-like carbon films deposited on steel substrates, Diamond and Related Materials, 10 (2001) 1528-1534.

[44] R. Polini, F. Pighetti Mantini, M. Braic, M. Amar, W. Ahmed, H. Taylor, M.J. Jackson, Effects of Ti- and Zr-based interlayer coatings on hot-filament chemical vapor deposition of diamond on high-speed steel, J. of Materi Eng and Perform, 15 (2006) 201-207.

[45] P.S. Weiser, S. Prawer, Chemical vapour deposition of diamond onto iron based substrates—The use of barrier layers, Diamond and Related Materials, 4 (1995) 710-713.

[46] F.J.G. Silva, A.J.S. Fernandes, F.M. Costa, A.P.M. Baptista, E. Pereira, A new interlayer approach for CVD diamond coating of steel substrates, Diamond and Related Materials, 13 (2004) 828-833.

[47] A.K. Sikder, T. Sharda, D.S. Misra, D. Chandrasekaram, P. Selvam, Chemical vapour deposition of diamond on stainless steel: the effect of Ni-diamond composite coated buffer layer, Diamond and Related Materials, 7 (1998) 1010-1013.

[48] R.A. Vieira, M.C.A. Nono, Modification of a 304 ss surface with a titanium film to improve the adherence of cvd diamond, Revista Brasileira de Aplicacoes de Vacuo, 27 (2008) 133-135.

[49] Y.S. Li, Y. Tang, Q. Yang, J. Maley, R. Sammynaiken, T. Regier, C. Xiao, A. Hirose, Ultrathin W−Al Dual Interlayer Approach to Depositing Smooth and Adherent Nanocrystalline Diamond Films on Stainless Steel, ACS Applied Materials & Interfaces, 2 (2010) 335-338.

[50] C.F.M. Borges, E. Pfender, J. Heberlein, Influence of nitrided and carbonitrided interlayers on enhanced nucleation of diamond on stainless steel 304, Diamond and Related Materials, 10 (2001) 1983-1990.

[51] J.G. Buijnsters, P. Shankar, P. Gopalakrishnan, W.J.P. van Enckevort, J.J. Schermer, S.S. Ramakrishnan, J.J. ter Meulen, Diffusion-modified boride interlayers for chemical vapour deposition of low-residual-stress diamond films on steel substrates, Thin Solid Films, 426 (2003) 85-93.

[52] P.S. JG Buijnsters, WJP van Encekvort, JJ Schermer, JJ ter Meulen, The adhesion of hot-filament CVD diamond films on AISI type 316 austenitic stainless steel, Diamond & Related Materials, 13 (2004) 848-857.

[53] W.v.E. M Gowri, JJ Schermer, JP Celis, JJ ter Meulen, JG Buijnsters, Growth and adhesion of hot filament chemical vapor deposited diamond coatings on surface modified high speed steel, Diamond & Related Materials, 18 (2009) 1450-1458.

[54] S.K. Sarangia, D.K. Sahub, S. Padhic, A.K. Chattopadhyayd, Nucleation and growth of diamond by different seeding mechanisms on cemented carbide inserts by HFCVD process in: 5th International & 26th All India Manufacturing Technology, Design and Research Conference, Guwahati, Assam, India, 2014.

[55] K.E. Spear, J.P. Dismukes, E. Society, Synthetic Diamond: Emerging CVD Science and Technology, Wiley, 1994.

[56] I.R. Lewis, H. Edwards, Handbook of Raman Spectroscopy: From the Research Laboratory to the Process Line, CRC Press, 2001.

[57] E. Smith, G. Dent, Modern Raman Spectroscopy: A Practical Approach, Wiley, 2013.

[58] R. Pfeiffer, H. Kuzmany, P. Knoll, S. Bokova, N. Salk, B. Günther, Evidence for trans-polyacetylene in nano-crystalline diamond films, Diamond and Related Materials, 12 (2003) 268-271.

[59] S. Prawer, R.J. Nemanich, Raman spectroscopy of diamond and doped diamond, 2004.

[60] Properties, Sources, and Detection of Radiation, in: Fundamentals of Powder Diffraction and Structural Characterization of Materials, Springer US, 2009, pp. 107-132.

[61] B. Fultz, J. Howe, Diffraction and the X-Ray Powder Diffractometer, in: Transmission Electron Microscopy and Diffractometry of Materials, Springer Berlin Heidelberg, 2013, pp. 1-57.

[62] C.C. Chusuei, D.W. Goodman, X-Ray Photoelectron Spectroscopy, in: R.A. Meyers (Ed.) Encyclopedia of Physical Science and Technology (Third Edition), Academic Press, New York, 2003, pp. 921-938.

[63] J.F. Moulder, J. Chastain, Handbook of X-ray Photoelectron Spectroscopy: A Reference Book of Standard Spectra for Identification and Interpretation of XPS Data, Physical Electronics, 1995.

[64] C.R. Brundle, A.D. Baker, Electron Spectroscopy: Theory, Techniques and Applications, Academic Press, 1977.

[65] W. Zhou, R. Apkarian, Z. Wang, D. Joy, Fundamentals of Scanning Electron Microscopy (SEM), in: W. Zhou, Z. Wang (Eds.) Scanning Microscopy for Nanotechnology, Springer New York, 2007, pp. 1-40.

[66] P.E. West, Introduction to Atomic Force Microscopy: Theory, Practice, Applications, P. West, 2006.

[67] A.C. Ferrari, J. Robertson, Interpretation of Raman spectra of disordered and amorphous carbon, Physical Review B, 61 (2000) 14095-14107.

[68] A.C. Ferrari, S.E. Rodil, J. Robertson, Interpretation of infrared and Raman spectra of amorphous carbon nitrides, Physical Review B, 67 (2003) 155306.

[69] M. Marton, M. Vojs, E. Zdravecka, M. Himmerlich, T. Haensel, S. Krischok, M. Kotlar, P. Michniak, M. Vesely, R. Redhammer, Raman Spectroscopy of Amorphous Carbon Prepared by Pulsed Arc Discharge in Various Gas Mixtures, Journal of Spectroscopy, 2013 (2013) 6.

[70] N. Solomon, I. Solomon, Deformation induced martensite in AISI 316 stainless steel, Revista de metaluriga, 46 (2010) 121-128.

[71] E.K.-O. A. Kurc-Lisiecka, Structure and mechanical properties of austenitic steel after cold rolling, Journal of Achievements in Materials and Manufacturing Engineering, 44 (2011) 148-153.

[72] G.F. A. Zapata, A. Mateo, Effect of cold rolling on the high cycle fatigue behaviour of an AISI 301LN stainless steel, Anales de Mecánica de la Fractura, 1 (2011).

[73] H.F.G.d. Abreua, S.S.d. Carvalhoa, P.d.L. Netoa, R.P.d. Santosa, V.N. Freirea, P.M.d.O. Silvab, S.S.M. Tavares, Deformation Induced Martensite in an AISI 301LN Stainless Steel: Characterization and Influence on Pitting Corrosion Resistance, Materials Research, 10 (2007).

[74] I. Altenberger, B. Scholtes, U. Martin, H. Oettel, Cyclic deformation and near surface microstructures of shot peened or deep rolled austenitic stainless steel AISI 304, Materials Science and Engineering: A, 264 (1999) 1-16.

[75] W.F. Gale, T.C. Totemeier, Smithells Metals Reference Book, Elsevier Science, 2003.

[76] S. Taktak, S. Tasgetiren, Identification of delamination failure of boride layer on common Cr-based steels, J. of Materi Eng and Perform, 15 (2006) 570-574.

[77] P.A. Dearnley, T. Bell, Engineering the surface with boron based materials, Surface Engineering, 1 (1985) 203-217.

[78] C. Badini, C. Gianoglio, G. Pradelli, Preferential distribution of chromium and nickel in the borided layer obtained on synthetic Fe-Cr-Ni alloys, J Mater Sci, 21 (1986) 1721-1729.

[79] G. Samudrala, Y. Vohra, M. Walock, R. Miles, Rapid Growth of Nanostructured Diamond Film on Silicon and Ti–6Al–4V Alloy Substrates, Materials, 7 (2014) 365.

[80] O. Allaoui, N. Bouaouadja, G. Saindernan, Characterization of boronized layers on a XC38 steel, Surface and Coatings Technology, 201 (2006) 3475-3482.

[81] J. Goldstein, D.E. Newbury, P. Echlin, D.C. Joy, A.D. Romig, C.E. Lyman, C. Fiori, E. Lifshin, Scanning Electron Microscopy and X-Ray Microanalysis: A Text for Biologists, Materials Scientists, and Geologists, Springer US, 2012.